A PI BASED COORDINATED MAXIMUM POWER POINT TRACKING CONTROLLER FOR GRID CONNECTED PHOTOVOLTAIC SYSTEM

MD HAIDAR ISLAM

FACULTY OF ENGINEERING
DEPARTMENT OF ELECTRICAL ENGINEERING
UNIVERSITY OF MALAYA
KUALA LUMPUR

2021

A PI BASED COORDINATED MAXIMUM POWER POINT TRACKING CONTROLLER FOR GRID CONNECTED PHOTOVOLTAIC SYSTEM

MD HAIDAR ISLAM

DISSERTATION SUBMITTED IN FULFILMENT OF THE REQUIREMENTS FOR THE DEGREE OF MASTER BY RESEARCH IN ELECTRICAL ENGINEERING

FACULTY OF ENGINEERING
DEPARTMENT OF ELECTRICAL ENGINEERING
UNIVERSITY OF MALAYA
KUALA LUMPUR

2021

UNIVERSITY OF MALAYA

ORIGINAL LITERARY WORK DECLARATION

Name of Candidate: MD HAIDAR ISLAM

Matric No: KGA150058 (17058018/1)

Name of Degree: Master of Engineering Science

Title of Dissertation: A PI BASED COORDINATED MAXIMUM POWER POINT TRACKING CONTROLLER FOR GRID CONNECTED PHOTOVOLTAIC SYSTEM

Field of Study: Power Electronics

I do solemnly and sincerely declare that:

(1) I am the sole author/writer of this Work;
(2) This Work is original;
(3) Any use of any work in which copyright exists was done by way of fair dealing and for permitted purposes and any excerpt or extract from, or reference to or reproduction of any copyright work has been disclosed expressly and sufficiently and the title of the Work and its authorship have been acknowledged in this Work;
(4) I do not have any actual knowledge nor do I ought reasonably to know that the making of this work constitutes an infringement of any copyright work;
(5) I hereby assign all and every rights in the copyright to this Work to the University of Malaya ("UM"), who henceforth shall be owner of the copyright in this Work and that any reproduction or use in any form or by any means whatsoever is prohibited without the written consent of UM having been first had and obtained;
(6) I am fully aware that if in the course of making this Work I have infringed any copyright whether intentionally or otherwise, I may be subject to legal action or any other action as may be determined by UM.

Candidate's Signature   Date:

Subscribed and solemnly declared before,

Witness's Signature   Date:

Name:

Designation:

A PI BASED COORDINATED MAXIMUM POWER POINT TRACKING CONTROLLER FOR GRID CONNECTED PHOTOVOLTAIC SYSTEM

ABSTRACT

The global demand for electric energy has continuously increased over the last few decades. Photovoltaic (PV) sources are predicted to become one of the biggest contributors to electricity generation among all renewable energy generation candidates by 2040. The photovoltaic system a renewable energy source that has attracted the attention of researchers in recent years. The power output of a photovoltaic system has a complex dependence on varying environmental conditions such as solar irradiation and ambient temperature which cannot be controlled, thereby making the current versus voltage (I-V) and power versus voltage (P-V) characteristics of photovoltaic arrays nonlinear. Therefore, maximum power varies from time to time as these factors change rapidly. In order to maintain maximum power of the PV system, maximum power point tracking (MPPT) techniques are incorporated with direct current to direct current (DC-DC) converters and proportional integral (PI) controllers. A MPPT is an automatic control algorithm used to adjust the power interfaces and achieve the maximum possible power harvest, during instantaneous deviations of light levels, shading, temperature, and photovoltaic module characteristics. The idea behind the MPPT techniques is to adjust an operating voltage close to a maximum power point (MPP) under constantly changing atmospheric conditions. The MPPT techniques vary in many aspects such as: digital or analogical implementation, tracking speed, convergence speed, cost, simplicity and in other aspects. The differences between conventional and other modified MPPT algorithms are explained in this research work. A new coordinated PI-MPPT algorithm is then proposed based on the deficiencies of the other algorithms. The proposed MPPT algorithm is used to maximize a conversion efficiency of a PV array. The proposed algorithm's reference variables such as current, voltage, duty cycle and power output will be traced and the results obtained for different weather conditions. The proposed algorithm enhances the steady-state and dynamic responses by introducing an improved adaptive step-size for updating variables. A low complexity grid synchronization controller is implemented to generate parallel and orthogonal components of the grid voltage in a highly computationally efficient manner in order to create a synchronized current reference to the current control loop. MATLAB Simulink tool box is used to create models to carry out performance evaluation of a PV module with the MPPT algorithms. The grid-connected PV system is implemented with dSPACE controller and solar simulator, and other measuring instruments. Theoretical demonstrations are verified by the simulation and experimental results of the proposed system. The measured results validated that the proposed coordinated PI-MPPT technique tracks reference values accurately. The power efficiency of the proposed algorithm is achieved by 99.92%, 99.8%, 99.88% and 99.83% against uniform weather, partial shading conditions (PSCs) 1, 2 and 3, respectively, which is much higher than that of conventional MPPT techniques. The proposed system is an improved method which designed and modeled to obtain good accuracy and stability of tracking GMPP under highly dynamic conditions.

Keywords: Photovoltaic (PV), Maximum Power Point (MPP), Maximum Power Point Tracker (MPPT), Pulse Width Modulation (PWM) and Sine Pulse Width Modulation (SPWM).

PENGAWAL PENJEJAKAN TITIK KUASA MAKSIMUM TERKOORDINAT BERDASARKAN PI UNTUK SISTEM FOTOVOLTAIK BERORIENTASI GRID

ABSTRAK

Permintaan global untuk tenaga elektrik terus meningkat sejak beberapa dekad yang lalu. Sumber PV diramal akan menjadi salah satu penyumbang terbesar kepada penjanaan elektrik dari kumpulan kaedah penjanaan tenaga boleh diperbaharui menjelang tahun 2040. Sistem fotovolta adalah sumber tenaga yang boleh diperbaharui yang telah menarik perhatian ramai para penyelidik sejak beberapa tahun kebelakangan ini. Bagaimanapun hasil tenaga yang terjana dari sistem fotovolta mempunyai kebergantungan yang kompleks pada keadaan persekitaran yang sentiasa berubah-ubah seperti penyinaran suria dan suhu persekitaran yang tidak dapat dikawal, sehingga menyebabkan ciri arus melawan votan I-V dan kuasa melawan voltan P-V bagi fotovoltaik tidak berkadar terus. Ini menyebabkan tenaga maksimum berubah-ubah dari semasa ke semasa disebabkan ciri faktor persekitaran yang berubah dengan cepat. Untuk mengekalkan kuasa maksimum suatu sistem PV, teknik Penjejak Titik Tenaga Maksimum (MPPT) telah digabungkan dengan penukar arus terus ke arus terus dan pengawal kamiran berkadaran (PI). MPPT adalah algoritma kawalan automatik yang digunakan untuk mengawal tenaga antaramuka dan mencapai penuaian tenaga semaksimum yang mungkin semasa perubahan seketika yang berpunca dari perubahan tahap cahaya, bayangan, suhu, dan ciri modul fotovolta. Idea di sebalik teknik MPPT adalah menyesuaikan voltan operasi kepada yang terhampir dengan Titik Tenaga Maksimum (MPP) semasa keadaan persekitaran yang sentiasa berubah. Terdapat pelbagai teknik MPPT seperti: pelaksanaan digital atau analog, kelajuan penjejakan, kelajuan penumpuan, kos, kesederhanaan dan lain-lain. Perbezaan antara algoritma yang diubahsuai dan yang lazim juga telah dijelaskan dalam hasil penyelidikan ini. Algoritma

PI-MPPT terselaras baru yang dicadangkan dapat menampung kekurangan algoritma yang lain. Algoritma MPPT yang dicadangkan digunakan untuk memaksimukan kecekapan penukaran suatu tatasusunan PV. Algoritma yang dicadangkan mengesan perubahan pembolehubah seperti arus, voltan, kitaran tugas dan keluaran kuasa dan hasilnya diperoleh mengikut keadaan cuaca yang berbeza. Algoritma yang dicadangkan meningkatkan tindakbalas keadaan stabil dan dinamik dengan memperkenalkan ukuran langkah adaptif yang lebih baik untuk mengemaskini pembolehubah. Kaedah penyegerakan grid kompleks rendah dilaksanakan untuk menghasilkan komponen selari dan orthogonal voltan grid dengan cara yang sangat efisien untuk membuat rujukan arus segerak kepada gelung kawalan semasa. Perisian toolbox SimuLink MATLAB digunakan untuk membina model untuk melaksanakan simulasi bagi menilaian prestasi modul PV dengan algoritma terkawal. Sistem PV disambungkan dengan grid dilaksanakan bersama pengawal dSPACE dan simulator solar. Demonstrasi teori disahkan oleh hasil simulasi dan eksperimen sistem yang dicadangkan. Hasil yang diukur mengesahkan bahawa teknik PI-MPPT terkoordinasi yang dicadangkan mengesan nilai rujukan dengan tepat. Kecekapan daya algoritma yang dicadangkan mencapai 99.92%, 99.8%, 99.88% dan 99.83% pada semua keadaan normal, cuaca yang sama dengan lokasi GMPP disebelah kanan, tengah dan kiri di antara beberapa titik asal berturut-turut. Kecekapan ini lebih tinggi daripada teknik konvensional MPPT. Sistem yang dicadangkan adalah kaedah suatu kaedah penambahbaikan yang telah direkabentuk dan dimodelkan untuk mendapatkan ketepatan dan kestabilan yang lebih baik dalam pengesanan GMPP dalam keadaan yang dinamik.

Kata kunci: Fotovoltaik (PV), titik tenaga maksimum (MPP), penjejak titik tenaga maksimum (MPPT), modulasi lebar denyut (PWM) dan modulasi lebar denyut sinus (SPWM).

ACKNOWLEDGEMENTS

Firstly, I am genuinely grateful to the Almighty Allah for his blessings and mercy to complete this challenging research work.

I want to show my deepest gratitude to my three supervisors, PROF. SAAD MEKHILEF, DR. TEY KOK SOON, and DR. NORAISYAH BINTI MOHAMED SHAH. My study at the University of Malaya was made possible due to their generous help. Their guidance, patience, advice, encouragement, and financial support help me overcome the difficulties in pursuing my degree. It is indeed a valuable opportunity to learn the rigorous attitude towards study and research from them.

To my friends, I would like to thank my fellow members from power electronics and renewable energy laboratory (PEARL) and friends, especially Immad Shams, Leong Wen Chek, Shameem Ahmad, Tuanku Badzlin, Fardila Mohd Zaihidee, Dr. Mostefa Kermadi, Mohammad Zahirul Amin Chowdhury and many more for their assistance and support throughout my candidature.

My deepest gratitude belongs to my parents Mr. MD. Shiraj Ullah and Late Ms. Zahura Khatun, my brothers Mr. MD. Abu Yousuf and Mr. MD. Zainul Abedin and my sisters Khadija, Amena, and Majeda for their countless prayers, love, sacrifice, and unconditional support for my study.

TABLE OF CONTENTS

Abstract iii

Abstrak v

Acknowledgements vii

Table of Contents viii

List of Figures xiii

List of Tables..xvii

List of Symbols and Abbreviations xviii

CHAPTER 1: INTRODUCTION 1

1.1 Background.. 1

1.2 Problem Statement 3

1.3 Objectives of the Study... 5

1.4 Methodology... 6

CHAPTER 2: LITERATURE REVIEW 9

2.1 Introduction... 9

2.2 PV Array Modelling 9

2.3 Impacts on PV System 12

2.3.1 PV Panel Tilt and Orientation 12

2.3.2 Soiling Effect on PV Array 13

2.3.3 Snow Effect on the PV Array.. 14

2.3.4 Bypass and Blocking Diodes Effects 15

2.3.5 Load Effects on PV Array 16

2.4 Performance Analysis on MPPT Control Variables 17

2.4.1 Dynamic Weather Response to PV System... 17

2.4.2 Steady-State Error (SSE) 17

2.4.3 Robustness to Disturbances 18
2.4.4 The efficiency of a Large Power Capacity 18
2.4.5 PSCs Handling 19
2.4.6 Power Oscillation Near MPP Location 19
2.4.7 Tracking Speed 20
2.4.8 Convergence Speed 20
2.5 Types of MPPT Techniques 21
2.5.1 Others MPPT Algorithms 21
2.5.2 P&O MPPTs 22
2.5.3 INC MPPTs 26
2.5.3.1 Fixed step size (FSS)-INC algorithm 27
2.5.3.2 Variable Step Size (VSS)-INC MPPT 28
2.5.3.3 Adaptive INC MPPT algorithm 29
2.5.3.4 Modified adaptive INC algorithm 30
2.5.3.5 Power increment INC-MPPT technique 31
2.5.3.6 Solar tracker (ST)-INC algorithm 32
2.5.3.7 First converged INC-MPPT with FOCV and FSSC algorithms 34
2.5.3.8 FLC based INC-MPPT scheme 34
2.5.4 DC-DC Converters 37
2.5.5 Control of MPPTs and Boost Converter 39
2.5.6 Photovoltaic Inverters 40
2.5.6.1 Single-stage centralized inverter (SSCI) 40
2.5.6.2 Single-stage string inverter (SSSI) 41
2.5.7 Grid Integrated PV System 41
2.5.8 Control Techniques of the Grid-Connected PV System 42
2.5.8.1 SPWM techniques 43

2.5.8.2 Proportional Resonance (PR) and PI controllers........................44

2.5.9 DC-link capacitor 44

2.5.10 Grid synchronization Technique 45

2.6 Summary..47

CHAPTER 3: PROPOSED SYSTEM DESIGN 50

3.1 Introduction...50

3.2 Proposed Complete Topology 51

3.3 PV array design under Partial Shading Conditions 52

3.4 MPPT Schemes Design 54

3.4.1 P&O-MPPT Algorithm 55

3.4.2 INC-MPPT Algorithm...56

3.4.3 Proposed Coordinated PI-MPPT Algorithm 58

3.5 DC-DC Boost Converter Design 62

3.5.1 Principle and Circuit Elements Design...63

3.5.2 Transfer Function of the Boost Converter...66

3.6 Grid-Connected FB-VSI Design...69

3.6.1 Switching Circuit Configurations of the VSI 70

3.6.2 DC-Link Capacitor at the Input of the Inverter 71

3.6.3 LCL type LPF Filter Design...72

3.6.4 VSI Control Design 76

3.6.4.1 Bipolar SPWM Switching Control...76

3.6.4.2 Proportional Resonant Controller (PR) 77

3.6.5 Grid Synchronization Controller 80

3.7 Summary...81

CHAPTER 4: SIMULATION AND EXPERIMENTAL RESULTS 83

4.1 Introduction..83

4.2 Simulation Results 83

4.2.1 P-V and I-V Curves for Uniform and Shading Pattern 1, 2, and 3...........84

4.2.2 Simulation Results from INC-MPPT 86

4.2.2.1 Uniform Weather Condition..86

4.2.2.2 Shading Condition 1 87

4.2.2.3 Shading Condition 2 88

4.2.2.4 Shading Condition 3 89

4.2.3 Simulation Results for P&O-MPPT Algorithm 90

4.2.3.1 Uniform Weather Condition..90

4.2.3.2 Shading Condition 1 91

4.2.3.3 Shading Condition 2 92

4.2.3.4 Shading Condition 3 92

4.2.4 Simulation Results for proposed PI-MPPT Algorithm 93

4.2.4.1 Uniform Weather condition 93

4.2.4.2 Shading Condition 1 94

4.2.4.3 Shading Condition 2 95

4.2.4.4 Shading Condition 3 96

4.2.5 Comparative Study 97

4.2.5.1 Uniform Weather condition 97

4.2.5.2 Shading Condition 1 98

4.2.5.3 Shading Condition 2 100

4.2.5.4 Shading Condition 3 101

4.2.5.5 Performance of H-Bridge VSI...102

4.3 Experimental Validation 104

4.3.1 Experimental Setup 104

4.3.2 PWM and SPWMs Generation in dSPACE Platform 106

4.3.3 Boost converter and VSI Tests 107

4.3.4 P-V and I-V Curves for Uniform and Shading Patterns 1, 2, and 3 108

4.3.5 Experimental Results for Uniform Weather Condition.......................... 110

4.3.6 Experimental Results for Shading Condition 1 111

4.3.7 Experimental Results from Shading Condition 2.................................. 113

4.3.8 Experimental Results for Shading Condition 3 115

4.3.9 Experimental Results for Voltage Source Inverter (VSI) 117

4.4 Comparative Study of the MPPTs Results 118

4.4.1 Comparative Study of the Simulation Results 119

4.4.2 Comparative Study of Experimental Results 119

4.4.3 Comparative Study between Literature and Experimental Results........ 120

4.5 Summary... 122

CHAPTER 5: CONCLUSION AND FUTURE WORK 124

5.1 Conclusion 124

5.2 Future Work.. 125

References 127

List of Publications and Papers Presented... 143

LIST OF FIGURES

Figure 1. 1: Flowchart of Research Activities 8

Figure 2. 1: Diagram of a photovoltaic cell (Villalva et al., 2009) 10

Figure 2. 2: P-V and I-V curves at changing solar irradiances 11

Figure 2. 3: P-V curve at PSCs 11

Figure 2. 4: I-V Curve at PSCs 12

Figure 2. 5: Factors of Dust on PV Modules (Maghami, Hizam, Gomes, Radzi, Rezadad, Hajighorbani, et al., 2016) 13

Figure 2. 6: An Algorithm to Detect Snowfall (Seyedali Meghdadi & Tariq Iqbal, 2015) 14

Figure 2. 7: Bypass and Blocking Diodes (Yunmei & Xiangwei, 2019) 15

Figure 2. 8: Types of MPPT Schemes 21

Figure 2. 9: MPP locations of INC algorithm (S. S. Mohammed & Devaraj, 2015) 27

Figure 2. 10: A Flowchart of an Adaptive INC-MPPT Scheme (Jedari, Gharehpetian, Fathi, & Vahids, 2016) 29

Figure 2. 11: An Adaptive INC MPPT (J.-G. Lee et al., 2012) 30

Figure 2. 12: Threshold Tracking Zones (Hsieh, Hsieh, Tsai, & Wang, 2012) 31

Figure 2. 13: A Diagram of ST-MPPT (D. C. Huynh & Dunnigan, 2016) 32

Figure 2. 14: Improved INC Algorithm (D. C. Huynh & Dunnigan, 2016) 33

Figure 2. 15: The Stages of the FLC (Abdourraziq & El Bachtiri, 2014) 35

Figure 2. 16: FLC Membership Functions and Subsets (Radjai et al., 2015) 35

Figure 2. 17: Direct Control INC with FLC (Radjai et al., 2014) 36

Figure 2. 18: DC-DC Boost Converter (R. Zhang, Wu, Zhang, Wang, & Cang, 2018) . 39

Figure 2. 19: Offline and Online Controller (Harrag & Messalti, 2015) 39

Figure 2. 20: Single-Stage Centralized Inverter (Kabalcı, 2020) 40

Figure 2. 21: Single-stage string inverter (Ovaska, 2010) 41

Figure 2. 22: Typical Diagram of Utility Grid (Suman, Yadav, & Jangid, 2018) 42

Figure 2. 23: Single-phase SRF-PLL (Stojić et al., 2017) 46

Figure 2. 24: SOGI based OSG-PLL (Cha, Vu, & Kim, 2009) 46

Figure 3. 1: Proposed Grid-Tied Topology 51

Figure 3. 2: Patterns for uniform and partial shading conditions are listed as (a–d) Shading patterns for PV array of Isoltech 1STH-250-WH; (e–h) Shading patterns for Atlantis Energy System SS125LM. 53

Figure 3. 3: A Flow Chart of P&O-MPPT 55

Figure 3. 4: A Flow Diagram of INC-MPPT 57

Figure 3. 5: A Coordinated Proposed PI-MPPT Algorithm 61

Figure 3. 6: A Function Block of the PI Controllers 62

Figure 3. 7: Boost converter configurations; (a) switch ON (b) Switch OFF 63

Figure 3. 8: Grid-Connected H-bridge Inverter Topology 70

Figure 3. 9: DC-Link Voltage 71

Figure 3. 10: The LCL Filter Circuit 73

Figure 3. 11: Magnitude Plot of the Filter Transfer Function 74

Figure 3. 12: A Complete Closed Loop Control System for the VSI 76

Figure 3. 13: Bipolar SPWM Control singles 77

Figure 3. 14: A Current Control Block of the PR controller 78

Figure 4. 1: P-V and I-V characteristic curves of the four weather conditions are showed as: (a) uniform weather; (b) shading condition 1; (c) shading condition 2; and (d) shading condition 3. 85

Figure 4. 2: Simulation results of Conventional INC-MPPT are; (a) P-V and I-V curves at STC, and (b) voltage, current, power, and duty cycle graphs 87

Figure 4. 3: Simulation results of the INC-MPPT are; (a) P-V and I-V curves at shading pattern 1, and (b) voltage, current, power, and duty cycle graphs 88

Figure 4. 4: Simulation results of the INC-MPPT are; (a) P-V and I-V curves at shading condition 2, and (b) voltage, current, power, and duty cycle graphs 89

Figure 4. 5: Simulation results of the INC-MPPT are; (a) P-V and I-V curves at shading pattern 3, and (b) voltage, current, power, and duty cycle graphs 90

Figure 4. 6: Simulation results of the P&O-MPPT are; (a) P-V and I-V curves at STC, and (b) voltage, current, power, and duty cycle graphs 91

Figure 4. 7: Simulation results of the P&O-MPPT are; (a) P-V and I-V curves at shading condition 1, and (b) voltage, current, power, and duty cycle graphs................ 91

Figure 4. 8: Simulation results of the P&O-MPPT are; (a) P-V and I-V curves at shading condition 2, and (b) voltage, current, power, and duty cycle graphs................ 92

Figure 4. 9: Simulation results of the P&O-MPPT are; (a) P-V and I-V curves at shading condition 2, and (b) voltage, current, power, and duty cycle graphs................ 93

Figure 4. 10: Simulation results of the Proposed MPPT are; (a) P-V and I-V curves at STC, and (b) voltage, current, power, and duty cycle graphs 94

Figure 4. 11: Simulation results of the Proposed MPPT are; (a) P-V and I-V curves at shading condition 1, and (b) voltage, current, power, and duty cycle graphs................ 95

Figure 4. 12: Simulation results of the Proposed-MPPT are; (a) P-V and I-V curves at shading condition 2, and (b) voltage, current, power, and duty cycle graphs................ 95

Figure 4. 13: Simulation results of the Proposed-MPPT are; (a) P-V and I-V curves at shading condition 3, and (b) voltage, current, power, and duty cycle graphs................ 96

Figure 4. 14: Comparative simulation results of INC, P&O, and Proposed algorithms at STC are listed as (a) STC waveforms; (b) power; (c) voltage (d); current; and (e) duty cycle waveforms.. 98

Figure 4. 15: Comparative Simulation results of INC, P&O, and proposed MPPTs at shading condition 1, are listed as (a) P-V and I-V curves; (b) power; (c) voltage; (d) current; and (e) duty cycle.. 99

Figure 4. 16: Comparative Simulation results of INC, P&O, and proposed MPPTs at shading condition 2 are listed as (a) P-V and I-V curves; (b) power; (c) voltage; (d) current; and (e) duty cycle.. 100

Figure 4. 17: Simulation results of INC, P&O, and proposed MPPTs at shading condition 3. are listed as (a) P-V and I-V curves; (b) power; (c) voltage; (d) current; and (e) duty cycle characteristics. 102

Figure 4. 18: Simulation results of the proposed VSI: (a) uniform weather; (b) shading pattern 1; (c) shading pattern 2; and (d) shading pattern 3. 103

Figure 4. 19: Experimental Setup... 105

Figure 4. 20: PWM and SPWM Pulses in dSPACE Platform 106

Figure 4. 21: boost converter and the VSI results: (a) input and output voltages of boost converter; (b) output square and sinusoidal voltage waveforms, and current waveforms VSI. 107

Figure 4. 22: Characteristic curves of the four irradiance profiles for the experimental test are shown as (a) uni-form weather; (b) shading pattern 1; (c) shading pattern 2; and (d) shading pattern 3.. 108

Figure 4. 23: Experimental results under STC: (a) INC-MPPT; (b) P&O-MPPT; and (c) proposed MPPT.. 110

Figure 4. 24: Experimental comparison of three MPPT techniques at the right GMPP of the PSC: (a) conventional INC; (b) conventional P&O; and (c) coordinated PI-MPPT algorithms.. 112

Figure 4. 25: Experimental comparison of the MPPT techniques at Shading Condition 2: (a) INC-MPPT; (b) P&O-MPPT; and (c) Proposed algorithm. 114

Figure 4. 26: Comparative analysis of the algorithms at the left GMPP of the PSC: (a) INC-MPPT; (b) P&O-MPPT; and (c) Proposed algorithm. 116

Figure 4. 27: Experimental results of the proposed VSI: (a) uniform weather; (b) shading pattern 1; (c) shading pattern 2; and (d) shading pattern 3. 117

LIST OF TABLES

Table 2.1: PV Cell Parameters 10

Table 2.2: Comparison between P&O-MPPT Methods 25

Table 2.3: Fuzzy Logic Controller Rules (Radjai et al., 2015) 35

Table 2.4: Comparison of INC Algorithms 37

Table 3.1: Design Parameters of the PV Module 53

Table 3.2: Tuning Gains of the PI-1 and PI-2 60

Table 3.3: Boost converter parameters 69

Table 3.4: Parameters of the VSI 72

Table 3.5: Specifications of the Inverter Elements 75

Table 3.6: Parameters of PR controller 80

Table 4.1: Parameters of PV Modules for Experimental Analysis 109

Table 4.2: Comparative study of simulated parameters among MPPTs 119

Table 4.3: Experimental comparison of the proposed and conventional algorithms 120

Table 4.4: Detail comparison study of the proposed scheme with other algorithms in both Literature and Experimental outcomes 121

LIST OF SYMBOLS AND ABBREVIATIONS

AC	:	Alternating Current
ACO	:	Ant colony optimization
AI	:	Artificial intelligence
ANN	:	Artificial neural network
D_b	:	Blocking diode
D_{bip}	:	Bypass diode
CV	:	Constant voltage
CCM	:	Continuous conduction mode
Li	:	Converter side inductor of the LCL-LPF
IMPP	:	Current at maximum power point
I-V	:	Current versus voltage
C_{DC}	:	DC-link Capacitor
V_{CDC}	:	DC-link voltage
dSPACE	:	Digital signal processing and control engineering
DSP	:	Digital signal processor
IF	:	Diode forward current
d-q frame	:	Direct and quadrature frames
DC	:	Direct current
DC-DC	:	Direct current to direct current
DC-AC	:	Direct current to alternating current
DCM	:	Discontinuous conduction mode
DA	:	Dragonfly algorithm
D	:	Duty cycle
ESR	:	Equivalent series resistance

FOCV	:	Fractional open circuit voltage
FSSC	:	Fractional short circuit current
FB	:	Full-bridge
FLC	:	Fuzzy logic control
GW	:	Gigawatt
GMPP	:	Global maximum power point
GWO	:	Gray wolf optimization
I_g	:	Grid current
L_g	:	Grid side inductor of the LCL-LPF
V_g	:	Grid voltage
HC	:	Hill climbing
INC	:	Incremental conductance Controller
ΔIL	:	Inductor ripple current
LCL	:	Inductor-capacitor-inductor
V_{in}	:	An input voltage of boost converter
IGBT	:	Insulated gate bipolar transistor
K_i	:	An integral gain of PID controller
kW	:	Kilowatt
LDR	:	Light-dependent resistor
R_{Load}	:	Load resistance
LMPP	:	Local maximum power point
LPF	:	Low pass filter
MPP	:	Maximum power point
MPPT	:	Maximum power point tracking
ΔD_{max}	:	A maximum step size of the duty cycle
MOSFET	:	Metal oxide semiconductor field-effect transistor

C_{min}	:	The minimum capacitance of the DC-link Capacitor
MB	:	Model-based
M	:	Modulation index
N_{par}	:	Number of parallel-connected cells in a PV module
M	:	Number of PV module
N_{ser}	:	Number of series-connected cells in a PV module
V_{oc}	:	Open circuit voltage
OSG	:	Orthogonal signal generator
V_o	:	The output voltage of boost converter
PSCs	:	Partial shading conditions
PSO	:	Particle swarm optimization
PIC	:	Peripheral interface controller
P&O	:	Perturb and observe
PLL	:	Phase-locked loop
PV	:	Photovoltaic
I_{pv}	:	Photovoltaic array current
P_{pv}	:	Photovoltaic array power
V_{pv}	:	Photovoltaic array voltage
PMPP	:	Power at the maximum power point (MPP)
$\cos\theta$	:	Power factor
P-V	:	Power versus voltage
K_p	:	A proportional gain of PID controller
K_{PR}	:	A proportional gain of PR controller
PI	:	Proportional integral
PID	:	Proportional integral derivative
PR	:	Proportional resonance

PWM	:	Pulse width modulation
V_{ref}	:	Reference Voltage
K_R	:	Resonance gain of PR controller
RMS	:	Root means square
T_s	:	Sampling time
I_o	:	Saturation current of PV cell
SOGI	:	Second-order generalized integrator
I_{sc}	:	Short circuit current
SPWM	:	Sine pulse width modulation
SEPIC	:	Single-ended primary inductor converter
1-ϕ	:	Single-phase
STC	:	Standard test conditions
SSC	:	Steady-state condition
S	:	Apparent power
SSE	:	Steady-state error
Dd	:	A step size of the output reference voltage of the boost converter
ΔD	:	A step size of the duty cycle
F_{sw}	:	Switching frequency
SRF-PLL	:	Synchronous reference frame phase-locked loop
THD	:	Total harmonic distortion
TS	:	Tracking speed
VSS	:	A variable step size of a duty cycle
VMPP	:	The voltage at maximum power point
VSI	:	Voltage sourced inverter
W	:	Watt
W/m^2	:	Watt/square meter

CHAPTER 1: INTRODUCTION

1.1 Background

Burning fossil fuels leads to increase environmental pollution, for example, an increasing amount of toxic carbon dioxide gas released into the atmosphere (Ebhota & Jen, 2020). Renewable energy sources such as photovoltaic, hydroelectric, and wind power are viable, sustainable, eco-friendly, and renewable (Kalair, Abas, Saleem, Kalair, & Khan, 2020). Renewable energy production is predicted to increase by 6.7% by 2030 (Fatima, Shahzad, & Cui, 2020). The Joint Research Center report revealed that the global installation of PV plants was 315 GW in 2016, with a cumulative increase of 40% annual production over the last 15 years. Therefore, 133.7 billion USD was invested in 2016 alone to produce PV energy, comprising 55% of gross renewable energy cost (A. Ibrahim, Aboelsaud, & Obukhov, 2019). Solar photovoltaic energy is harnessed from a PV array by converting sunlight into electrical energy (Sharma & Puri, 2020). However, solar PV modules have low conversion efficiency (less than 22.5%), a high manufacturing cost of energy, and high dependence on environmental factors (H. Zhang et al., 2020). A grid-tied PV system delivers excess power to a utility grid, which reduces household electricity bills and meets electricity demands (Khezri, Mahmoudi, & Haque, 2020). Recently, many PV systems are integrated with the utility grid because of its increasing demands and reliable operations compared with other renewable sources (Joisher et al., 2020). The non-linear P-V and I-V curves of a PV array are generated when variations have occurred in solar irradiations, temperatures, and loads (Bi et al., 2020).

A maximum power point tracking (MPPT) algorithm is connected between a PV array and DC/DC converter to track maximum power from a P-V curve by perturbing the size of a converter's duty cycle (Darcy Gnana Jegha, Subathra, Manoj Kumar, Subramaniam, & Padmanaban, 2020). A robust MPPT algorithm can continuously supply maximum power from a photovoltaic array to a load, notwithstanding the changing weather conditions (Rakhshan, Vafamand, Khooban, & Blaabjerg, 2018). A significant number of the MPPT algorithms are investigated and applied commercially due to the growing importance of high efficient photovoltaic power generation. (Kumar, Hussain, Singh, & Panigrahi, 2017). An operating point of an MPPT controller moves around the different peaks of the P-V curve to track a maximum power point (MPP) location under different weather conditions on a PV array (Belhachat & Larbes, 2018).

Conventional MPPT algorithms are only reliable under uniform environmental conditions where the P-V curve generates only one MPP (Ji et al., 2010; Wang, Li, & Ruan, 2016). Cloud cover, tall objects, and bypass diodes cause a partial shading condition (PSC) that generates multiple power peaks on the P-V curve (Faldu & Kulkarni, 2020). One of the main challenges of designing MPPT schemes is the need to quickly detect global MPP (GMPP) instead of searching for several local MPPs (LMPPs) under the PSCs (Bollipo, Mikkili, & Bonthagorla, 2020). Conventional perturbation and observation (P&O) algorithm is commercially used as Hill Climbing (HC) MPPT scheme, which can be implemented without any complexity (P. Singh, Palwalia, Gupta, & Kumar, 2015). However, one of the significant drawbacks of the P&O MPPT method is that oscillations around a peak power point of the P-V curve at the steady-state condition (SSC) are continuously substantial in an amount under standard testing condition (STC) of weather. A conventional Incremental Conductance (INC) MPPT algorithm is used to mitigate the disadvantages of the P&O MPPT at the STC environmental circumstance (Rouibah et al., 2020).

The location of an operating point and maximum power points (MPPs) is dynamically changeable when the PSCs condition occurred on the PV module. Hence, an online Maximum Power Point Tracking (MPPT) algorithm is required to harness the maximum energy from a PV array by driving the operating point toward the nearest of a global MPP (GMPP) region (Bouchakour, Borni, & Brahami, 2019). The traditional P&O-MPPT algorithm performs poorly against the change of solar irradiance and temperature under partial shading conditions (PSCS). The conventional INC-MPPT technique stops searching for an operating point value after detecting a global MPP without leaving power oscillations at no partial shading conditions (PSCs). However, the INC-MPPT algorithm cannot remove power fluctuations around the GMPP location, degrading tracking and conversion efficiency of a PV array under the PSCs. Furthermore, computational burden and execution time of the INC-MPPT algorithm are increased when small sampling frequency is selected (A. O. Ibrahim & Basir, 2013). A PI-based P&O-MPPT algorithm is developed to maintain constant output voltage of a converter, and tracking a MPP location on a P-V curve with reduced power oscillations (Kabalci, Gokkus, & Gorgun, 2015). A P&O-based voltage regulation loop is designed with a proportional integral derivative (PID) controller to increase the tracking speed of the MPP and regulate the output reference voltage faster than the conventional P&O algorithm (Khaled, Aboubakeur, Mohamed, & Nabil, 2018). However, the PI-based P&O-MPPT and INC-MPPT algorithms cannot track a GMPP location when it lies on the left most corner or middle on partially shaded P-V curves. Therefore, this work aims to present and implement a coordinated PI-MPPT technique to overcome inaccurate operations in the conventional algorithms under the PSCs (Motahhir, El Hammoumi, & El Ghzizal, 2018).

1.2 Problem Statement

A study found that average income families cannot afford to install costly PV panels in their houses. The average efficiency of extracting power from installed PV modules is between 9% and 17%, and of this, preliminary studies suggest that 47% is accounted for by inefficiencies in power tracking systems and 36% is accounted for by others (Kafui, Seres, & Farkas, 2019). Therefore, the credence is that by utilizing much more effective and accurate MPPT techniques, PV systems' energy turnover is effectively increased. An increase in energy absorption efficiency increases investors' attention to install more solar PV systems (Heinisch, Odenberger, Göransson, & Johnsson, 2019).

Cloud cover, trees, buildings, and bypass diodes cause a partial shading condition (PSC) with numerous power peaks on the PV string (Kermadi & Berkouk, 2015). A tradeoff between the size of a duty cycle perturbation, slow tracking speed, and power oscillations around GMPP under partial shading conditions (PSCs) is a common problem faced by an MPPT algorithm when tracking the GMPP location on a P-V curve (Bhattacharyya, Samanta, & Mishra, 2020). Once a converter duty cycle's perturbation size increases, tracking speed goes down, but the power oscillations increased, and it causes a more significant power loss. Similarly, tracking speed is slower if the step size of the converter's duty cycle is minimal. Due to this unforeseen relationship between tracking speed and power oscillations, a variable step perturbation is applied to achieve a higher efficiency in photovoltaic MPPT design (H. Islam et al., 2018). Many online and offline MPPT controllers are ineffective in tracking a GMPP on a non-linear P-V curve under PSCs, which degrades the PV system's efficiency because of the slow tracking speed, high power oscillations, and low convergence speeds (Joshi & Sharma, 2018).

A PI-based INC-MPPT algorithm was designed to remove a dilemma of choosing the step size of the converter duty cycle under abruptly changing solar irradiance and temperature (Patel & Tiwari, 2017). An improved hill-climbing double closed-loop algorithm was deployed nearer to the MPP to reduce steady-state oscillations and a rise time when solar insolation is in dynamic condition (Y. Liu et al., 2019). An adaptive

PID controller with the P&O MPPT algorithm for a PV system is proposed (Sahoo, Samanta, & Bhattacharyya, 2020) to improve tracking time and reduce oscillation around MPP. In (Anto, Asumadu, & Okyere, 2016), PID-integrated P&O MPPT is proposed for a grid-connected PV system. These developed MPPT schemes' main constraints are making delays in the tracking MPP and generating more significant power oscillations because their operating points are lost to the local MPPs (LMPPs) under PSCs (Lyden, Haque, Gargoom, & Negnevitsky, 2013). By taking into account the drawbacks of the previously developed MPPT techniques, in this study, a PI-based coordinated MPPT technique is proposed for a grid-tied PV system to improve tracking speed and reduce power oscillations of a PV array under PSCs (Motahhir et al., 2018). Harmonic components, frequency instability, and out of phase between a voltage sourced inverter (VSI) and grid waveforms of voltage and current are common problems in a grid-tied PV system (Palanisamy & Vijayakumar, 2020). A simple synchronous reference frame phase-locked loop (SRF-PLL) in the VSI control is used to maintain the same phase and frequency of voltage and current between the VSI and grid sides (Xia, Zhang, Tan, & Liu, 2020).

1.3 Objectives of the Study

This research aims to increase the efficiency of the photovoltaic system by introducing a coordinate PI-MPPT algorithm. This study also focuses on designing a controller and synchronization technique to control a grid-connected full-bridge (FB) voltage sourced inverter (VSI) and deliver active power to the utility grid with unity power factor under uniform weather and the PSCs. The specified objectives of the research work are as follows:

- To investigate a coordinated PI-MPPT technique.

- To design a highly efficient control method for a grid-connected voltage source inverter (VSI) with unity power factor and minimal computational complexity.
- To develop a laboratory setup for the proposed MPPT algorithm with PV simulator, DC/DC boost converter, and the grid-tied inverter (the VSI).
- To validate the developed grid-connected PV system experimentally.

1.4 Methodology

The methodology is outlined at five stages in this research work. The background, problem statements, and research objectives of this research work are explained in detail in the first stage.

Chapter 2 includes an overview of renewable and solar energies with their environmental impacts. Various contingency analyses of MPPT techniques and their implementation steps are discussed. The study is carried out on online and offline MPPT algorithms to know their features of tracking speed, execution time, and power oscillations. The study also investigates how to find a more robust MPPT technique to improve the PV system's overall efficiency. Many DC-DC converters such as buck, boost, and buck-boost converters are reviewed to find an efficient DC-side control technique. Several control techniques for the voltage source inverter (VSI), such as phase-locked loop (PLL) and proportional resonance (PR) controllers, are also investigated to find out an efficient technique for controlling the grid-connected PV system with a unity power factor.

In chapter 3, the modeling of the grid-connected PV system is categorized into three major parts. Firstly, identifying exact circuit components such as switches, sensors, and converters is viable in enhancing the photovoltaic plant operation's reliability, whose failure may result in power dissipation of system elements and hence decrease system security. Malfunction and misalignment of the components can cause permanent damage to the system's equipment. Moreover, upon identifying the components for monitoring MPPT features under the PSCs and variances, the tracking speed and steady-state power oscillations are investigated as a crucial part of the study. Furthermore, an efficient control and synchronization technique of the VSI is modeled to synchronize voltage and current between the PV and utility grid sides.

In chapter 4, simulation and experimental works are carried out to validate the grid-connected PV system. This stage consists of three main parts. Firstly, condition monitoring of an adequately designed PV system, DC-DC boost converter, full-bridge VSI, and the proposed MPPT charge controller by simulation study with the software MATLAB is performed. For the proposed converters, duty cycle, PWM, and SPWM signals are outlined. A dynamic study of the PV system is carried out in MATLAB to detect a wide range of disturbances on the partially shaded P-V curves. The VSI control system's performance is investigated by monitoring output voltage and current waveforms synchronized with the utility grid at unity power factor.

Moreover, a laboratory setup is performed for the proposed MPPT algorithm with a PV simulator, boost converter, VSI controllers, sensors, dSPACE controller, power supply units, oscilloscopes, and load. A series of experimental tests are carried out to test the performance of the proposed MPPT technique. The output characteristics of the grid-tied PV system is tested under acute weather and three PSCs. The operation of three significant types of MPPT techniques with their tracking components and performance are discussed. A detailed comparison is performed among the MPPT schemes with tracking parameters such as tracking speed, design complexity, power oscillations, and cost-effectiveness.

Some recommendations for shortcomings and future work on the presented research work are highlighted in the final stage. A dissertation report of this research work is written by highlighting the findings and sending the report to the grant's respective authority. This report includes a detailed literature review, mathematical modeling of the designed system, simulation, and experimental analyses of the proposed grid-connected PV system and MPPT controller. Figure 1.1 shows a detailed explanation of the research activities.

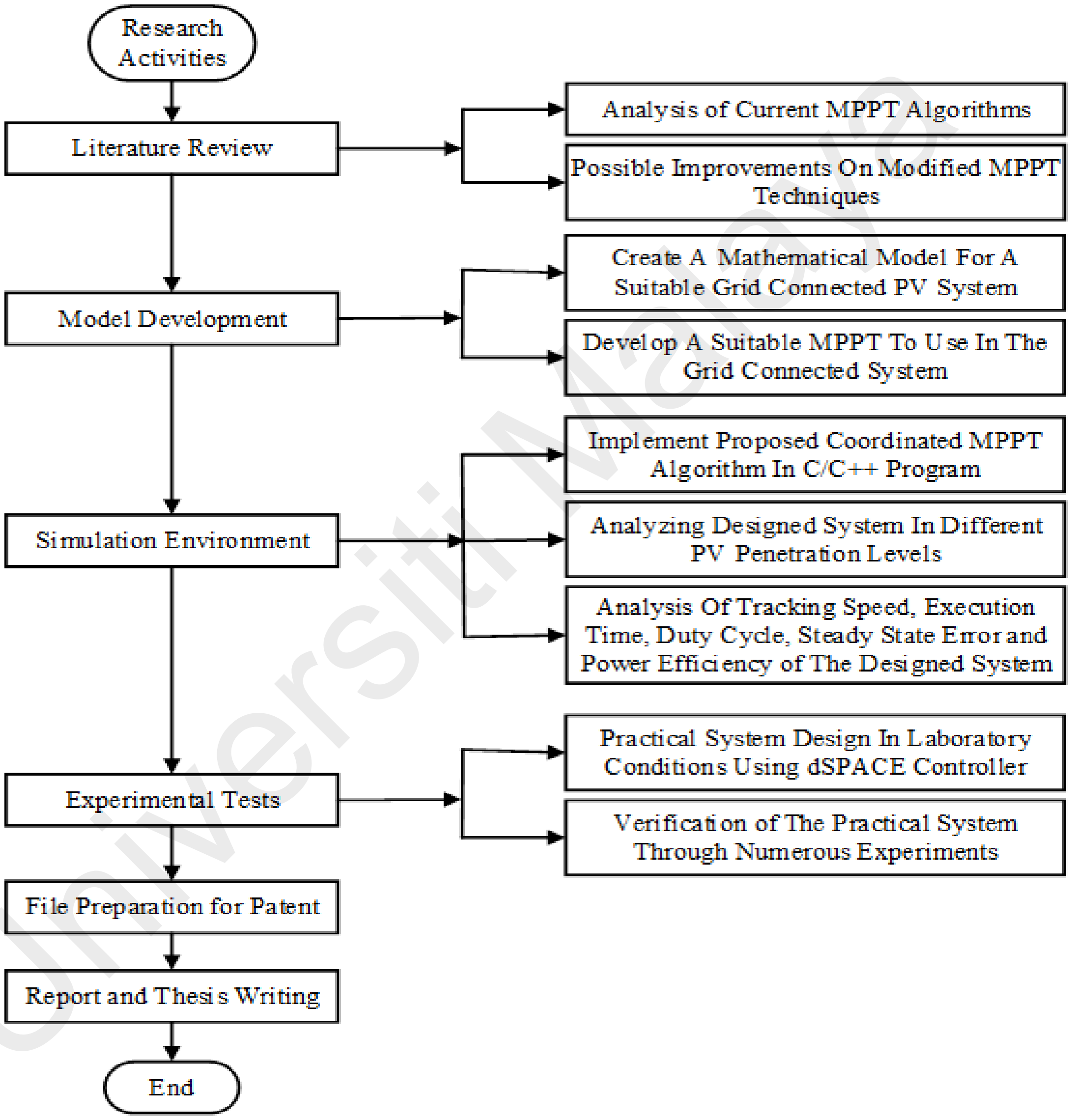

Figure 1. 1: Flowchart of Research Activities

CHAPTER 2: LITERATURE REVIEW

2.1 Introduction

Chapter 2 includes a literatue review on solar energy and its impacts on the environment and reviews on a grid-tied PV system. This study provides a whole concept of non-conventional energy sources. Various contingency analyses of MPPT techniques are outlined in this review part. A Study is taken on traditional and hybrid MPPT algorithms (online and offline) to know the characteristics of the tracking speed, execution time, and oscillations in the vicinity of GMPP. Techniques to improve various modified MPPT methods are also compared. An analysis of different power converters is evaluated with their efficiency and overall performance in tracking GMPP location on the power-voltage (P-V) curve. A further study is undertaken to find a more robust control and precise MPPT technique to improve the overall PV module's efficiency. This review also highlights the difference between power stages, control mechanisms, and synchronization techniques of photovoltaic solar modules associated with the utility grid.

2.2 PV Array Modelling

PV array is modeled by considering different weather conditions to investigate an appropriate MPPT controller (Winston, Kumaravel, Kumar, & Devakirubakaran, 2020). In modeling, selecting the PV array parameters' accurate size is challenging when the PV system is operated under uniform weather and the PSCs (Bonthagorla & Mikkili, 2020).

$$I_{cell} = I_{cell}N_{par} - I_o N_{par}\left[\exp\left(\frac{V_{cell} + R_s\left(\frac{N_{ser}}{N_{par}}\right)I}{V_t \alpha N_{ser}}\right) - 1\right] - \frac{V_{cell} + R_s\left(\frac{N_{ser}}{N_{par}}\right)I_{cell}}{R_p\left(\frac{N_{ser}}{N_{par}}\right)} \quad (2.1)$$

Where I_{cell} is the current of an individual PV cell that is proportional to the solar irradiance, V_{cell} is the voltage across each PV cell, I_o is a reverse saturation current of the PV cell, q is an electron charge, α is an ideality constant of Shockley diode, V_t is the thermal voltage of a PV array, N_{ser} is the number of series-connected PV cells, N_{par} is the number of parallel-connected PV cells, R_s is the series resistance of the PV cell and R_p is a parallel resistance of the PV cell. The PV cell parameters are shown in Table 2.1. A PV cell acts as a current or voltage source based on an operating point's location to track an MPP on a P-V curve (Villalva, Gazoli, & Ruppert Filho, 2009). Eq. (2.1) shows a current of a PV cell. Figure 2.1 shows an internal circuit diagram of a PV cell applying a current source (I_m) and PV array current (I_{pv}).

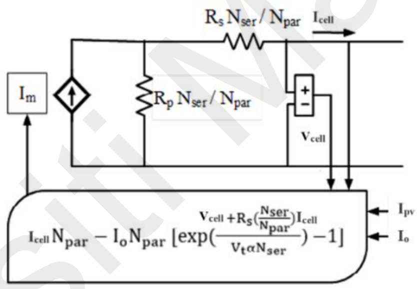

Figure 2. 1: Diagram of a photovoltaic cell (Villalva et al., 2009)

Table 2.1: PV Cell Parameters

PV cell Parameters	Simulation for 1.5 kW (ISoltech 1STh-250-WH)	Experimental for 213.55 W (Atlantis System SS125LM)
PV Cell Current (I_{cell})	8.15 A	4.91 A
PV Cell Voltage (V_{cell})	30.7 V	2.9 V
Light Current (I_L)	8.7106 A	5.2225 A
Temperature Coefficient	0.086998 (%/°C)	0.029 (%/°C)
Diode reverse current (I_o)	4.1601*e-10 A	3.1918*e-11A
Electric charge (q)	1.60217×10^{-19} C	1.60217×10^{-19} C
Boltzmann constant (k)	1.38065×10^{-23} J/k	1.38065×10^{-23} J/k
Diode ideality (α)	1.019	0.92984
Series resistance (R_s)	0.23724 Ω	0.077509 Ω
Parallel resistance (R_p)	224.1886 Ω	91.9399 Ω
Temperature (T)	K	K
Thermal Voltage (V_t)	V	V
Series-PV cells (N_{ser})	6	15
Parallel-PV cells (N_{par})	1	1

Figure 2.2 shows the three sets of P-V and I-V curves at room temperature (25°C) and uniform solar insolation. The MPP_1, MPP_2, and MPP_3 are individually generated from 1000 W/m^2, 800 W/m^2 and 200 W/m^2 Solar irradiances. Figure 2.3 depicts a PV array's characteristics under a partial shading condition (PSC) that generates a GMPP and three LMPPs on the P-V curve.

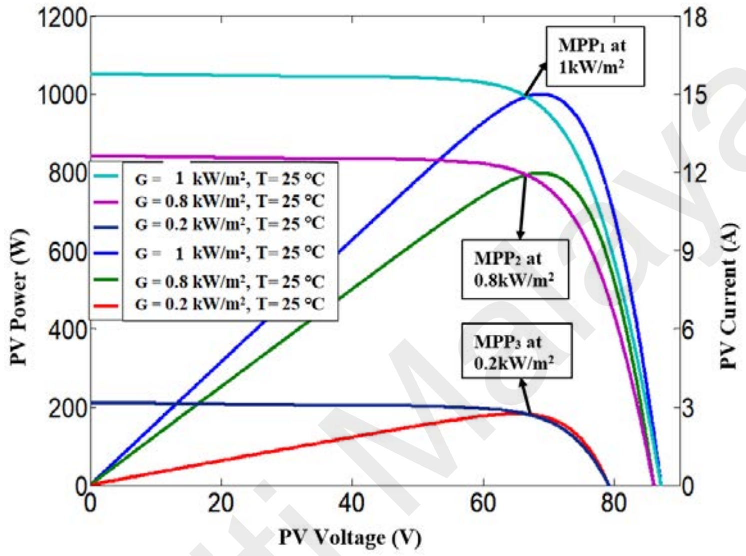

Figure 2. 2: P-V and I-V curves at changing solar irradiances

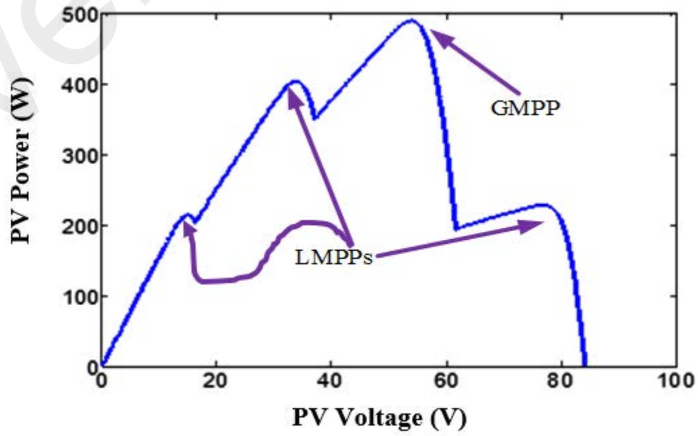

Figure 2. 3: P-V curve at PSCs

Figure 2.4 demonstrates an I-V curve of a PV array at the PSC considering an ambient temperature of 25 °C, generating voltage (V_{pv}) and current (I_{pv}) coordinates for the LMPPS and the GMPP locations as shown in Figure 2.3. For example, I_{MPP} and V_{MPP} are the current and voltage of the GMPP location, respectively.

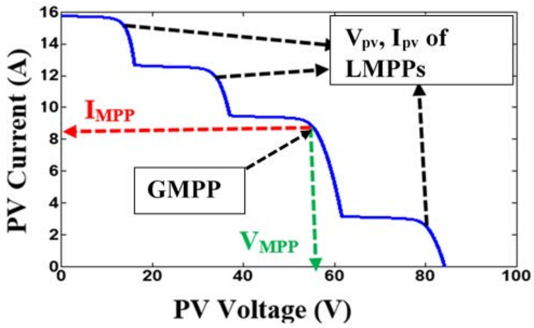

Figure 2. 4: I-V Curve at PSCs

2.3 Impacts on PV System

An increased number of low efficient photovoltaic power plants are integrated nowadays with an electric grid, which makes some risks of controlling power system network. Therefore, a comprehensive study of the PV array is essential to investigate its adverse impacts on the grid network. This subtopic includes an overview of a PV module's state of affairs at different weather conditions and outlines the root causes of many negative impacts on the PV system. A PV array produces power loss when its tilt angle is not directed toward sunlight and due to soiling effect, snow layers, bypass diodes connection, and load variations.

2.3.1 PV Panel Tilt and Orientation

A moveable Sun Tracker (ST) used with the PV panel can increase daily energy production by 43.87% compared with a fixed system (Despotovic & Nedic, 2015). A dual-positioned ST-MPPT in a solar panel can improve energy production 40% more than the fixed-tilt collectors. However, the ST tracker is not recommended for small solar collectors, especially in residential applications or in hot climate zones, due to its high design cost and high internal energy consumption (5– 10%) (Awasthi et al., 2020).

For the fixed installation of a PV plant without ST, deviation of the tilt angles throughout the year reduces gross output power under non-uniform solar insolation levels. The installed PV panel's surface is adjusted to be perpendicular to the sunlight to reduce the fluctuating trends of the PV array's output power because of Sun dynamics and moving cloud coverage. An optimum tilt angle of the PV array can be set for summer and winter, and the azimuth angle can vary from east to west during the day, but it increases cost and complexity (Esfahani et al., 2020).

2.3.2 Soiling Effect on PV Array

Soiling consists of debris such as tree leaves, bird droppings, the dust of vehicular exhaust, airflows, and volcanic eruptions. Figure 2.5 shows the factors of dust accumulation on the surface of the PV panel. The worst dust materials are desert (e.g., Sahara) sand and polluted soil found in Middle Eastern and North African countries such as Libya (Li, Mauzerall, & Bergin, 2020).

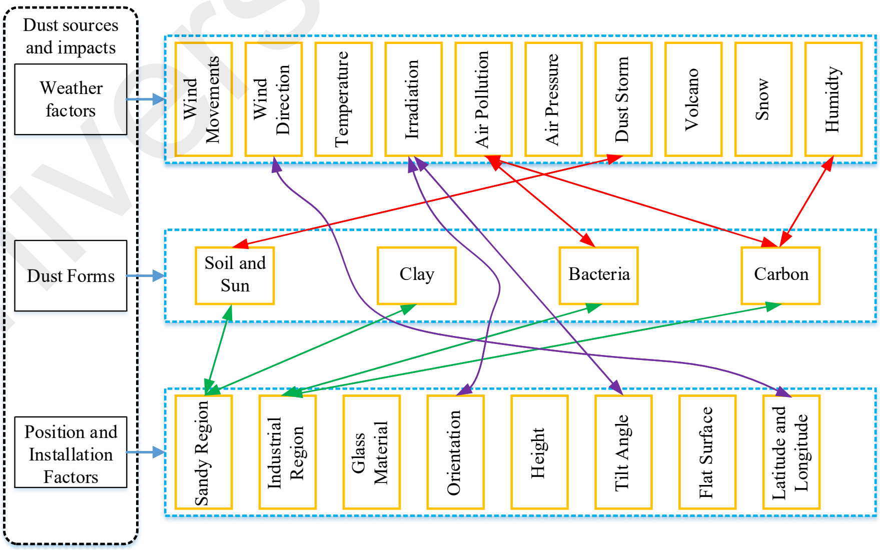

Figure 2. 5: Factors of Dust on PV Modules (Maghami, Hizam, Gomes, Radzi, Rezadad, Hajighorbani, et al., 2016)

The performance of the PV module is degraded by environmental factors especially soiling (causes a 2–50% power loss), scattering effects of the solar irradiance (Maghami, Hizam, Gomes, Radzi, Rezadad, & Hajighorbani, 2016; Saidan, Albaali, Alasis, & Kaldellis, 2016) and blocked sunlight. A study conducted on 204 sites in California found that efficiency degradations during uniform weather with no rainfall were 0.2% daily and 1.5–6.2% annually (Maghami, Hizam, Gomes, Radzi, Rezadad, & Hajighorbani, 2016).

2.3.3 Snow Effect on the PV Array

PV systems are well-developed for use in temperate regions regardless of their low solar illumination, especially in Northern European countries, and frequent snowfall in Northern America, Canada, Japan, and Germany (Heidari, Gwamuri, Townsend, & Pearce, 2015).

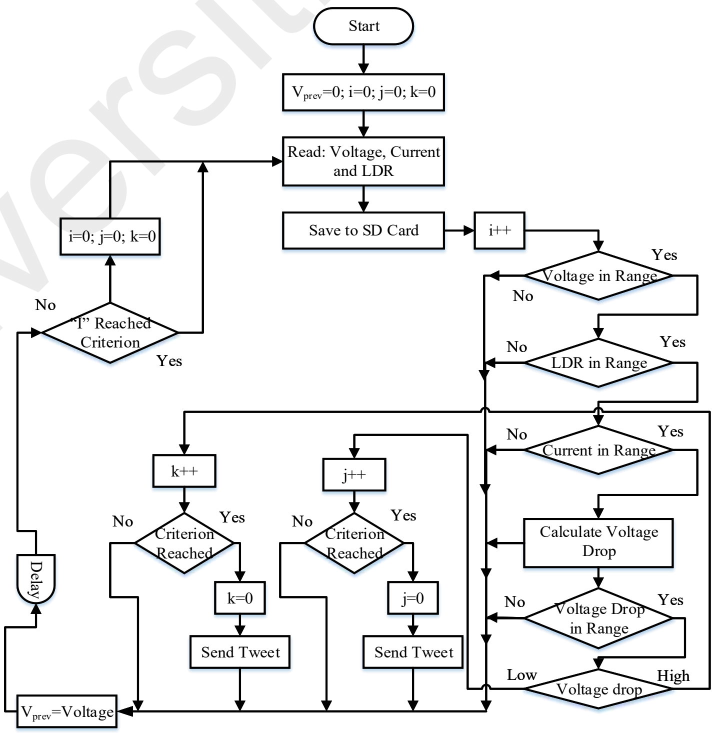

Figure 2. 6: An Algorithm to Detect Snowfall (Seyedali Meghdadi & Tariq Iqbal, 2015)

Snow degrades the PV-generated power in three ways; through wave diffusion, albedo reflection on neighboring PV modules, and conduction with snowless modules (Yan, Qu, Chen, & Feng, 2020). Power loss due to the snowfall is directly influenced by PV modules' tilt angles and the level of ground interference (Hashemi, Cretu, & Taheri, 2020). A study found that power loss in a year due to snowfall was more than 15% on low tilted PV modules. In Germany, power loss was from 0.3% to 2.7% for an unshaded rooftop module at a 28° angle (Heidari et al., 2015). A cost-effective snow detection method was applied to a solar PV module for three months in St. John's, Newfoundland, Canada. The module was composed of an Arduino controller connected with a Wi-Fi combined with a light-dependent resistor (LDR) to measure the output voltage, current, and solar insolation. A Twitter message is sent to the owner if the snow accumulation is more than 5 cm, based on the algorithm shown in Figure 2.6 (Seyedali Meghdadi & Tariq Iqbal, 2015).

2.3.4 Bypass and Blocking Diodes Effects

A PV cell is open-circuited or fully damaged if it dissipates more than the maximum tolerated power in the hot-spot stage of the PV array under the PSCs (J. Teo, Tan, Mok, Ramachandaramurthy, & Tan, 2020). Figure 2.7 shows bypass diodes ($D_{bip\,1}$ to D_{bip4}) are connected across each PV module (M_1 to M_4), and a blocking diode (D_b) in series with a battery.

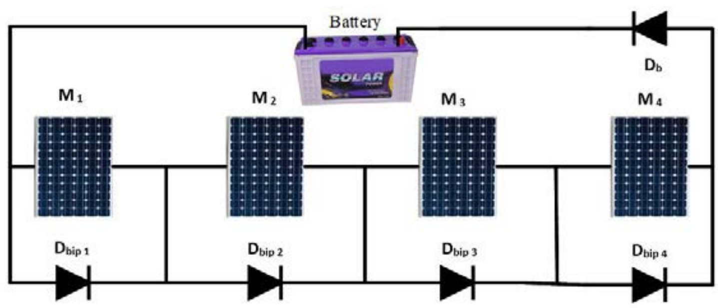

Figure 2. 7: Bypass and Blocking Diodes (Yunmei & Xiangwei, 2019)

The bypass diodes start functioning if 20% of a PV module is shaded to reduce power loss because of a substantial current flow through them (J. E. Lee et al., 2016). By contrast, a shaded PV cell can be excluded using a bypass diode (D_{bip}) to continue power supply by the remaining PV cells, which maximizes the efficiency of the PV system (H. Mohammed, Kumar, & Gupta, 2020). The bypass diode cannot protect the PV modules from being damaged when a copper indium gallium selenide (CIGS) is used in thin-film PV cells (Voswinckel, Mikolajick, & Wesselak, 2020).

2.3.5 Load Effects on PV Array

The nonlinearity of a load occurs in a PV system when load impedance is changed because of a PV panel's voltage change. An impedance variation in a sinusoidal voltage source produces a nonlinear load current that contains several harmonic components. Hence, overcurrent flow through a load damages the devices and circuit components in a power system's distribution side. The level of harmonic distortion is minimized by selecting a large switching frequency when an inductive load is connected to a PV system. Nonlinear loads can also be identified during the transition period of the active switching time (Nazir, Kumar, Pal, Singh, & Panigrahi, 2020). Incremental voltage slope (dV) and current slope (dI) in the I-V curves are positive and negative when a change of load resistance occurs in the PV array. Thus, an operating point of an MPPT controller shifts away from a GMPP location.

A new duty cycle of a DC-DC converter is selected to bring the operating point closer to the GMPP location during a varied load condition (Jana, Kumar, Mishra, Sen, & Saha, 2020). Eq. (2.2) shows a formula is used to calculate a new duty cycle throughout load variations. A load variation is detected in a modified INC-MPPT technique if the paths of voltage and current fluctuations are different. Thus, a load-variant subroutine is started functioning to carry out the operating point closer to the

GMPP location. Conventional MPPT algorithm requires a long period of tracking time to return to a local maximum power point (LMPP) location on a P-V curve once the load resistance is decreased from 10 Ω to 5 Ω (Tey & Mekhilef, 2014).

$$R_{load} = \frac{D^2}{(1-D)^2} \cdot \frac{V_{pv}}{I_{pv}};\ D = \frac{\sqrt{\alpha}}{1+\sqrt{\alpha}} \tag{2.2}$$

2.4 Performance Analysis on MPPT Control Variables

In this section, an MPPT controller's performance is evaluated with its important parameters such as tracking speed, dynamic weather response, steady-state error (SSE), and robustness to interferences.

2.4.1 Dynamic Weather Response to PV System

PV panels on cloudy days are experienced with a fast dynamic change of solar insolation. Under such circumstances, a PV panel receiving low solar irradiation acts as a load and creates hotspot regions in the PV cells. This dynamic weather condition on a PV array makes a slow process of delivering maximum power to a load and downgrades the whole PV system's efficiency. A bypass diode is connected across each PV module to remove a hotspot area from a PV panel in dynamic weather conditions. However, many MPPT algorithms' operating points cannot search for a maximum power point among multiple peaks on the P-V cure under dynamic weather change (Ram et al., 2018).

2.4.2 Steady-State Error (SSE)

An ideal control system of an MPPT algorithm always maintains an operation point of a converter at an optimal power point regardless of weather condition on a PV array. However, a modified MPPT algorithm is deployed to keep an operating point location nearest to maximum power point in dynamic weather conditions, which removes the steady-state error. Tracking GMPP by an MPPT algorithm is related to how the perturbation size of predefined voltage and duty cycle sets. Thus, an operating point is seen revolving around the GMPP, which results in continuous power oscillations at the steady-state condition (SSC) depending upon a change in the amount of predetermined perturbation size. The small selection of a perturbation step size of a duty cycle, the more accuracy is found in the control variables of a solar PV panel at the SSC (Huang et al., 2017).

2.4.3 Robustness to Disturbances

MPPT controllers of a PV system require a precise and robust response against unpredictable weather conditions. Different types of PV models manufactured by different companies show distinct characteristics against a PV module's disturbance control. Therefore, it's necessary to use a robust MPPT control scheme to withstand any disturbances.

2.4.4 The efficiency of a Large Power Capacity

Efficiency gives us an idea of how much a developed MPPT technique can track an MPP location on a P-V curve. A high efficient MPPT algorithm tracks a GMPP at different solar insolation levels; however, this is somewhat difficult to achieve during the worst weather change. A PV array's efficiency is obtained by calculating a percentage ratio between tracked power and an actual nominal power of a PV system as represented in Eq. (2.3). Smooth tracking of the GMPP enhances the overall efficiency of a designed PV system by a robust MPPT algorithm at any dynamic weather condition (Husain, Tariq, Hameed, Arif, & Jain, 2017). However, the PV system's overall efficiency is degraded when uncontrolled power oscillations around a GMPP region are detected by an operating point of an MPPT algorithm on a PV array (Karami, Moubayed, & Outbib, 2017). For instance, the low efficiency of the fractional short circuit current (FSCC) algorithm is measured when a repeated tuning method of a duty cycle of a boost converter is applied in switching ON and OFF of its IGBT or MOSFET. The high efficient PV system is found when an intermittent periodical method of perturbing duty cycle and a scaled selection of a control variable are applied at PSCs and solar insolation change respectively (Husain et al., 2017).

$$\eta = \frac{\text{Power Tracked}}{V_{mpp}\ I_{mpp}} \tag{2.3}$$

2.4.5 PSCs Handling

PV systems can be wholly or partially shaded by a flying object, large trees, and tall buildings, which results in many MPPs occurrence on a P-V curve. An MPPT in a shaded P-V curve tracks an undesired local MPP (LMPP) rather than a GMPP, which results in significant power losses (Ezinwanne, Zhongwen, & Zhijun, 2017). In a PV string under PSCs, voltage mismatches can occur between the shaded and non-shaded PV modules, which leads to a more significant power loss. A voltage equalizer, a DC/DC converter, and a micro-inverter are integrated with an MPPT technique to handle a partial shading condition in a PV system. Micro-inverters are usually interconnected in each module to accurately control the PSCs, increasing cost and complexity because it requires many stages of power conversion in a PV system (Uno & Kukita, 2014).

2.4.6 Power Oscillation Near MPP Location

In most online MPPT schemes, power losses are mainly occurred because of massive power oscillation at the vicinity of a GMPP location. A large step size of a fixed duty cycle perturbation increases the tracking speed and causes huge power oscillation around the GMPP (Mirza, Mansoor, Ling, Yin, & Javed, 2020). These power oscillations can be extreme if an operating point of a conventional MPPT algorithm continuously searches for an MPP location on the P-V curve, although the MPP is tracked earlier (Sher et al., 2015).

2.4.7 Tracking Speed

A tracking speed is defined as how fast a GMPP of a P-V curve is tracked with a different duty cycle perturbation size. Fast and accurate tracking speed is attainable by tuning a perturbation step size of a duty cycle and calculating a distance from an operating point of an MPPT controller to the MPP location on a P-V curve (Karami et al., 2017). Many improved MPPT methods are suitable for getting a high tracking speed in a dynamic weather condition. For example, a modified firefly MPPT algorithm has a higher tracking speed than an ordinary particle swarm optimization (PSO) algorithm (Seyedmahmoudian et al., 2016).

2.4.8 Convergence Speed

Convergence speed is the time required to obtain an MPP location from the P-V curve. An MPPT algorithm delays tracking a GMPP location when the magnitude of the voltage, current, and power points are changed on the P-V and I-V curves because of a sudden increase in solar insolation and the PSCs. Hence, numerous power losses and a slow convergence speed of the operating point are measured in a PV system (Shams, Saad, & SOON, 2020). The convergence speed in offline and online MPPT techniques is generally high and low, respectively, when an operating point reaches close to a P-V curve's global peak. A convergence time of an efficient MPPT algorithm must be as shorter as possible (Ezinwanne et al., 2017).

2.5 Types of MPPT Techniques

Three main types of conventional, modified and hybrid MPPT techniques are drawn in this section. Figure 2.8 shows the types of some improved and hybrid INC, P&O and other MPPT algorithms.

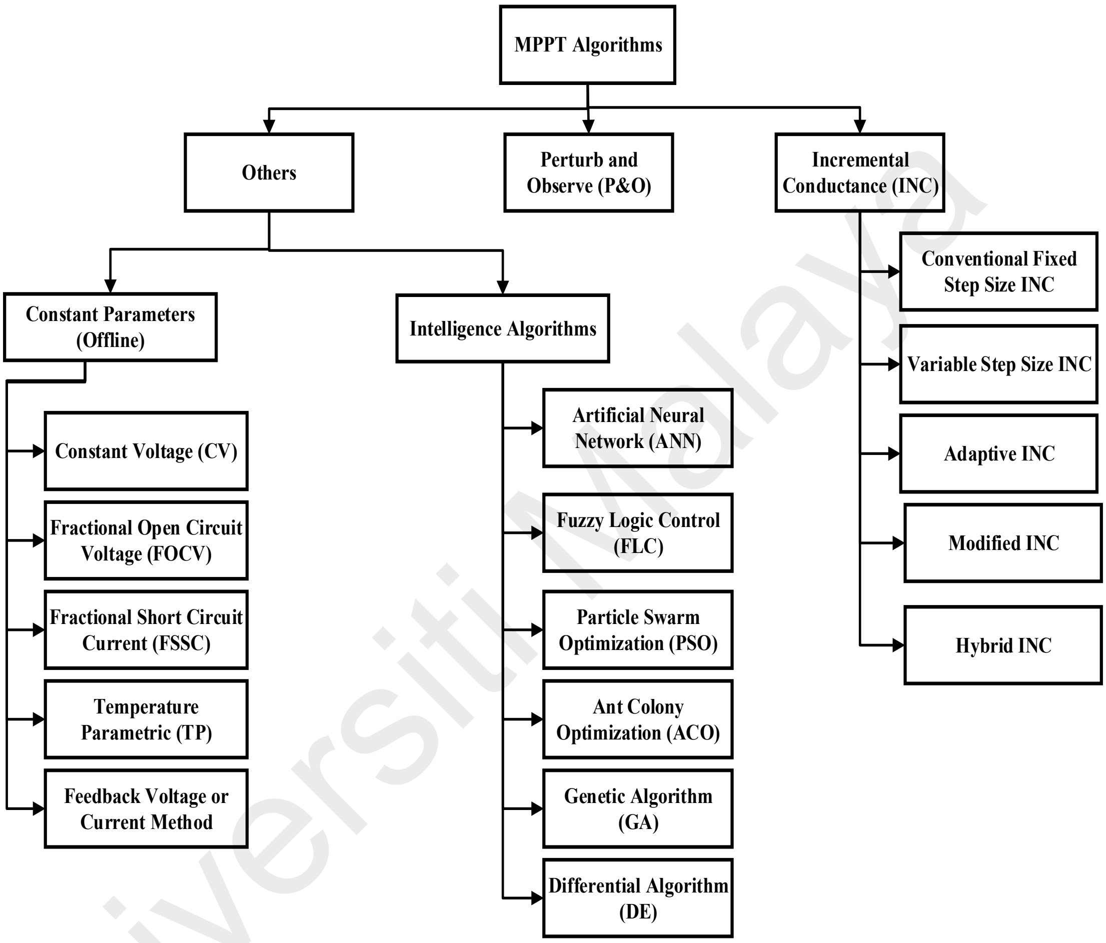

Figure 2. 8: Types of MPPT Schemes

2.5.1 Others MPPT Algorithms

This section presents several other MPPT methods with their pros and cons, tracking issues, expenses, and computational burden. The classification of the MPPT approaches is relied on the number of their control parameters, sensing devices, tracking capabilities and so forth. A comparative study is presented in this section to understand each discussed algorithm's behavior and performance, how to address the problems such as transient and steady-state errors in the PV system. Constant parameters based MPPT algorithms are offline MPPT schemes such as fractional short circuit current (FSCC) and fractional open-circuit voltage (FOCV) are suitable to maintain high efficiency operated by more direct analog or digital technologies in finding MPP. Since no permanent and stable condition exists in the environment, these offline techniques require a discontinuity of the PV panels while an operating point pretends to be closer to the GMPP. But a more significant power loss is attained due to the halt in sending power to the designed circuit while measuring the current and voltage variables of the offline algorithms. As long as these offline MPPT schemes are less efficient and failed to track an actual MPP at PSCs, they are not recommended to apply in an intricate design system (Smadi & Rana, 2020). The offline tracking techniques' main disadvantage is low accuracy so that they are only used in the least powered PV system in uniform environmental cases (Kamarzaman & Tan, 2014). Although the FOCV method does not always reach a real MPP, the system can be operated without a digital signal processor (DSP) or microcontroller, which results in a comfortable and cheap implementation for the system. However, during the tracking process, the measurements are taken periodically by disconnecting the arrays from the load, which results in the system power loss (Hua, Fang, & Chen, 2016).

2.5.2 P&O MPPTs

Conventional perturb and observe (P&O) MPPT scheme is considered a type of a hill-climbing (HC) algorithm. When the difference between instant power $\mathrm{P(k)}$ and actual power, $\mathrm{P(k-1)}$ is positive ($\mathrm{dP/dV} > 0$), the direction of an operating point is located towards the GMPP and vice versa. The perturbation of a PV voltage and current continues in both positive and negative directions on a P-V curve (Bendib, Belmili, & Krim, 2015; Deshpande, Patil, & Deopare, 2016, April; Saravanan & Babu, 2015, March). The P&O algorithm's drawbacks are the occasional tracking deviation from the GMPP region, slow tracking speed, and much oscillation around the GMPP under PSCs (Bendib et al., 2015). Performance of the P&O-MPPT is improved by accelerating the PV system's tracking speed in a steady-state condition when a reference variable's small perturbation size is selected in uniform weather conditions (Saidi & Benachaiba, 2016). A modified P&O with a fixed step size of its duty cycle is then introduced to reduce a tradeoff between steady-state oscillations and tracking speed by adjusting a scaling factor (Ashique, Salam, & Ahmed, 2015, October). To overcome the tradeoff, a conventional adaptive P&O is introduced, however, the problem is remained same because of its dependency on a pre-declared step size of a duty cycle and fluctuating open-circuit voltage (Voc) under PSCs (Abdelsalam, Massoud, Ahmed, & Enjeti, 2011). Moreover, an adaptive P&O with a variable step-sized perturbation of a reference variable is developed to improve tracking efficiency and convergence speed, in which an adaptive perturbation of a duty cycle (ΔD) and period (T) is determined to observe a load current (Y. Jiang, Qahouq, & Haskew, 2012). The adaptive perturbation brings an operating point closer to GMPP based on the estimation of a fractional short circuit current (Isc), and the variable perturbation reduces power oscillations towards the GMPP (Kollimalla & Mishra, 2014). The performance of the conventional and adaptive P&O algorithms is worsened because of a drift (an operating point moves towards only positive or negative direction onto multiple P-V curves if solar insolation is increased or decreased) occurrence when the ΔD is not accurately selected with the enormous change of its perturbation size (Killi & Samanta, 2015). The P&O algorithm consistently searches for multiple MPPs toward the front and back of a P-V curve, thereby resulting in power oscillations in the steady-state condition (Ahmad, Rashid, Ferdowsy, Islam, & Mahmood, 2015; Sher et al., 2015). The power oscillations are reduced by selecting the smallest step size of a duty cycle, but the tracking speed is decelerated (Shebani, Iqbal, & Quaicoe, 2016; Sher et al., 2015). A fractional short-circuit current (FSCC) algorithm first measures an operating point value and sends it to the online P&O algorithm. This method exhibits a high tracking speed and fewer power oscillations around the MPP at PSCs (Sher et al., 2015). Moreover, a modified P&O-MPPT with the fixed and adaptive perturbation size of a duty cycle is applied to remove drift problem by moving an operating point adjacent to the MPP and increasing the duty cycle (D), and positive values of incremental current (dI) and voltage (dV) of the I-V curve (Killi & Samanta, 2015). A PSO-P&O algorithm is deployed to improve tracking efficiency, convergence speed, and steady-state response and reduce the searching space of the MPP. In the PSO-P&O algorithm, P&O consistently searches for a unique MPP under uniform environmental conditions and tracks a local MPP at non-uniform environmental conditions (Manickam, Raman, Raman, Ganesan, & Nagamani, 2016; Sebtahmadi, Azad, Kaboli, Islam, & Mekhilef, 2018). Then, the PSO technique is employed to regulate the perturbation size of the duty cycle at the PSCs' instant (Manickam et al., 2016; K. T. K. Teo, Lim, Chua, Goh, & Tan, 2014, December). An adaptive P&O-FLC algorithm is applied to obtain a high tracking accuracy and reduce computational time without requiring a peripheral interface controller (PIC). The P&O-FLC technique improves system performance in dynamic weather conditions by driving an operating point toward the MPP and increasing the step size of the duty cycle at the direction of the MPP (Radjai, Gaubert, Rahmani, & Mekhilef, 2015). A hybrid ACO-P&O method is used to guarantee a rapid convergence speed regardless of a step size of the duty cycle (ΔD), which occasionally detects the LMPP instead of the GMPP on a P-V curve at PSCs (Sundareswaran et al., 2015). An ANN-P&O method is designed to detect an operating point location by measuring a PV current and classifying the output reference voltage at partially shaded I-V curve.

Table 2.2: Comparison between P&O-MPPT Methods

Parameters/ P&O MPPTs	Adaptive P&O[1]	FSCCP &O[2]	DA P&O[3]	PSO P&O[4]	FLC P&O[5]	ACO P&O[6]	ANN P&[7]	MB P&O[8]	GWO P&O[9]
Inputs	V_{pv}, I_{pv}	V_{pv}, I_{pv}	V_{pv}, I_{pv}	V_{pv}, I_{pv}	V_{pv}, I_{pv}	V_{pv}, I_{pv}	V_{pv}, I_{pv}	V_{pv}, I_{pv}	V_{pv}, I_{pv}
variables	I_{ref}	I_{ref}, D	D, ΔI	V_{ref}	D, Load	D	V_{ref}, D	V_{ref}	D
cost	Low	Low	Low	Low	Low	Low	Low	Low	Low
Controller	dSPE	dSPE	MC	MC	dSPE	PIC	DSP	PIC	dSPE
Converter	Boost	BB	SEPIC	Boost	Cuk	Boost	Buck	Boost	Boost
Complexity	Simple	Avg	Avg	Simple	Simple	Simple	Simple	Simple	Simple
Sys Ind.	Poor	High	High	High	Avg	High	High	High	High
Converge speed	Fast	Fast	Fast	Faster	Fast	Fast	Fast	Fast	Fast
MPP Oscillation	Less	Less	Less	Less	Less	No	less	Less	Less
Periodic Tuning	Yes	Yes	No	Yes	No	No	Yes	No	No
Power efficiency	Medium	High	High	High	High	High	High	High	High
Tracking speed	Faster	Fast	Fast	Fast	Fast	Faster	Fast	Faster	Faster

---

[1] Kollimalla, S. K., & Mishra, M. K. (2014). A novel adaptive P&O MPPT algorithm considering sudden changes in the irradiance. IEEE Transactions on Energy Conversion, 29(3), 602-610.

[2] Sher, H. A., Murtaza, A. F., Noman, A., Addoweesh, K. E., Al-Haddad, K., & Chiaberge, M. (2015). A new sensorless hybrid MPPT algorithm based on fractional short-circuit current measurement and P&O MPPT. IEEE Transactions on Sustainable Energy, 6(4), 1426-1434.

[3] Killi, M., & Samanta, S. (2015). Modified perturb and observe MPPT algorithm for drift avoidance in photovoltaic systems. IEEE Transactions on Industrial Electronics, 62(9), 5549-5559.

[4] Manickam, C., Raman, G. R., Raman, G. P., Ganesan, S. I., & Nagamani, C. (2016). A Hybrid Algorithm for Tracking of GMPP Based on P&O and PSO With Reduced Power Oscillation in String Inverters. IEEE Transactions on Industrial Electronics, 63(10), 6097-6106.

[5] Radjai, T., Gaubert, J. P., Rahmani, L., & Mekhilef, S. (2015). Experimental verification of P&O MPPT algorithm with direct control based on Fuzzy logic control using CUK converter. International Transactions on Electrical Energy Systems, 25(12), 3492-3508.

[6] Sundareswaran, K., Vigneshkumar, V., Sankar, P., Simon, S. P., Nayak, P. S. R., & Palani, S. (2015). Development of an improved P&O algorithm assisted through a colony of foraging ants for MPPT in PV system. IEEE Transactions on Industrial Informatics, 12(1), 187-200.

[7] Jiang, L. L., Nayanasiri, D., Maskell, D. L., & Vilathgamuwa, D. (2015). A hybrid maximum power point tracking for partially shaded photovoltaic systems in the tropics. Renewable Energy, 76, 53-65.

[8] Mahmoud, Y., Abdelwahed, M., & El Saadany, E. F. (2016). An Enhanced MPPT Method Combining Model-Based and Heuristic Techniques. IEEE Transactions on Sustainable Energy, 7(2), 576-585.

[9] Mohanty, S., Subudhi, B., & Ray, P. K. (2016). A Grey Wolf Assisted Perturb &Observe MPPT Algorithm for a Photovoltaic Power System. IEEE Transactions on Energy Conversion, 32(1), 340-347.

In the ANN-P&O, when solar irradiance is changed, a new GMPP area is predicted, and the tracking position of the operating point is measured as a voltage value by the ANN and P&O techniques, respectively. A P&O-MPPT algorithm is used to track the GMPP location in the tracking zone. The ANN algorithm created the tracking zone on the P-V curve (L. L. Jiang, Nayanasiri, Maskell, & Vilathgamuwa, 2015). A model-based (MB) and heuristic P&O algorithms are combined to enhance tracking performance in dynamic weather conditions, which needs very less computational time and complexity (Mahmoud et al., 2016). In a hybrid gray wolf optimization (GWO) and P&O method, an offline GWO algorithm drives an operating point nearest to the GMPP location by reducing the searching space. The online P&O method is then operated to track the best wolf position when wolves are closest to one another. In this combined method, only three animals are selected to scale down computational complexity, although a larger number of animals produce a more precise MPP tracking (Mohanty, Subudhi, & Ray, 2016). Table 2.2 describes all the parameters of the P&O algorithms. In Table 2.2, microcontroller (MC), dSPACE (dSPE), Avg (average), Sys Ind. (system independence) and buck-boost converter (BB) are written in short form.

2.5.3 INC MPPTs

This section presents a comprehensive review of INC MPPT algorithms with their merits, disadvantages, tracking performance, cost and implementation complexity. The digitally implemented INC algorithms are also reviewed to explain their performance under dynamic weather conditions. This section also includes fixed, variable and adaptive step sized INC MPPT algorithms. A comparison table is presented at the end of this section.

2.5.3.1 Fixed step size (FSS)-INC algorithm

This traditional FSS-INC algorithm is commonly known as a Hill Climbing (HC) MPPT scheme (Elgendy, Zahawi, & Atkinson, 2014). The algorithm is generally applied to track a unique MPP seeing on the P-V curve at uniform solar insolation. The INC method stands on a concept that its gradient or summation of an instantaneous and incremental conductance of P-V curve is zero at MPP, absolute to the leftward of MPP, and negative to the rightward of MPP, as shown in Eq. (2.4) (Elgendy et al., 2014; Hussein, Muta, Hoshino, & Osakada, 1995). The MPPT method is not worthy enough to use in partial shading cases on the PV characteristics waveforms since it doesn't altogether remove oscillations at SSC (J. G. Lee et al., 2012, October).

$$\left\{\frac{\mathrm{dP}}{\mathrm{dV}} = 0, \mathrm{at\ MPP}; \frac{\mathrm{dP}}{\mathrm{dV}} > 0, \mathrm{left\ of\ MPP};\ \frac{\mathrm{dP}}{\mathrm{dV}} < 0, \mathrm{right\ of\ MPP}\right\} \tag{2.4}$$

Eq. (2.5) mathematically manipulated as:

$$\left\{\frac{\mathrm{dP}}{\mathrm{dV}} = \frac{\mathrm{d(IV)}}{\mathrm{dV}} = \mathrm{I} + \mathrm{V}\frac{\mathrm{dI}}{\mathrm{dV}} = \mathrm{I} + \mathrm{V}\frac{\Delta \mathrm{I}}{\Delta \mathrm{V}}\right\} \tag{2.5}$$

Substituting equation (2.4) into (2.5), (2.6) it is computed as;

$$\left\{\frac{\Delta \mathrm{I}}{\Delta \mathrm{V}} = -\frac{\mathrm{I}}{\mathrm{V}}, \mathrm{at\ MPP};\ \frac{\Delta \mathrm{I}}{\Delta \mathrm{V}} > -\frac{\mathrm{I}}{\mathrm{V}}, \mathrm{left\ of\ MPP};\ \frac{\Delta \mathrm{I}}{\Delta \mathrm{V}} < -\frac{\mathrm{I}}{\mathrm{V}}, \mathrm{right\ of\ MPP}\right\} \tag{2.6}$$

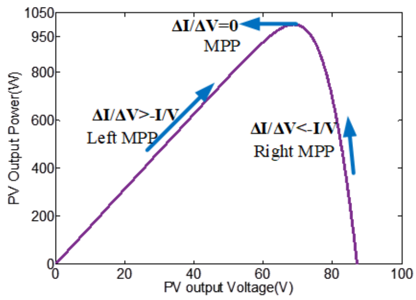

Figure 2. 9: MPP locations of INC algorithm (S. S. Mohammed & Devaraj, 2015)

Figure 2.9 depicts how an operating point traces a location of MPP by comparing an instantaneous conductance ($\Delta I/\Delta V$) with an incremental conductance (I/V). A reference variable is incremented or decremented, comparing the two conductance values to track a proceeding MPP location. An alternative control parameter (only duty cycle) instead of reference voltage can be used in the MPPT scheme to drive an operating point toward an expected MPP location (Elgendy et al., 2014; Hussein et al., 1995; P. Huynh & Cho, 1996; F. Liu, Duan, Liu, Liu, & Kang, 2008). A complexity in designing the circuitry and optimizing the control parameters' perturbation size is the main barrier to selecting the best MPPT algorithm (Kuo, Liang, & Chen, 2001). Therefore, a true MPP is tracked by analyzing the two conductance values at a moment if only a suitable algorithm is selected with an accurate perturb value of a control variable in uniform weather conditions. The initial input of an algorithm is a reference voltage (Vref) at which the FSS-INC is set to operate. Hence, to obtain maximum power, the control variable (Vref) is brought to an approximate initial PV array voltage.

2.5.3.2 Variable Step Size (VSS)-INC MPPT

A conventional fixed-step size (FSS) INC-MPPT cannot track the GMPP location on a P-V curve when a rapid change of solar irradiance and partial shading conditions (PSCs) occur on a PV array (J. G. Lee et al., 2012, October). However, the VSS-INC algorithm can shift the operating point toward GMPP location with an appropriate step change of the duty cycle under the PSCs. However, the VSS-INC is an inefficient method to apply under adverse weather condition because it leaves a more significant amount of power oscillations nearer to the GMPP location though its tracking performance is better than the FSS-INC algorithm (Carannante, Fraddanno, Pagano, & Piegari, 2009; F. Liu et al., 2008).

2.5.3.3 Adaptive INC MPPT algorithm

An adaptive step sized INC-MPPT algorithm attains a faster convergence speed at the steady-state condition. The operating point of adaptive INC-MPPT moves rapidly toward an MPP location because it requires fewer iterations of the duty cycle. This MPPT algorithm includes a constant (S) feedback variable and an exponential factor (M). When the constant (S) step size increases, the tracking speed of an operating point is increased, but convergence speed remains slow. If the M value is applied as a variable and the S is unchanged, the accuracy of tracking MPP location increases, but the tracking speed is reduced yet. Therefore, an optimal set of S and M values can increase the convergence speed, but it leaves the accuracy down shown in Figure 2.10. The adaptive INC algorithm can be used as an alternative approach to the conventional fixed step sized INC algorithm because of its fast convergence speed (Hossain, Tiwari, & Bhattacharya, 2016).

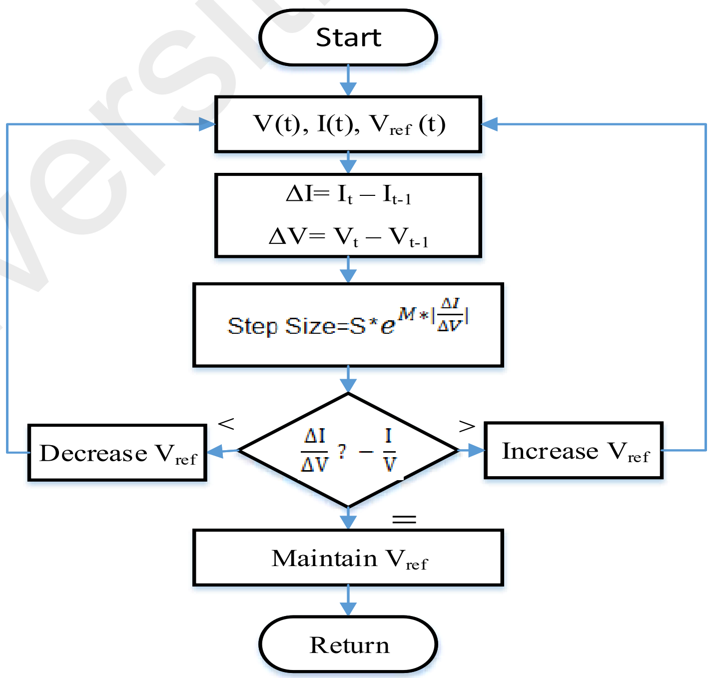

Figure 2. 10: A Flowchart of an Adaptive INC-MPPT Scheme (Jedari, Gharehpetian, Fathi, & Vahids, 2016)

2.5.3.4 Modified adaptive INC algorithm

Variable step size (VSS)-INC algorithm contributes massive power oscillation around the GMPP location. The VSS-INC algorithm increases tracking speed when a large amount of perturbation size of a duty cycle is selected and required MPP location is still seen far from an operating point in dynamic weather conditions (F. Liu et al., 2008). Therefore, the VSS-INC algorithm is developed to overcome a tradeoff between a high tracking speed and increased power oscillations in an adjacent region of the MPP on the P-V curve (J.-G. Lee et al., 2012).

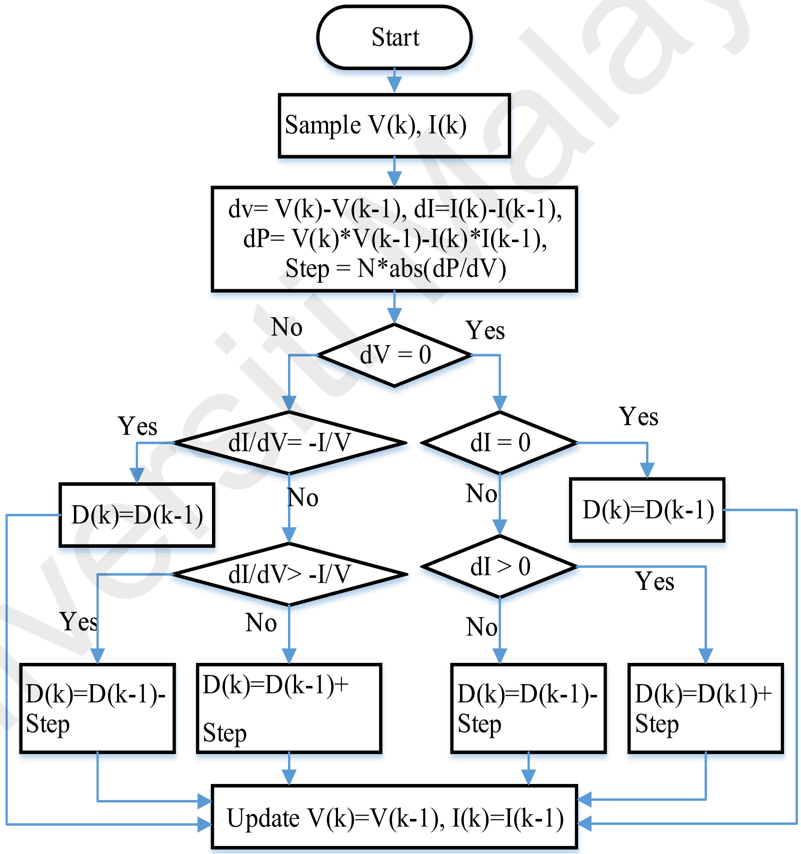

Figure 2. 11: An Adaptive INC MPPT (J.-G. Lee et al., 2012)

Figure 2.11 shows a graph of an improved adaptive INC-MPPT technique by which a new perturbation of the duty cycle is calculated using a step (N*abs(dP/dV). Eq. (2.7) is derived from controlling a duty cycle, and N as a multiplier is dedicated to regulating the perturbation size of a control variable. In some studies, the typical N value is chosen from 0.06 to 0.12. However, a considerable N value guarantees a drastic increase in tracking speed. In Eq. (2.8), the maximum step size of a duty cycle (ΔD_{max}) is selected initially for the fixed step INC algorithm. D (k) and D (k-1) are the present and past step sizes of the duty cycle, respectively. The slope of a P-V curve (dP/dV) is used to change the duty cycle's perturbation size.

$$D(k) = D(k-1) * N\left|\frac{dP}{dV}\right| \tag{2.7}$$

$$N < \Delta D_{max} / \left|\frac{dP}{dV}\right|_{\text{fixed step}=\Delta D_{max}} \tag{2.8}$$

The VSS-INC operates as a fixed step size INC algorithm If Eq. (2.8) is not used in MPP tracking (F. Liu et al., 2008). An operating point of the VSS-INC algorithm deviates from a GMPP location when a perturbation size of the duty cycle is wrongly selected, resulting in massive power losses.

2.5.3.5 Power increment INC-MPPT technique

The power increment INC-MPPT is developed to increase tracking speed because of confusing values of current change (ΔI) and zero slope on the I-V curve's left side. To attain maximum power from a PV array, the MPPT suppresses the number of duty cycle iterations.

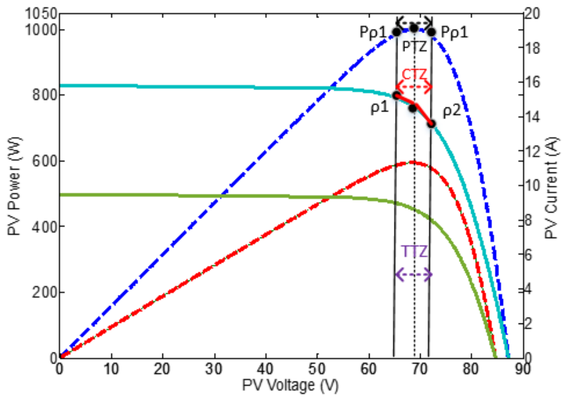

Figure 2. 12: Threshold Tracking Zones (Hsieh, Hsieh, Tsai, & Wang, 2012)

$$-\rho 1 \frac{\text{Ipv}}{\text{Vpv}} > \Delta\text{C} > -\rho 2 \frac{\text{Ipv}}{\text{Vpv}} \tag{2.9}$$

$$-\text{P}_{\rho 1} > \Delta\text{P} > -\text{P}_{\rho 2} \tag{2.10}$$

Conductance increment (ΔC) and power increment (ΔP) are bounded by the ratios ($\rho1$ and $\rho2$) on an I-V curve, and the rations ($\text{P}_{\rho 1}$ *and* $\text{P}_{\rho 2}$) on the P-V curve, respectively, shown in Eq. (2.9) and Eq. (2.10). The power increment INC-MPPT tracks a GMPP location by identifying the conductance threshold zone (CTZ) and power threshold zone (PTZ) on the I-V curve and P-V curve. An operating point's location is detected by the threshold tracking zone (TTZ) that equals the sum of the CTZ and PTZ. The ΔC and ΔP are measured inside and outside regions of the TTZ, respectively. A proper selection of the TTZ range enables an operating point to track the GMPP at the left-right side of a P-V Curve, as shown in Figure 2.12 (Hsieh et al., 2012).

2.5.3.6 Solar tracker (ST)-INC algorithm

Figure 2.13 shows an open and close-loops solar tracker (ST) MPPT algorithm used to tilt a PV array perpendicular to the sunlight to achieve maximum solar irradiance on the PV array (D. C. Huynh & Dunnigan, 2016).

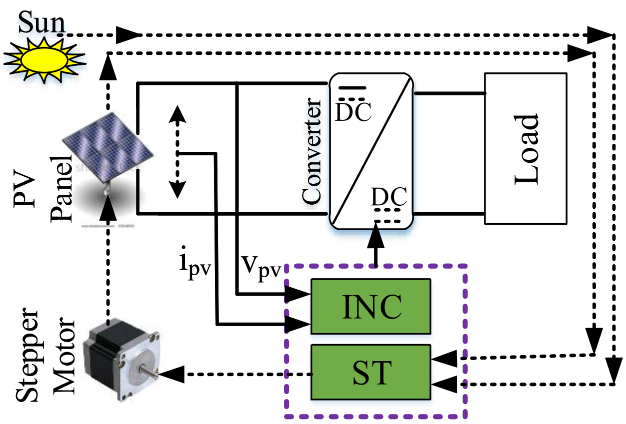

Figure 2. 13: A Diagram of ST-MPPT (D. C. Huynh & Dunnigan, 2016)

Figure 2.14 shows an improved INC algorithm is integrated with a constant voltage (CV) algorithm to guarantee a faster tracking of a GMPP location in the limited searching area of a P-V curve. A stepper motor is connected between a Sun tracker (ST) and a PV panel to rotate a PV module toward sunlight.

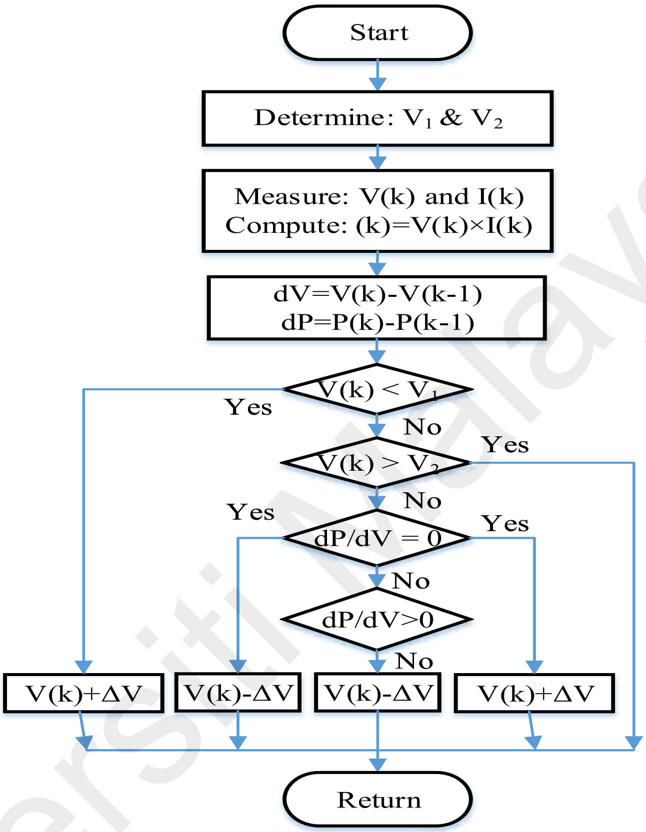

Figure 2. 14: Improved INC Algorithm (D. C. Huynh & Dunnigan, 2016)

In the ST-INC method, the CV algorithm first measures reference voltage, V(k), to identify a GMPP zone derived in Eq. (2.11). Then, the INC algorithm tracks the best GMPP point (0.76 V_{oc}) from three predicted regions; (0 to 0.7 V_{oc}), (0.7 V_{oc} to 0.8 V_{oc}), and (0.8 V_{oc} to V_{oc}). This combined MPPT technique has less computational complexity, high tracking and convergence speeds.

$$V(k) = (70\% - 80\%)V_{oc} = (V_1 - V_2) \tag{2.11}$$

The ST-INC MPPT algorithm can maximize a PV array's output power under the variations of temperature and solar insolation (D. C. Huynh & Dunnigan, 2016).

2.5.3.7 First converged INC-MPPT with FOCV and FSSC algorithms

A fractional open-circuit voltage (FOCV) and fractional short circuit current (FSSC) algorithms are integrated with an improved INC-MPPT scheme to operate PV systems without an intermittent disconnection. However, a periodic tuning of a duty cycle is required to operate a PV array when an operating point locates closer to a GMPP location. A permitted error between an incremental conductance and instantaneous conductance is assumed to be approximately 0.06 to operate the PV array at high tracking speed, as demonstrated in Eq. (2.12) (Soon & Mekhilef, 2014).

$$\left|\frac{\mathrm{dI}}{\mathrm{dV}} + \frac{\mathrm{I}}{\mathrm{V}}\right| < 0.06 \tag{2.12}$$

2.5.3.8 FLC based INC-MPPT scheme

A fuzzy logic controller (FLC) based INC-MPPT algorithm is deployed to maintain an operating point of a control variable nearest to the GMPP location in highly dynamic weather conditions. The FLC-INC-MPPT is an alternative of a conventional fixed step sized INC-MPPT technique to track GMPP at PSCs (Radianto, Dousouky, & Shoyama, 2015, October; Radjai, Rahmani, Mekhilef, & Gaubert, 2014). The FLC algorithm operated through three rules such as fuzzification (input as e & Δe), rule interference (for controlling output variable), and defuzzification (output used as a duty cycle). The FLC's operation depends on the designer's assumption on the range of membership functions used to convert the linguistic values into the crisp and numerical (Radjai et al., 2014; Seyedmahmoudian et al., 2016). In the FLC-INC method, a conventional P&O algorithm is used to receive its input value (duty cycle) measured by the FLC algorithm.

The FLC algorithm follows the fuzzification, interference, and defuzzification rules to help the INC algorithm recovering its tracking deviation of an operating point, as shown in Figure 2.15 and Figure 2.16. The FLC controller rules are shown in Table 2.3.

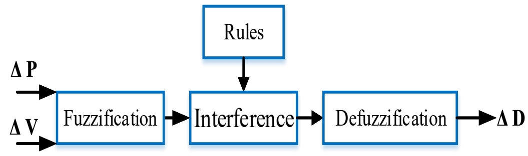

Figure 2. 15: The Stages of the FLC (Abdourraziq & El Bachtiri, 2014)

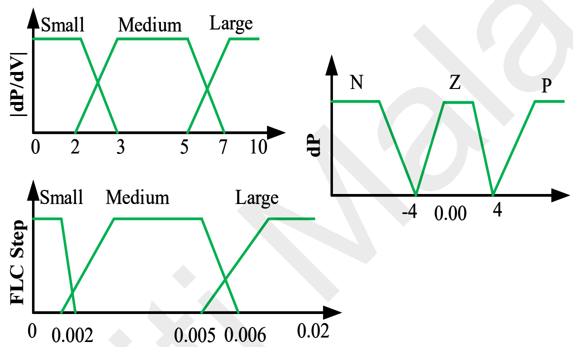

Figure 2. 16: FLC Membership Functions and Subsets (Radjai et al., 2015)

Table 2.3: Fuzzy Logic Controller Rules (Radjai et al., 2015)

FLC input $\lvert\Delta P/\Delta V\rvert$	ΔP	FLC Output
Large	N	Small
large	P	Large
Small	N	Small
Small	P	Small
Small	Z	Small
Medium	P	Medium
Medium	N	Small

The primary and secondary inputs of the FLC algorithm are an absolute value of P-V curve $\lvert\Delta P/\Delta V\rvert$ and power slope (ΔP). Input and output of the FLC have three language variables: negative (N), positive (P), and zero (Z); The modified INC algorithm makes an error value (e_{INC}) approximately zero by comparing an instantaneous and incremental conductance as shown in Eq. (2.13). Then a fuzzy logic controller determines its first input as a minimized error (e_{INC}) by measuring the step size of a duty cycle of a CUK converter, as shown in Figure 2.17.

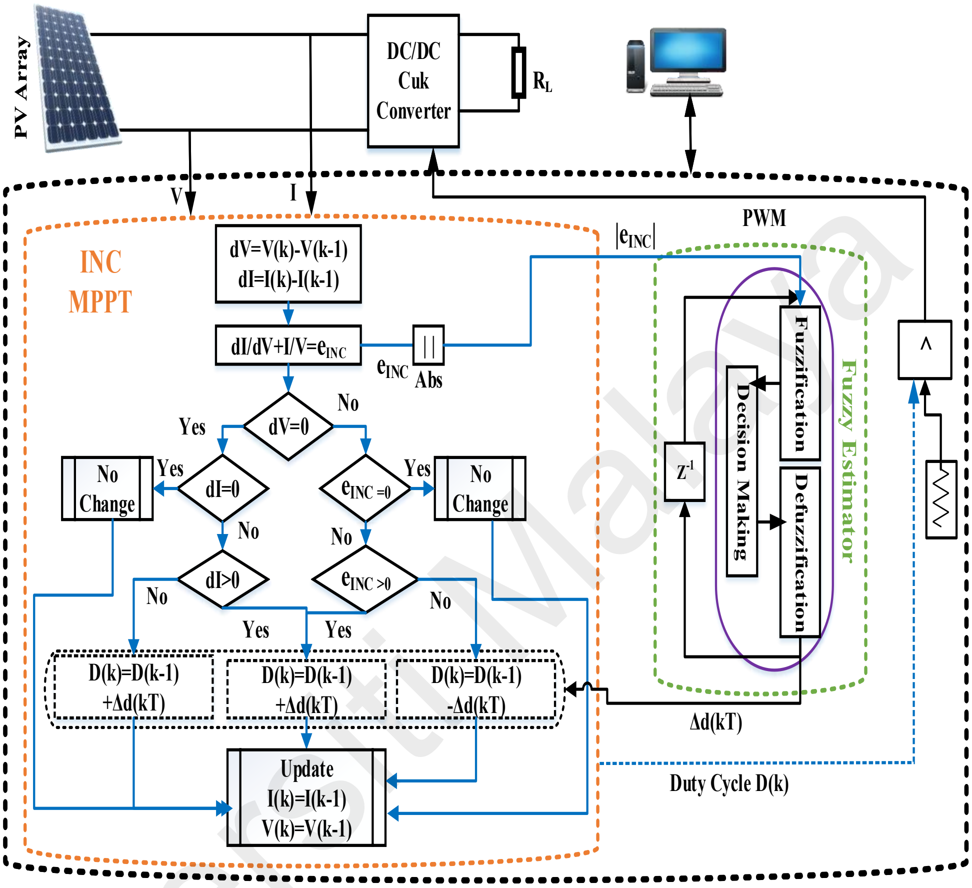

Figure 2. 17: Direct Control INC with FLC (Radjai et al., 2014)

$$\frac{dI}{dV} + \frac{I}{V} = |e_{INC}| \tag{2.13}$$

The second input of the FLC algorithm is calculated from the last change of the duty cycle. Output Dd (kT) of the FLC algorithm sends through the INC-MPPT to estimate an optimal value of a duty cycle for a DC conversion step (Radjai et al., 2014). This hybrid system ensures high accuracy in tracking the GMPP with less computational complexity (Radjai et al., 2015). Table 2.4 depicts a comparative table of the variables of different hybrid INC-MPPT techniques explained in this chapter.

Table 2.4: Comparison of INC Algorithms

Parameters/INC MPPTs	Adaptive INC	ST- INC[10]	FC-NC[11]	PI- INC[12]	FLC- NC[13]
Input variables	V_{pv}, I_{pv}	V_{pv}, I_{pv}	V_{pv}, I_{pv}	V_{pv}, I_{pv}	V_{pv}, I_{pv}
Control variables	D	V_{ref}	R_{load}, D	D	R_{load}, D
Implementation cost	Low	Low	Low	Low	Low
Controller types	PIC	Microprocessor	PIC	DSP	dSPACE
Converter types	Boost	Buck-Boost	SEPIC	Fly Back	CUK
Complexity	Simple	Complex	Simple	Complex	Average
System independence	High	High	High	High	High
Reliability in PSCs	Less	High	High	High	High
Convergence speed	Average	Fast	Fast	Medium	Fast
Oscillation at MPP	No	No	No	No	Less
Periodic tuning	Yes	Yes	Yes	Yes	Yes
Power efficiency	Average	High	High	High	High
Tracking speed	Slow	Fast	Fast	Fast	Faster

2.5.4 DC-DC Converters

MPPT schemes maximize a PV system's power by controlling a duty cycle and switching a DC-DC converter (analyzing its current or voltage). DC-DC converters are mainly used to stabilize the PV system's output voltage in any weather conditions (Charaabi, Barambones, Zaidi, & Zanzouri, 2020). When a converter with a fixed duty cycle experiences the PSCs or load changes, the output voltage and current of a PV system are destabilized. An MPPT controller regulates the converter's duty cycle if only the PSCs and load variations are detected on a PV array (Soon & Mekhilef, 2014). The DC-DC converter and MPPT controller are operated in a continuous mode to ensure an uninterruptable power supply to the load. However, the converter's continuous mode operation creates some effects such as electrical resonance, device heaviness, expenses,

---

[10] Huynh, D. C., & Dunnigan, M. W. (2016). Development and comparison of an improved incremental conductance algorithm for tracking the MPP of a solar PV panel. IEEE Transactions on Sustainable Energy, 7(4), 1421-1429.

[11] Soon, T. K., & Mekhilef, S. (2014). A fast-converging MPPT technique for photovoltaic system under fast-varying solar irradiation and load resistance. Industrial Informatics, IEEE Transactions on, 11(1), 176-186.

[12] Hsieh, G. C., Hsieh, H. I., Tsai, C. Y., & Wang, C. H. (2012). Photovoltaic power-increment-aided incremental-conductance MPPT with two-phased tracking. IEEE Transactions on power electronics, 28(6), 2895-2911.

[13] Azman, A. Y., Rahman, A. A., Bakar, N. A., Hanaffi, F., & Khamis, A. (2011, June, 27-29 June 2011). Study of renewable energy potential in Malaysia. Paper presented at the 2011 IEEE Conference on Clean Energy and Technology (CET). IEEE.

and unreliable power supply to the load. A filter circuit or sizeable electrolytic capacitor (with 1000 h lifetime) is connected at the converter's output side to store surplus energy and reduce the converter's ripples of primary current and secondary voltage. A uniform PV array's efficiency is dropped by 5% if a ripple voltage of MPP is found at approximately 8% (El Khateb, Rahim, Selvaraj, & Williams, 2014).

The popular converters, namely, single-ended primary inductor converter (SEPIC), Cuk, boost, and buck-boost, are used to increase or decrease the PV array's input voltage. The buck and buck-boost and SEPIC converters allow a flow of discontinuous input current and output current, respectively (El Khateb et al., 2014; Kok Soon Tey, 2018). The buck-boost converter is not widely used in MPPT applications because of its discontinuous input current flow and inadequate transient response to weather changes. However, the buck-boost converter reduces its circuit components' size if it is operated with a high switching frequency (Sarikhani, Allahverdinejad, & Hamzeh, 2020). A continuous conduction mode (CCM) boost converter reduces the ripple components and boosts up PV current and voltage by regulating a duty cycle's perturbation size. A carrier signal is compared with the duty cycle to generate pulse width modulation (PWM), and switching OFF and ON of a MOSFET or IGBT (Mirzaee, Arab Ansari, & Shokrollahi Moghani, 2020). Voltage drop and current across an inductor of the converter are measured when its switch (IGBT) is closed for a time ($\mathrm{DT_s}$) and opened for a time ($(1-\mathrm{D})\mathrm{T_s}$) respectively. $\mathrm{T_s}$ stands for the total period required to operate the IGBT in both ON and OFF states. Eq. (2.14) shows a relation between a duty cycle, input and output voltages of the boost converter (Z. Jiang, Chen, Zhang, Qiu, & Xie, 2020).

$$\mathrm{V_0} = \frac{\mathrm{V_i}}{(1-\mathrm{D})} \tag{2.14}$$

PV current flows across an inductor of a CCM converter until a steady-state condition of switching IGBT is over. Figure 2.18 shows a simple circuit of the converter.

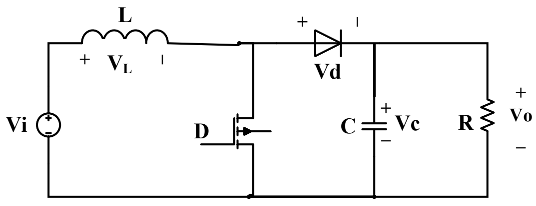

Figure 2. 18: DC-DC Boost Converter (R. Zhang, Wu, Zhang, Wang, & Cang, 2018)

2.5.5 Control of MPPTs and Boost Converter

Two proportional-integral (PI) controllers are integrated with an MPPT algorithm to maintain a PV array's maximum output power at any weather condition (Soon & Mekhilef, 2014).

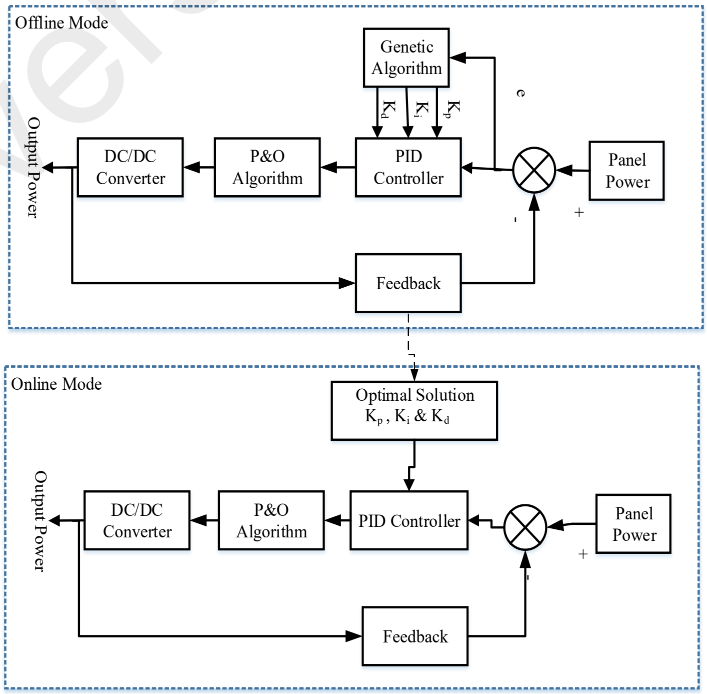

Figure 2. 19: Offline and Online Controller (Harrag & Messalti, 2015)

Figure 2.19 demonstrates a P&O MPPT controller integrated with two PI controls to maximize a PV module (Sahoo et al., 2020). Implementing an MPPT algorithm with the PI controllers in both simulation and experimental works is affected by the user talent and knowledge. For example, a real-time dSPACE board is used to implement an MPPT controller to generate PWM signals and digitize DC/DC and DC/AC converters (Farhat, Barambones, & Sbita, 2015).

2.5.6 Photovoltaic Inverters

A single-phase voltage sourced inverter (VSI) is used to feed a boosted DC-link voltage of the DC/DC converter to generate square signals of the output current and voltage. The VSI is classified as a full and half-bridge inverter based on the voltage and current control strategy. A selection of a suitable VSI relies on the weather conditions and user affordability (N. Singh & Khan, 2020). There are two types of common inverter topologies are explained as follows;

2.5.6.1 Single-stage centralized inverter (SSCI)

The SSCI inverter is usually connected with a real PV sting that formed by two parallel-connected photovoltaic arrays. Figure 2.20 shows a schematic diagram of the SSCI inverter.

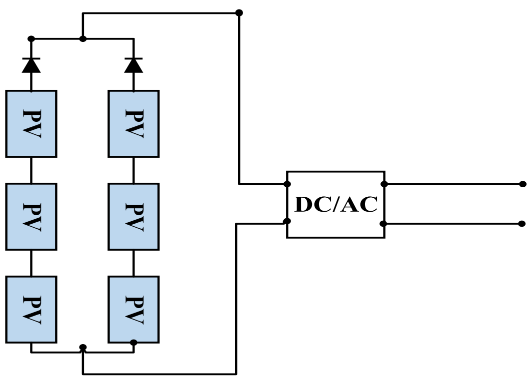

Figure 2. 20: Single-Stage Centralized Inverter (Kabalcı, 2020)

The SSCI inverter's drawbacks are a power mismatch and unequal voltage distribution between parallel-connected PV panels under PSCs (Kabalcı, 2020).

2.5.6.2 Single-stage string inverter (SSSI)

Figure 2.21 depicts a diagram of the SSCI that is suitable to use along with a distributed MPPT technique to track a maximum power point (MPP) separately from each PV module under PSCs. The SSSI performance is better than that of the SSCI because it allows an MPPT algorithm to track a GMPP of the P-V curve from each PV array at an adverse weather condition (Zakzouk, Abdelsalam, Helal, & Williams, 2020).

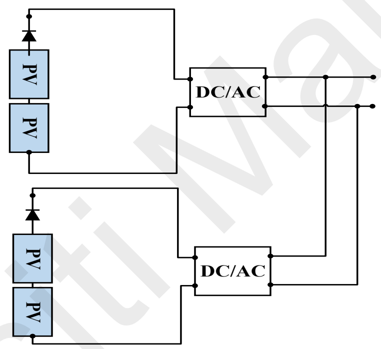

Figure 2. 21: Single-stage string inverter (Ovaska, 2010)

2.5.7 Grid Integrated PV System

Figure 2.22 shows a typical grid-connected PV system used to harness solar energy into electrical energy from a PV array and deliver surplus energy to a utility grid (Jiandong, Ma, & Tuo, 2018, September). A grid-tied PV system allows a bi-directional power flow between a country's national grid and the PV plant, which benefits the plant owner to earn revenue by selling units (KWh) (Jasuan, Nawawi, & Samaulah, 2018. October). Several issues, such as safety and synchronization between a PV array and the grid, need to be assessed before maximizing energy production from a grid-connected PV system. Technical problems such as islanding, unbalanced condition, hazarded noise, and out of phase of frequency and voltage between the VSI and grid are explained in detail to come up with the best synchronization technique of the grid-tied PV system (Peña, Sampaio, de Brito, & Canesin, 2020).

A power range of a grid-connected system is started worldwide from a few kilowatts (kW_p) to several megawatts (MW_p) from domestic PV plants and a utility-scale PV plant (Bouzerdoum & Mellit, 2017, October). Manufacturer companies of the grid-tied PV system need to follow high design standards because of integrating robust and sophisticated control techniques in practical aspects (Eltawil, Zhao, & Reviews, 2010). A PV system's performance is deteriorated because of two types of losses: power conversion loss and tracking loss of a PV array (Bouzerdoum & Mellit, 2017, October).

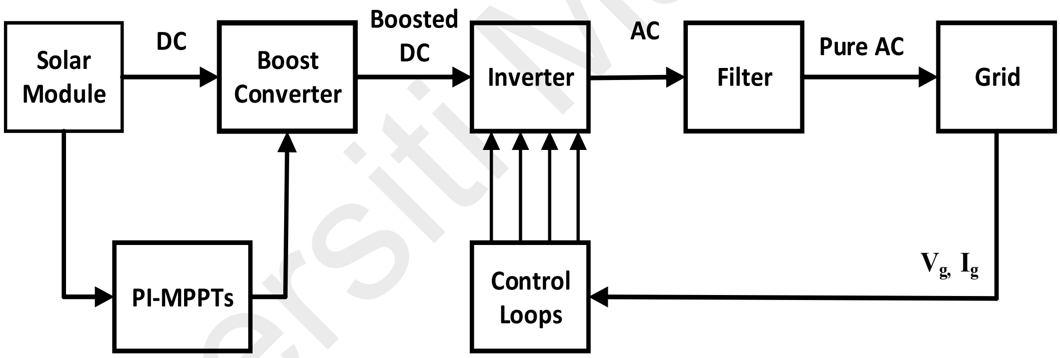

Figure 2. 22: Typical Diagram of Utility Grid (Suman, Yadav, & Jangid, 2018)

2.5.8 Control Techniques of the Grid-Connected PV System

Several controllers, such as a sine pulse width modulation (SPWM), proportional-integral (PI), proportional resonance (PR), and phase-locked loop (PLL), is required to regulate the voltage and power of the grid-connected PV system. These controllers are integrated with a grid-tied PV system to maximize power generation and a reliable operation of the utility grid and a PV plant. In grid-side control, the PLL and PR are used to synchronize voltage and frequency between the grid and the VSI and minimize the steady-state error of grid current, respectively (Youssef, El-Telbany, & Zekry, 2018).

2.5.8.1 SPWM techniques

Pulse width modulation (PWM) decreases an average power of a DC/DC converter by sampling it into digital pulses. The discrete signal's amplitude is equally proportional to the control parameter's value, such as voltage. A DC/DC converter and DC/AC inverter are operated at a high switching frequency (kHz) to reduce their components. Advanced PWM techniques are developed to increases the power quality of a PV system. The SPWM technique converts the sinusoidal signal into discrete form to reduce the harmonic components of current and voltage of the VSI. In the SPWM technique, a triangular waveform is modulated with a sinusoidal signal to generate two complementary pulses to operate the switches of the VSI. (Sharif, 2018). The SPWM technique generates the same amplitude of the complementary pulses as a percentage of duty cycle value (Aroul, Umashankar, Prabhu, & Sanjeevikumar, 2018). The SPWM technique is classified into bipolar and unipolar techniques (IsaTezde, MuhsinDemir, Gurel, IbrahimOkumus, & Kahveci, 2018).

THE unipolar SPWM technique can generate two times higher switching frequencies than the bipolar technique. However, the same type of a carrier signal is modulated with a sinusoidal waveform in both techniques (Baburajan, Peyghami, Kumar, Blaabjerg, & Davari, 2020). A low leakage current is generated across the switches of the VSI when bipolar SPWM pulses are applied instead of unipolar SPWM pulses (Yuditya, Hasanah, Ardhenta, & Taufik, 2020). However, the bipolar SPWM technique requires a double carrier signal out of phase from each other compared to the unipolar method (Prabaharan, Arun, Palanisamy, & Sanjeevikumar, 2018).

2.5.8.2 Proportional Resonance (PR) and PI controllers

A grid current of a grid-connected PV system is controlled by simple Proportional Integral (PI) controllers (Asok, Baburaj, Jayaprakash, & Mukundan, 2018, March). An advantage of using the PR controller is to eliminate steady-state error (SSE) from the grid current and voltage waveforms by producing infinite gain in previously identified resonant frequency and highly attenuated gain at other frequencies (Yuan, Allmeling, Merk, & Stemmler, 2000, October), (Youssef et al., 2018). A proportional resonance (PR) controller is used to remove the SSE from grid current and voltage and select line frequency as closed as resonance frequency (S. Islam et al., 2018). The PR controller increases the performance of the grid-connected PV system. Signals that the PR controller controls are sent to a PWM generator to produce complementary SPWM pulses (Oruganti, Dash, Nallaperumal, & Ramasamy, 2018).

2.5.9 DC-link capacitor

Current and voltage waveforms of the VSI, and DC-link voltage (V_{Cdc}) generate harmonic and ripple components. The ripples and harmonics are developed because of an improper selection of the DC-link capacitor and filter circuit (Panigrahi, Mishra, & Srivastava, 2018, September). A bulk DC-link capacitor functions as a filter to supply a constant ripple-less voltage into the VSI by filtering out a high frequency switching current (Rettner, Schiedermeier, Apelsmeier, & März, 2020). In a PV system, an electrolytic DC-link capacitor is inefficient because of its low voltage capacity, ripple current, and less longevity, regardless of its availability and convenient cost found in the market. In contrast, a reliable Dc-link film-type capacitor can remove a ripple component of a double-line frequency of the VSI current (Rettner et al., 2020). A large capacity DC-link capacitor also removes a pulsating DC component of a DC/DC converter (Panigrahi et al., 2018, September).

2.5.10 Grid synchronization Technique

An automated synchronization control technique synchronizes the phase and frequency of the voltage and current between the VSI and utility grid. An inefficient simple controller of the synchronization technique causes non-linear effects and distortions in the grid current (Fantino, Busada, & Solsona, 2020). There are robust control methods used in grid synchronization to identify the variant phase quickly and frequency of the grid voltage and current and maintain the state of Grid affairs (Panigrahi et al., 2018, September). The synchronization controllers such as artificial neural network (ANN) algorithm, phase-locked loop (PLL), and linear quadratic estimation (LQE) are used to minimize harmonic components, obtaining balanced condition, and limiting ripple components of the grid voltage and current. The PLL is widely used to extract original current and voltage waveforms of the VSI and grid from distorted ones, and maintaining the same phase and frequency of the waveforms. However, the PLL cannot measure the magnitude and amplitude of the grid waveforms (Panigrahi et al., 2018, September). The PLL consists of a stochastic oscillator, a phase detector, and control loops dedicated to drawing a phase and frequency matching between the VSI and grid (Suman et al., 2018). Synchronous reference frame PLL (SRF-PLL) is mainly used in a three-phase PV system as a current synchronization controller, in which a 90° out of phase reference current is used to provide signals in d-q form. A proportional resonance (PR) controller (with no intermittent operation) is combined with the SRF-PLL technique to remove a steady-state error of the grid current (Pugliese, Kwon, & Liserre, 2020). However, the SRF-PLL is not used directly in single-phase grid-tied PV systems without increasing a number of control loops such as an orthogonal signal generator (OSG) used to synthesize a grid voltage and frequency, as shown in Figure 2.23. Many stages of filter circuits are required in the OSG design to activate the SRF-PLL detecting phase angle of the grid voltage when frequency and phase variations are noticed on the grid because of a load change and other disturbances (Stojić, Georgijević, Rivera, & Milić, 2017). A SOGI-PLL is very popular nowadays because of its stable operation and convenient design, which precisely can extract an accurate grid frequency from already noisy waveforms. An all-pass filter is required in the SOGI-PLL design to generate a delayed form of the grid voltage, but it causes severe distortions in the input waveforms of the VSI (Eltarouty, Aboudan, Biricik, Ahmed, & Benbouzid, 2020). The SOGI effectively filters out the VSI frequency's noisy components and removes ripple components from an orthogonal signal before sending them into a αβ - dq frame (Kalavalli, Meenalochini, Selvaprasanth, & Haq, 2020).

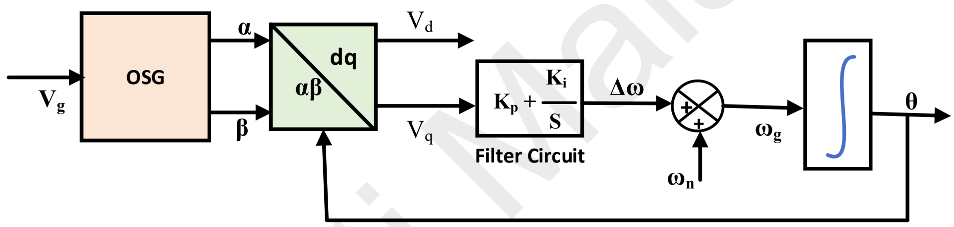

Figure 2. 23: Single-phase SRF-PLL (Stojić et al., 2017)

The SRF-PLL with OSG is divided into three categories: a time delay controller, a second-order generalized integrator (SOGI,) and a proportional derivative controller.

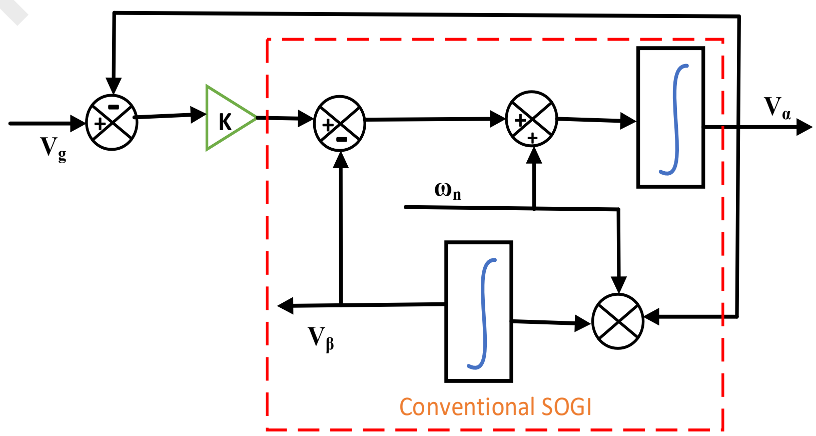

Figure 2. 24: SOGI based OSG-PLL (Cha, Vu, & Kim, 2009)

Figure 2.24 shows an improved SOGI signal generator in which a red-colored rectangular region is considered a conventional SOGI circuit. In modern grid synchronization control, a time delay in the PLL is not used because of unpredictable frequency changes in the grid voltage and current waveforms. Therefore, the SOGI-PLL includes a feedback control loop to limit unpredictable changes in the grid frequency.

2.6 Summary

A GMPP changes its location along the P-V curve because of a sudden weather change, which increases the computational burden for an MPPT algorithm, and the harmonic components of voltage and current waveforms of the VSI. The power oscillations are increased when an operating point of an MPPT algorithm continuously moves around the GMPP at steady-state conditions. Some studies use a variable perturbation size of a duty cycle in a sophisticated MPPT technique to meet a massive power oscillation around a GMPP region. An FLC algorithm takes a long time to track and store the GMPP and LMPPs because of its complex fuzzification and defuzzification rules. A PSO algorithm needs much converging time toward the GMPP location because of making many assumptions to the membership functions of a governing equation.

In essence, conventional open-loop MPPT algorithms cannot track the GMPP location, leaving massive power oscillations when any partial shading condition (PSC) occurs on the P-V curve. On the other hand, conventional closed-loop MPPT algorithms can track the GMPP location on a P-V curve when operated under uniform weather and shading conditions 1 and 2. Similarly, improved, online, offline, modified, and adaptive conventional MPPT algorithms are failed to track a GMPP location under shading conditions 2 and 3. A dynamic duty cycle perturbation is used to shift the operating point of the conventional MPPT algorithms to track the P-V curve's GMPP location.

However, the operating point of the MPPTs stops at an LMPP location instead of tracking the GMPP on the P-V curve because they are dependent on the concept of hill climbing. To shift the operating point of the conventional MPPTs toward GMPP location and increase its tracking speed, the duty cycle's perturbation size is increased, resulting in substantial power oscillations around the GMPP. Hence, A PI-based coordinated INC-MPPT algorithm is designed in chapter 3 to track the GMPP location on a P-V curve with high efficiency, high tracking speed, and zero power oscillations around the GMPP location at the PSCs.

Different types of continuous and discontinuous DC-DC converters are reviewed in this chapter to find out a simple and low-cost converter to design for the grid-tied PV system. A DC-DC continuous mode converter must be able to step-up the input voltage from the PV array to a level of the VSI input DC voltage at the PSCs. However, some conventional converters such as buck and buck-boost converter are not suitable for the grid-connected PV system. For example, a buck converter cannot increase output voltage when PV power is reduced at the PSCs. As a result, the VSI cannot receive the desired reference DC-link voltage to generate corresponding sinusoidal voltage to the grid voltage level. Therefore, the buck converter is only applied between a high power PV array and low power loads. The grid-tied PV system needs higher output voltage than PV panel; hence, a low-cost and straightforward boost converter is a better choice, but the buck and other step-down converters are used in low voltage PV applications. The PI controllers are integrated with the MPPT algorithm to maintain the boosted output voltage of the converter to the desired level of reference DC-link Voltage. The output reference voltage of the boost converter is boosted by increasing the duty cycle's perturbation size when PV power decreases because of the PSCs.

Load variations in the grid and signal conversion errors cause harmonic components, frequency instability, and out of phase on the current and voltage waveforms between the VSI and grid. Several control techniques for grid synchronization are discussed in this chapter to determine an exclusive control strategy for the grid-connected PV system. A simple, reliable, and robust synchronous reference frame phase-locked loop (SRF-PLL) in the VSI control is used to maintain the same phase and frequency of voltage and current between the VSI and grid sides.

CHAPTER 3: PROPOSED SYSTEM DESIGN

3.1 Introduction

This chapter presents a typology used to interface between a 250 V AC single-phase grid and a PV array. In section 3.3, eight types of shading patterns of PV arrays for both simulation and experimental works are drawn under uniform weather conditions and the PSCs. In section 3.4, the conventional INC flowcharts, P&O, and proposed MPPT techniques are sketched with their detailed functionality. In section 3.5, a DC-DC boost converter is employed to step up the output voltage of a grid-tied PV array and delivers power into the VSI. A switch-mode boost converter is designed because of its simple circuitry, a smooth and faster-switching ability, and supplying maximum power to the grid in this research work, limiting its output current to overcome an overheating of circuit elements. In section 3.6, the grid-tied FB-VSI is modeled with its principle and different configurations. The purpose of using an LCL type low pass filter (LPF) along with the VSI is to eliminate excessive harmonic and ripple components from the current and voltage waveforms and reducing the output current of the VSI.

Mathematical modeling and the transfer function of the DC-DC boost converter is developed to estimate its circuit components, such as inductor and capacitor. There are two distinct types of photovoltaic arrays with different power capacities, such as 1.5 KW and 213.55 W, to evaluate MPPT algorithms in simulation and experimental works, respectively. The converter switch is operated with high frequency (10 kHz) to minimize circuit elements' size and faster switching operation without overheating problem. This chapter includes mathematical modeling, working functions, and developing equations of the proposed controllers such as PI, PR, and SPWM technique. It also explains AC current regulator, a direct-quadrature (d-q) theory for 1-φ grid-connected PV arrays and the design of the PLL synchronization method. The proposed algorithm and two conventional MPPT methods are then designed with its working principles, stability analysis, flowchart, and partial shading conditions. The proposed algorithm is commercially attractive because of its simple structure, robustness, and reliability. Finally, PI controllers and the proposed PI-MPPT algorithm are designed to attain constant voltage at the output of DC-DC boost converter for an effective operation of the inverter. The bipolar SPWM method is applied to control inverter switches and limiting harmonic components of the unfiltered current and voltage at the inverter's secondary side.

3.2 Proposed Complete Topology

Figure 3.1 shows a designed topology for a grid-tied PV array. The topology consists of five interconnected branches such a PV array, an MPPT controller in connection with PI controllers, a PR controller, a DC-DC boost converter, a single-phase full-bridge (FB) VSI, and the LPF circuit along with grid load.

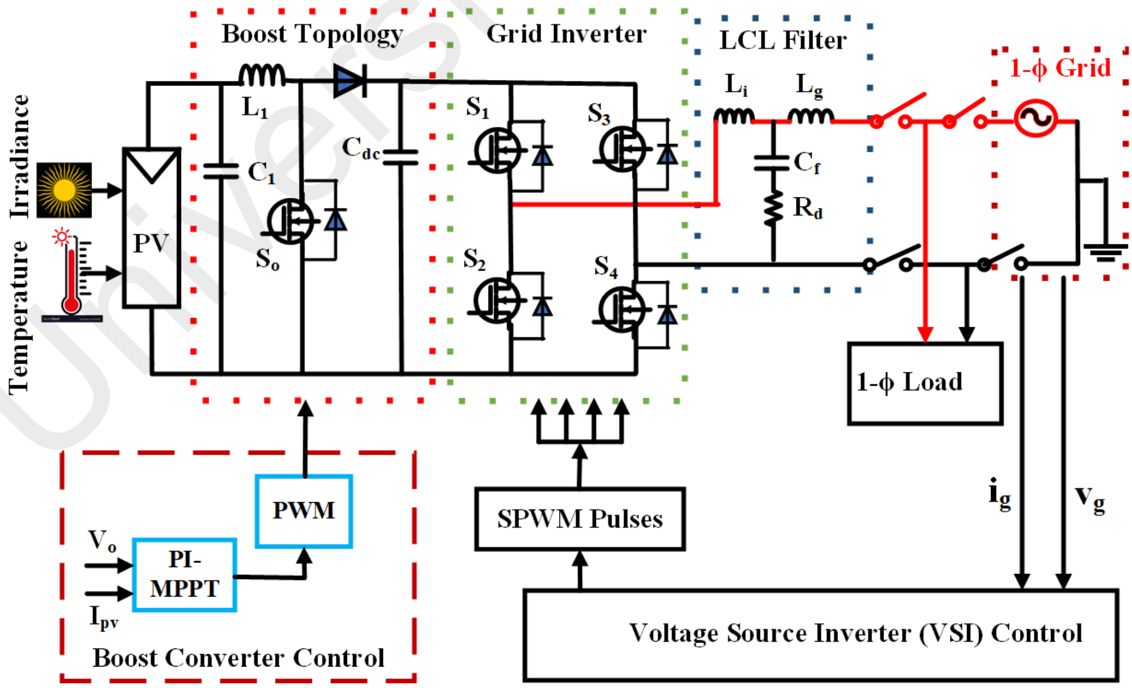

Figure 3. 1: Proposed Grid-Tied Topology

A DC-DC boost converter and a single-phase DC-AC inverter are used to step up PV voltage, and convert DC to AC voltage and current, respectively. The LCL-filter is used to decouple between the filter and the grid impedance. A parallel capacitor of the LCL filter limits a ripple current of the grid-side inductor (L_g). The LCL filter provides a good attenuation ratio even with small L and C values. MPPT controller, and voltage and current PI controllers are combined with tracking GMPP and generating constant DC-link voltage at the output-side of the boost converter. Single-phase digital phase-locked loop (PLL) is introduced to detect the phase of grid voltage. The grid voltage becomes α-component of the stationary reference frame, while the β-component is a virtual voltage through the filter. The stationary reference frame (α-β components) is converted into the synchronous reference frame (d-q components), in which d denotes a phase difference between grid voltage and measured VSI voltage. A conventional PR controller is used instead of a PI controller to achieve zero steady-state error (SSE) of a grid current. Compared with the conventional PI controller, the PR control can overcome two drawbacks of the PI controller: an inability to track a sinusoidal reference with zero steady-state error and a low capability of disturbance rejection.

3.3 PV array design under Partial Shading Conditions

Two types of PV models, such as an Isoltech 1STH-250-WH and Atlantis Energy System SS125LM, are applied in simulation and experimental analyses, respectively. Figure 3.2 shows two patterns for uniform weather conditions, and the six shading patterns at PSCs are drawn to generate corresponding P-V and I-V curves. Figure 3.2 (a–d) and Figure 3.2 (e-f) show uniform weather and the PSC patterns for the simulation and experimental works. In each PV pattern, a blocking-diode denoted in red color is used to limit the flow of a reverse saturation current across a PV array and protect the battery from damage. These eight different irradiance profiles are used to test the tracking performance of an MPPT algorithm. A maximum power (213.6 W) of a PV model is used in the experimental analysis for approximately seven times lesser than the maximum power (1497 W) of the simulation work because of the limited power rating of an Agilent solar simulator.

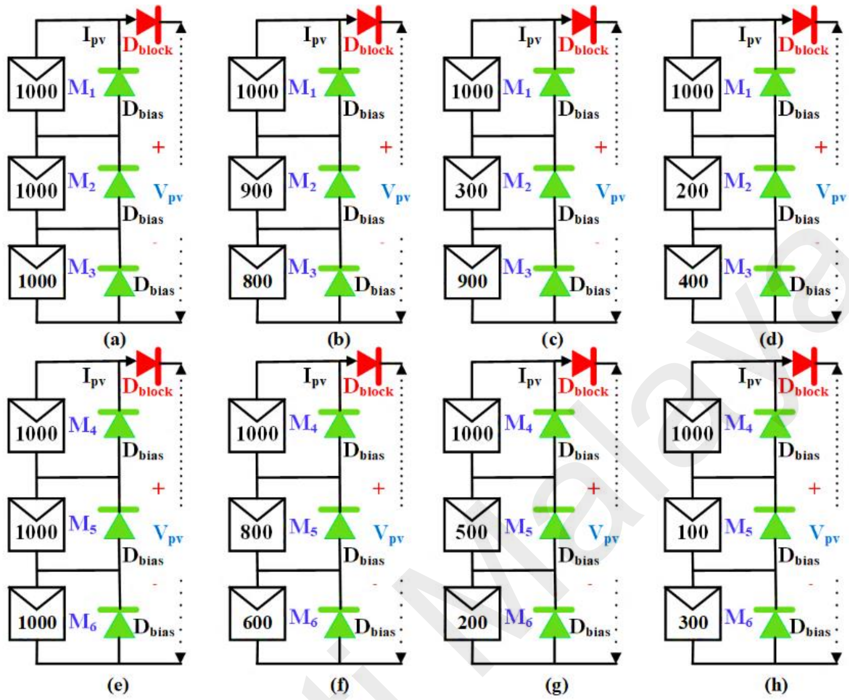

Figure 3. 2: Patterns for uniform and partial shading conditions are listed as (a–d) Shading patterns for PV array of Isoltech 1STH-250-WH; (e–h) Shading patterns for Atlantis Energy System SS125LM.

Table 3.1: Design Parameters of the PV Module

Models/ Parameters	Simulation Model (Isoltech 1STH-250-WH)				Experimental Model (Atlantis Energy System SS125LM)			
	MPP	$GMPP_r$	$GMPP_m$	$GMPP_l$	MPP	$GMPP_r$	$GMPP_m$	$GMPP_l$
N_{ss}	60	60	60	60	6	6	6	6
N_{ser}	1	1	1	1	1	1	1	1
V_{oc}	223.7	222.8	219.7	215.9	55.5	54.96	53.85	52.99
V_{mp}	183.9	189.6	123.7	59.98	43.5	47.03	30.71	13.18
N_{par}	6	3*2=6	3*2=6	3*2=6	15	3*5=15	3*5=15	15
I_{sc}	8.71	8.71	8.71	8.71	5.22	5.22	5.22	5.22
I_{mp}	8.14	6.72	7.47	8.13	4.91	3.05	2.53	4.88
P_{mp}	1497	1275	924.4	487.6	213.59	143.6	77.72	64.31

Table 3.1 shows the power, voltage, and current of LMPPs and GMPPs of the eight PV patterns measured from the MATLAB simulation environment. $GMPP_r$, $GMPP_m$,

and $GMPP_l$ are represented as the right, middle, and left GMPP locations, respectively, from the different shading patterns. The maximum power is uneven and reduced because of the PSCs at each shaded P-V curve. The abbreviation of the parameters in Table 3.1 are as follows; Number of series-connected cells (N_{ss}), Number of series-connected modules per string (N_{ser}), Open Circuit Voltage (V_{oc}), Voltage Maximum Power (V_{mp}), Parallel-connected modules per string (N_{par}), Short Circuit Current (I_{sc}), Current at MPP current (I_{am}), and power at MPP (P_{mp}).

3.4 MPPT Schemes Design

A DC-DC converter and MPPT algorithm is designed to supply stabilized voltage and current to load and remove the ripple components. To calculate an error value, a measured and reference secondary voltage of the converter is compared. Proper tuning of the control variables such as duty cycle and reference voltage provides a minimized error value. Proportional integral (PI) controllers are used in this research because of their high stability, optimal operation, smooth auto-tuning process, and inexpensive design. Proportional (K_p) and integral (K_i) gain parameters are applied to control the present and residual cumulative past errors of the PI controller. The tuning terms' summed value is referred to a control variable that can be positive, negative, large, or small depending on the tuning of proportional parameter and the size of residual error. The residual tuning in the integral term only functions when the proportional term cannot minimize the error. A perturbation size of the duty cycle has to be enlarged if an operating point is located far from the GMPP location, and the reference voltage shows extreme positive or negative values. The operating point reaches the GMPP location when the error is optimized to approximately zero. The aim of using the PI controller is to maintain the operating point (by adjusting the error between measured and reference values) as close to MPP voltage and current so that the input voltage of the inverter can be stable without any ripple components. An MPPT algorithm initially produces the reference voltage fed by the PI controller to compare with the boost converter's measured output voltage. The perturbation size of the duty cycle is adjusted based on the generated error value from the two-terms PI controllers. The duty cycle is modulated with a triangular waveform to generate PWM switching pulses of the converter. In this combined PI-MPPT method, the PV string variables' response is adjusted to determine a desired constant output voltage and current of the boost converter to make a reliable operation of the FB-VSI.

3.4.1 P&O-MPPT Algorithm

Figure 3.3 depicts a conventional P&O-MPPT in which voltage is measured and perturbed as a control variable instead of a duty cycle.

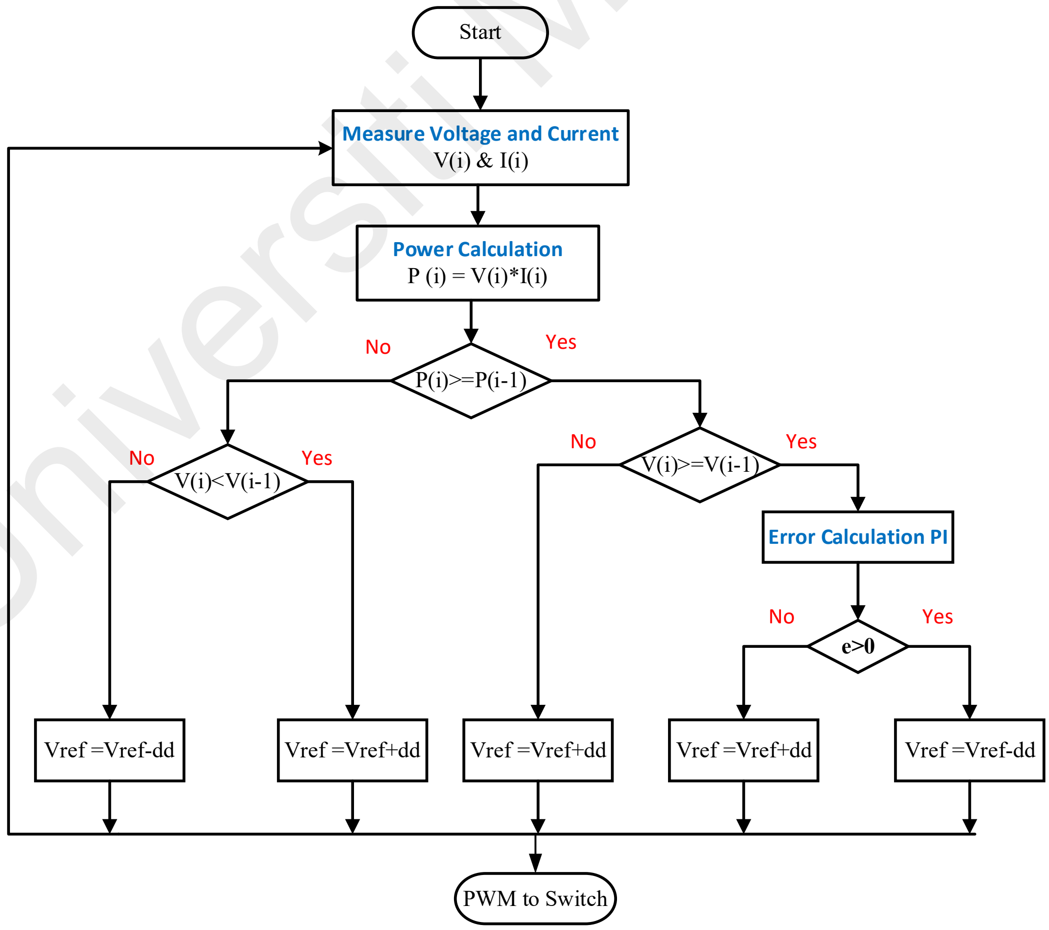

Figure 3. 3: A Flow Chart of P&O-MPPT

This algorithm initially measures photovoltaic panel voltage and current to compute an active power. When the new measured power is found greater than or equals to a stored power from a PV panel, the operating point needs to measure voltage difference. If the present voltage difference is greater than or equals to the past voltage value, an error is measured and calculated by the MPPT algorithm. If the error is larger than zero, the reference voltage must be increased by approximately 1 V and vice versa. The PI controller is activated if the panel voltage causes an increment of the boost converter's input extraction power. Hence, both the PI and MPPT algorithm manipulates the error, and perturb duty cycle based on the reference variables. The PI controller is executed and regulated by the trial adjustments of its two gain parameters to achieve satisfactory improvement over an open-loop grid-tied photovoltaic power plant interconnected with the P&O algorithm.

3.4.2 INC-MPPT Algorithm

This closed-loop incremental conductance algorithm is used to tune the perturbation size of a duty cycle to enable the operating point to track GMPP location when solar irradiance increases or decreases with a steep slope. In this circumstance, this algorithm is suitable to minimize oscillations around MPP and tracks the GMPP faster than the conventional INC technique. A continuous mode boost converter cannot identify a specific zone for the expected MPP location. However, this INC algorithm is developed to trace GMPP location with better accuracy and precession. An accurate perturbation step size of a duty cycle must keep the output voltage of the boost converter constant under the PSCs on the PV array. However, this INC-MPPT algorithm is only suitable for use in the grid-connected PV system if there is no partial shading condition, and the GMPP is located on the right side of a shaded P-V curve along with other LMPPs. The closed-loop INC algorithm also has the disadvantage of selecting a dynamic perturbation size of the reference variable under weather change. In this closed-loop INC-MPPT, choosing an accurate step size of a duty cycle is very difficult under PSCs because of a proportional relationship between enhanced tracking speed and massive power oscillation, and vice versa. This closed-loop INC algorithm is failed to decide which duty cycle value is a perfect solution under PSCs exclusively when an operating point is at the close vicinity of the GMPP location on a partially shaded P-V curve. Hence, this algorithm's optimum robustness and tracking performance are not acquired under the partially shaded curves (c) and (d), as shown in Figures 4.1 and 4.22. However, it may reduce the amount of power oscillation and increase tracking speed if there is no abrupt change in solar insolation and no heavily shaded non-linear P-V curve. Figure 3.4 shows the INC-MPPT technique with a voltage-controlled proportional-integral controller is used to realize the duty cycle to track a correct GMPP location.

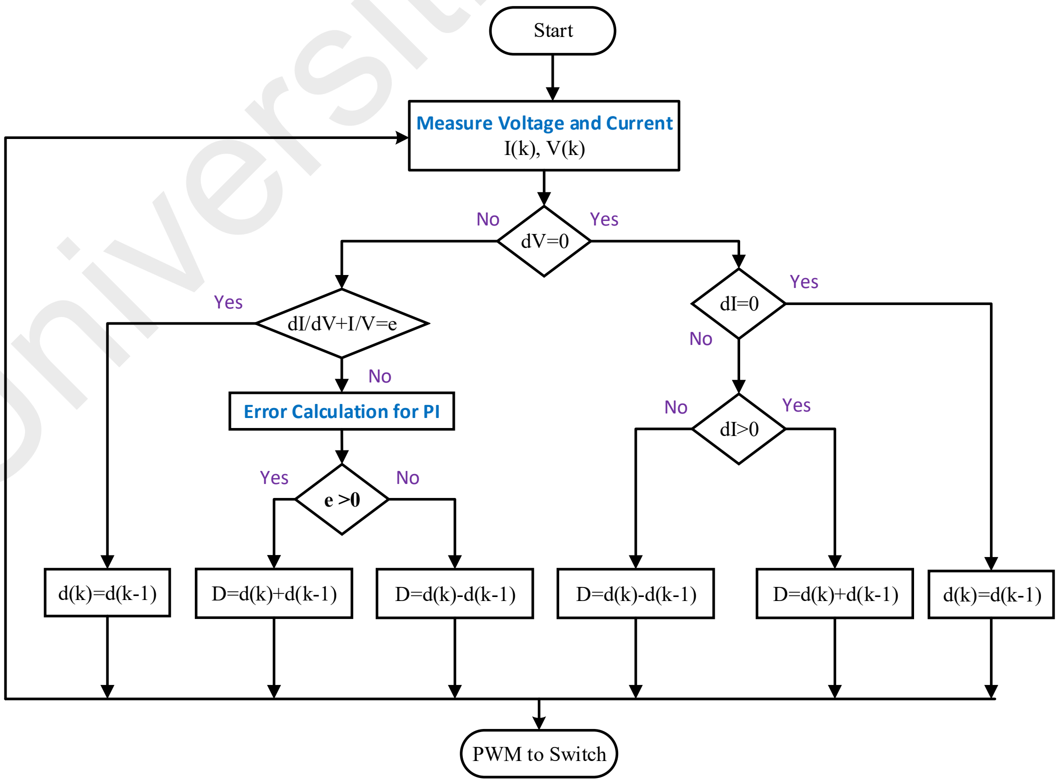

Figure 3. 4: A Flow Diagram of INC-MPPT

A PI controller is used to track an optimal value of PV voltage by minimizing the gradient value error on a P-V curve. An error 'e' is delivered to the PI controller as calculated in Eq. (3.1). An instantaneous gradient (dI_{pv}/dV_{pv}) of the P-V curve increments huge power oscillation nearer to the GMPP at dynamic weather conditions.

$$e = \frac{I_{pv}}{V_{pv}} + \frac{dI_{pv}}{dV_{pv}} \tag{3.1}$$

The perturbation step size (ΔD) of a duty cycle is measured by the PI controller and added up with or subtract from a pre-defined duty cycle because of driving the operating point at the best region of the GMPP location. The PI controller optimizes the step size (ΔD) based on the mathematical sing of the error (e) value.

$$\frac{I_{pv}}{V_{pv}} = -\frac{dI_{pv}}{dV_{pv}} \quad \text{at MPP} \tag{3.2}$$

Eq. (3.2) shows a slope (dP/dV) of the P-V curve equals zero when the power of a PV array reaches the GMPP. This equality of the voltage-power slope is never satisfied in practice; thus, a PI compensator is employed to force the slope into zero. In turn, this provides a comparatively reliable operation of the designed PV system with highly efficient tracking performance and limiting power oscillations in dynamic weather conditions. However, this INC-MPPT method is useful only in some instances, mainly if it operates in a uniform weather condition and a shaded condition in which GMPP locates at the right corner of the P-V curve among other multiple power peaks.

3.4.3 Proposed Coordinated PI-MPPT Algorithm

The conventional P&O and INC MPPT methods are used to increase or decrease the perturbation size of a control variable to drag an operating point toward an expected GMPP region. But, they cannot predict an accurate step size of a control value closest to the reference one when there is an adverse weather condition realized on the P-V curve. Generally, power losses on the P-V curve are diminished with slow tracking speed if the smallest possible step size of a control parameter (e.g., duty cycle or reference voltage) is chosen near the GMPP. If a smaller step size of a control parameter is chosen near the GMPP, power losses on the P-V curve decrease with low tracking speed. The proposed coordinated PI-MPPT algorithm integrates additional PI observers to address a speed-oscillation tradeoff when an operating point is about to track the GMPP in dynamic weather conditions. The PI controllers are dedicated to controlling both the current and voltage of the boost converter in cooperation with the proposed MPPT algorithm to stabilize a full bridge grid-tied inverter (the VSI). Besides, the proposed MPPT algorithm as an improved technique is deployed in a closed-loop grid-connected PV system to operating under dynamic weather conditions (exhibiting numerous multiple power peaks on P-V curves), unlike a conventional open-loop photovoltaic system. Nevertheless, the proposed PI-MPPT technique is superior to the traditional closed-loop MPP trackers in convergence speed, tracking speed, and power oscillations around the GMPP location.

This study uses a trial and error approach to predict the gain parameters of the PI controllers. The optimum tuned parameters such as proportional gain (K_p) and integral gain (K_i) are obtained by tuning the PI controllers and performing a closed-loop response. Hence, the optimum tuned parameters of the PI controllers are calculated to minimize the power oscillations around the GMPP. Then, an INC algorithm is applied to control the boost converter. The parameters of PI controllers are presented in Table 3.2. Thus, the optimum PI-tuning parameters necessary for minimizing the oscillations around the MPP can be found. The proposed algorithm includes two PI controllers to control both input current and output voltage and the duty cycle of the boost converter to achieve the PV system's maximum power efficiency.

Table 3.2: Tuning Gains of the PI-1 and PI-2

Parameters/PSCs	PI Controller 1		PI Controller 2	
	K_p	K_i	K_p	K_i
STC	0.008	9.5	0.025	2.51
Shading condition 1	0.012	20.3	0.05	3.25
Shading condition 2	0.017	50.8	0.502	5.32
Shading condition 3	0.205	100.2	0.8	8.71

The proposed algorithm takes a feedback voltage and current from the PV array as input and generates the optimal duty cycle to track the GMPP. The PWM generator then compares the duty cycle with a high-frequency carrier wave to generate a switching pulse for the boost converter switch. An increase in duty cycle proportionally increases the output current and decreases the PV module's output voltage. The boost converter's output power is not directly proportional to the duty cycle but the output current and voltage of the PV module.

The proposed MPPT method finds the GMPP location on a P-V curve by iteratively perturbing the input current and output voltage of the boost converter and comparing the PV power (P_{pv}) and the output power of the boost converter (P_o) as shown in Figure 3.5. The voltage and current perturbations are achieved through the changes in the duty cycle (ΔD). The sign of error ($\Delta P = P_{pv} - P_o$), is used to determine the direction of an operating point. The voltage error (ΔV) is the difference between the output reference voltage ($V_{o,ref}$) and measured output voltage (V_o) of the boost converter. If the power and voltage differences are together greater than zero ($\Delta P \geq 0$ and $\Delta V \geq 0$), PI-1 is activated to reduce error one (e_1). Then, PI-2 is operated to minimize an error (e_2) or ($\Delta I = I_{ref} - I_{pv}$), and the duty cycle is increased to make a constant output power of the converter. Initially, an input reference current ($I_{pv,ref}$) and output reference voltage ($V_{o,ref}$) of the boost converter are chosen to be 8.14 A and 325 V for simulation work, respectively. The proposed algorithm can reverse the present perturbation condition when PV power is decreased under the PSCs. The perturbation of the duty cycle keeps continuous until the GMPP location of the P-V is achieved. The proposed algorithm produces a constant value of the duty cycle at the steady-state condition when an operating point reaches the GMPP location on the partially shaded P-V curves. To increase system stability, the power oscillations around the GMPP location on the P-V curve have to be zero; thus, the operating point stops perturbing the duty cycle when the ΔP reaches zero or practically equals an approximately zero value.

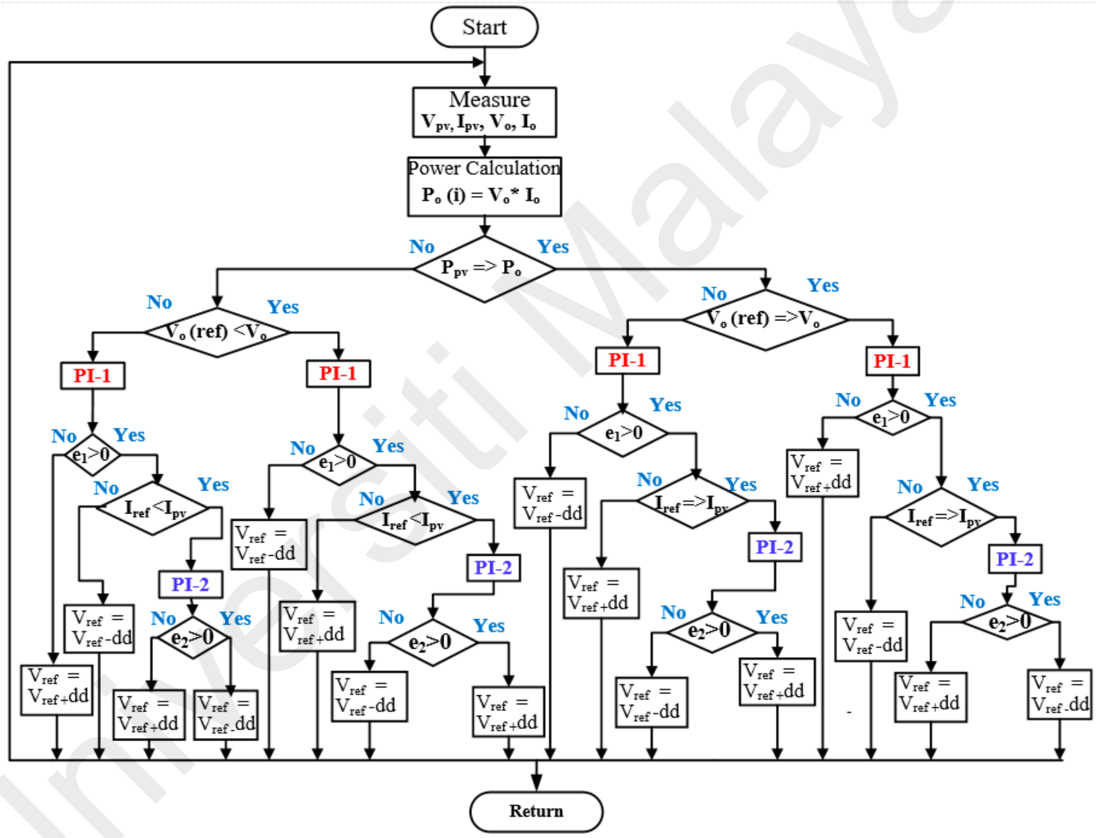

Figure 3. 5: A Coordinated Proposed PI-MPPT Algorithm

The proposed PI-MPPT method's main improvements over conventional ones are convergence and tracking speeds and power oscillations around the GMPP under the PSCs. The initial input of the PI controllers is a reference voltage ($V_{o,ref}$) at which the PV system is set to work, as shown in Figure 3.6. Hence, to achieve maximum PV power, a GMPP voltage must be equal to this initial input voltage at which the system must operate. When the operating point of the proposed MPPT reaches the GMPP location, it stops searching for another MPP on the P-V curve until there is a change in weather conditions.

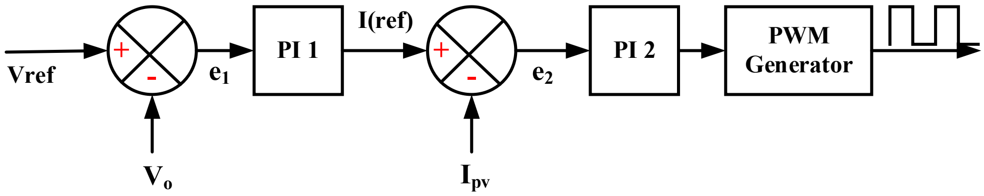

Figure 3. 6: A Function Block of the PI Controllers

The PSCs change the shapes of both P-V and I-V curves and shift the LMPPs and the GMPP's location, resulting in power loss and downgrade overall system efficiency. However, the proposed algorithm is designed to track the $GMPP_r$, $GMPP_m$, and $GMPP_l$ locations by overlooking the other two LMPPs when three types of PSCs reshaped a P-V curve generated from uniform weather case as shown in Figures 4.1 and 4.22.

3.5 DC-DC Boost Converter Design

In this research work, a boost converter is designed to step-up the PV array voltage from 184 V to 360 V DC under uniform weather and the PSCs. The boost converter's output voltage is not constant when only a PWM is applied to control an insulated-gate bipolar transistor (IGBT) or metal-oxide-semiconductor field-effect transistor (MOSFET) switch in the open-loop system. In a closed-loop system, PI controllers and PWM and MPPT techniques are combined with maintaining a constant output voltage (360V) at the PSCS by regulating the converter's range of duty cycle between 0.2 and 0.82. The PWM signal controls the switch's opening and closing (transistor/MOSFET) with a switching frequency of 10 KHz and controls the duty cycle. The PWM pulses are generated by comparing a reference voltage with a triangular waveform with a constant amplitude of the voltage and frequency. When the amplitude of a reference voltage is greater than a saw-tooth waveform, the switch of the boost converter is OFF to calculate output power and the inductor power. When the amplitude of the reference sinusoidal voltage is lower than the saw-tooth waveform, the IGBT is closed, and the diode of the boost converter is started functioning in reverse bias condition, which isolates the output circuit from the input. The duration between the ON-period and the OFF-period of the boost converter provides an average output voltage of the boost converter; hence the duty cycle varies. The boost converter operates in continuous conduction mode (CCM) and discontinuous conduction mode (DCM). The CCM of the boost converter is widely used in a grid-connected PV system to extract maximum power from non-linear P-V curves.

3.5.1 Principle and Circuit Elements Design

The boost converter's main circuit component is an inductor that stores energy—the inductor functions as a load and source in the charging and discharging periods, respectively. During the inductor's discharge state, a DC voltage across the capacitor is deepened on the rate of change of the inductor current. Figure 3.7 (a) and (b) show ON and OFF conditions of a boost converter switch, respectively.

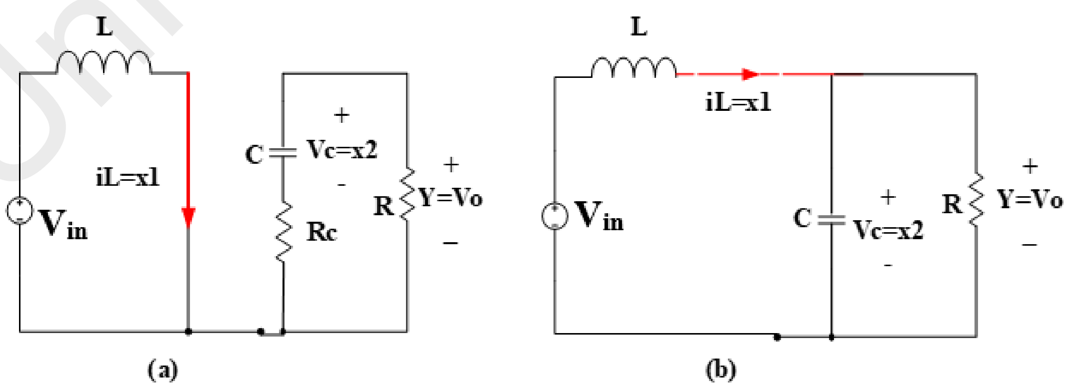

Figure 3. 7: Boost converter configurations; (a) switch ON (b) Switch OFF

The inductor stores energy when a magnetic field is created across it because of clockwise current flow. In the ON-state of the switch, input voltage (V_{in}) of the converter is calculated across the inductor L, which causes a change in inductor current (i_L) for a period as represented in Eq. (3.3). At the end of the ON-state, an increase in the inductor current (i_L) is calculated using Eq. (3.4). T defines as a total period when the converter switch is ON. The switch is in the ON and OFF states when the converter's duty cycle is maximum and zero, respectively. (Hu, Yin, & Ghaderi, 2020). The current across the inductor (I_L) is calculated in Eq. (3.5) and Eq. (3.6) for both ON and OFF states of the converter switch, respectively. Circuit elements of the CCM mode boost converter store the same amount of energy at the beginning and the end of a commutation cycle. Eq. (3.7) shows how to calculate the inductor's energy (Sadaf, Bhaskar, Meraj, Iqbal, & Al-Emadi, 2020). From Eq. (3.7), the inductor current's overall change between ON and OFF states of the switch is zero, as represented in Eq. (3.8). Eq. (3.9) is written by substituting the slope changes of the inductor current in both ON and OFF states are ΔI_{Lon} and ΔI_{Loff}, respectively. From Eq. (3.9), we obtain a ratio between output and input voltages (V_{out}/V_{in}) of the converter as is written in Eq. (3.10). From Eq. (3.10), the duty cycle (D) is calculated as a subject as depicted in Eq. (3.11).

$$\frac{\Delta I_L}{\Delta t} = \frac{V_{in}}{L} \tag{3.3}$$

$$\Delta I_{Lon} = \frac{1}{L}\int_0^{DT} V_{in}\,dt = \frac{DT}{L} V_{in} \tag{3.4}$$

$$V_{in} - V_{out} = L\,\frac{dI_L}{dt} \tag{3.5}$$

$$\Delta I_{Loff} = \int_{DT}^{T} \frac{(V_{in} - V_{out})\,dt}{L} = \frac{(V_{in} - V_{out})\,(1 - D)\,dt}{L} \tag{3.6}$$

$$E = \frac{1}{2}\ LI_L^2 \tag{3.7}$$

$$\Delta I_{Lon} + \ \Delta I_{Loff} = 0 \tag{3.8}$$

$$\Delta I_{Lon} + \ \Delta I_{Loff} = \ \frac{(V_{in}\ DT)}{L} + \frac{(V_{in} - V_{out})\ (1 - D)\ T}{L} \tag{3.9}$$

$$\frac{V_{out}}{V_{in}} = \frac{1}{(1 - D)} \tag{3.10}$$

$$D = 1 - \ \frac{V_{out}}{V_{in}} \tag{3.11}$$

(a) ***Boost converter switch design***

The switch of a boost converter can be a MOSFET, bipolar junction transistor (BJT), IGBT, or junction field-effect transistor (JFET). The MOSFET has three legs called a drain, gate, and source controlled through the gate pin that receives a PWM signal from the MPPT algorithm. The converter's maximum output current is the same as the forward current as presented in Eq. (3.12). I_F is an average forward current of the rectifier diode, I_{out} is the maximum output current of the diode, and V_F stands for an average forward voltage of the rectifier diode (Rex & Praba, 2020).

$$I_F = \ I_{out\ (max)} \tag{3.12}$$

(b) ***Inductor design***

The inductor ripple current is estimated between 20% and 40%, as calculated in Eq. (3.13). The critical inductance value of the boost converter is written in Eq. (3.13). Where; input voltage, output voltage, switching frequency, and inductor ripple current are denoted as V_{in}, V_{out} , f_{sw} and ΔI_L respectively.

$$\Delta I_L = I_{out\,(max)} \times (20\% \text{ to } 40\%) \times \frac{V_{out}}{V_{in}} \tag{3.13}$$

(c) ***Output capacitor design***

A large filter capacitor is required to limit the output ripple voltage as calculated in Eq. (3.14). When the diode is OFF, the filter capacitor should supply DC voltage to the load. Output minimum capacitance ($C_{out\,(min)}$), output ripple voltage (ΔV_{out}), switching frequency (f_{sw}) in kHz, maximum output current ($I_{out\,(max)}$), and duty cycle (D) are needed to calculate the output capacitance of the boost converter as presented in Eq. (3.14). A selection of minimum capacitance (C_{min}) must be higher than the calculated value to ensure that the ripple components of the converter output voltage remain low. Equivalent series resistance (ESR) is minimized by connecting a parallel capacitor bank. Therefore, the ESR is calculated using the following Eq. (3.15) (Leng, Zhou, Tian, Xu, & Blaabjerg, 2020).

$$C_{out\,(max)} = \frac{D * I_{out\,(max)}}{\Delta V_{out} * f_{sw}} \tag{3.14}$$

$$\Delta V_{out\,(ESR)} = ESR * \frac{I_{out\,(max)}}{(1 - D)} + \frac{\Delta I_L}{2} \approx 5\% \quad V_{out} \tag{3.15}$$

3.5.2 Transfer Function of the Boost Converter

A state-space model is derived from the equivalent circuits of the converter to find a transfer function.

(a) ***Switch ON condition***

When the converter switch is ON, a relation between inductor current, capacitor voltage, and the output voltage is expressed in Eq. (3.15), Eq. (3.16), and Eq. (3.17).

$$L\frac{d_{i_L}}{dt} = V_{in} \text{ or } L\dot{x_1} = U_0 \tag{3.15}$$

$$C\frac{d_{V_c}}{dt} = -\frac{Y}{R} \text{ or } C\dot{x_2} = -\frac{Y}{R} \tag{3.16}$$

$$Y = \frac{R\,x_2}{(R + R_c)} \tag{3.17}$$

(b) ***Switch OFF conditions***

Similarly, mathematical expressions are derived for the inductor current, input voltage, and output voltage are written in Eq. (3.18), (3.19), and (3.20) when the converter switch is in OFF mode.

$$U_0 = L\frac{d_{i_L}}{dt} + Y \text{ or } L\dot{x_1} = U_0 - Y \tag{3.18}$$

$$i_L = C\frac{d_{V_c}}{dt} + \frac{Y}{R} \text{ or } C\dot{x_2} = x_1 - \frac{Y}{R} \tag{3.19}$$

$$Y = \frac{R * x_2}{(R + R_c)} + \frac{R * R_c * x_1}{(R + R_c)} \tag{3.20}$$

For a switching period (T_s), the differential equations (non-linear state equations) are averaged over one switching period consisting of ON-time ($d\,T_s$) and OFF-time ($(1-d)T_s$) of the switch. Three equations, Eq. (3.21), Eq. (3.22), and Eq. (3.23), are derived from calculating the state-space variables in the ON and OFF switching conditions.

$$\dot{x_1} = \frac{U_0}{L} - \frac{R * x_2}{L\,(R + R_c)}\,(1-d) + \frac{R * R_c * x_1}{L\,(R + R_c)}\,(1-d) \tag{3.21}$$

$$\dot{x_2} = -\frac{x_2}{C\,(R + R_c)} + \frac{R * x_1}{C\,(R + R_c)}\,(1-d) \tag{3.22}$$

$$Y = \frac{R * x_2}{(R + R_c)} + \frac{R * R_c * x_1}{(R + R_c)} \quad (1 - d) \tag{3.23}$$

The above three equations are linearized to obtain the transfer function of the boost converter. The boost converter operates at the steady-state condition with a duty cycle (D), inductor current (x_{10}), capacitor voltage (x_{20}) and output voltage (Y_0). A small-signal perturbation ($\hat{d}$) is applied to the duty cycle (d). As a result, a small signal perturbation in the inductor current, capacitor voltage, and output voltage are shown respectively in Eq. (3.24). The non-linear average state-space equations are obtained by ignoring the terms formed by two small signal quantities. The derived equations are Eq. (3.25) and Eq. (3.26) and Eq. (3.27).

$$d = D + \hat{d}\,, x_1 = x_{10} + \hat{x}_1\,, x_2 = x_{20} + \hat{x}_2\,, Y = Y_0 + \hat{Y} \tag{3.24}$$

$$\widehat{x_1} = -\frac{R * R_c * \acute{D}}{L\,(R + R_c)}\ \hat{x}_1 - \frac{R * \acute{D}}{L\,(R + R_c)}\ \hat{x}_2 + \left[\frac{R * R_c}{L\,(R + R_c)}\ x_{10} + \frac{R}{L\,(R + R_c)}\ x_{20}\right]\widehat{d} \tag{3.25}$$

$$\hat{x}_2 = \frac{R * \acute{D}}{C\,(R + R_c)}\ \hat{x}_1 - \frac{x_2}{C\,(R + R_c)} - \frac{R}{C\,(R + R_c)}\ x_{10}\ \hat{d} \tag{3.26}$$

$$Y = \frac{R * \hat{x}_2}{(R + R_c)} + \frac{R * R_c * \acute{D}}{(R + R_c)}\ \hat{x}_1 - \frac{R * R_c}{(R + R_c)}\ x_{10}\ \widehat{d} \tag{3.27}$$

These sets of equations represent the average steady-state model for boost converter linearized around an operating point (D, x_{10}, x_{20}). A low ESR resistance (R_c) is compared to load resistance (R). The standard state-space model is presented by the matrices A, B, and C and Eq. (3.28). The state-space system of the transfer function is developed with perturbation size ($\hat{d}$) to output ($\hat{y}$) is given in Eq. (3.33).

$$\dot{x} = Ax + Bd\,, \qquad Y = Cx + Ed \tag{3.28}$$

$$A = \begin{bmatrix} -\frac{R_c * \acute{D}}{L} & -\frac{\acute{D}}{L} \\ \frac{\acute{D}}{C} & -\frac{1}{C\,R} \end{bmatrix} \tag{3.29}$$

$$B = \begin{bmatrix} \frac{R_c}{L}\, x_{10} + \frac{1}{L}\, x_{20} \\ -\frac{1}{C}\, x_{10} \end{bmatrix} \tag{3.30}$$

$$C = [\, R\, C\, \acute{D} \quad 1 \,] \tag{3.31}$$

$$E = -R\, C\, x_{10} \tag{3.32}$$

$$\frac{\hat{y}}{\hat{d}} = U_0 \frac{\left(1 - S\frac{L}{R\ \acute{D}^2}\right)(1 + S\, R_c\, C)}{L\, C\, S^2 + S\left(\frac{L}{R} + R\, C\, \acute{D}\right) + \acute{D}^2} \tag{3.33}$$

The parameters of the boost converter are written in Table 3.3.

Table 3.3: Boost converter parameters

Parameters Name/values	Symbols	Simulation	Experimental
Input voltage range	V_{in}	118-360 V	68.2-195 V
Output DC-link voltage	V_{cdc}	360 V	60 V
Switching frequency	f_{sw}	10 kHz	10 kHz
Nominal DC-Link Voltage	$V_{dc}^{nominal}$	400 V	100 V
Duty Cycle Range	ΔD	0.18-0.829	0.152-0.778
Rated Power	P_{rated}	1.5 kW	0.23 kW

3.6 Grid-Connected FB-VSI Design

A single-phase voltage source inverter (VSI) is designed by considering a power stage and control mechanisms. The VSI is categorized into two types based on the number of switches, such as a half-bridge inverter and a full-bridge FB-VSI. The VSI is also divided into three distinct categories: boost, buck, and buck-boost, based on the magnitude of the inverter output and input voltages (Albatran, Allabadi, Al Khalaileh, & Fu, 2020). In this dissertation, an H-bridge buck type full-bridge inverter topology is chosen due to its simplicity and high efficiency. The topology of an H-bridge inverter is shown in Figure 3.8. In this research work, approximately 400 volts DC is supplied from the boost converter to the VSI input, and 240 V RMS AC is generated by the H-bridge Inverter. Proportional Resonance (PR) controllers keep the grid current constant and remove the steady-state error (SSE) from the sinusoidal current signal.

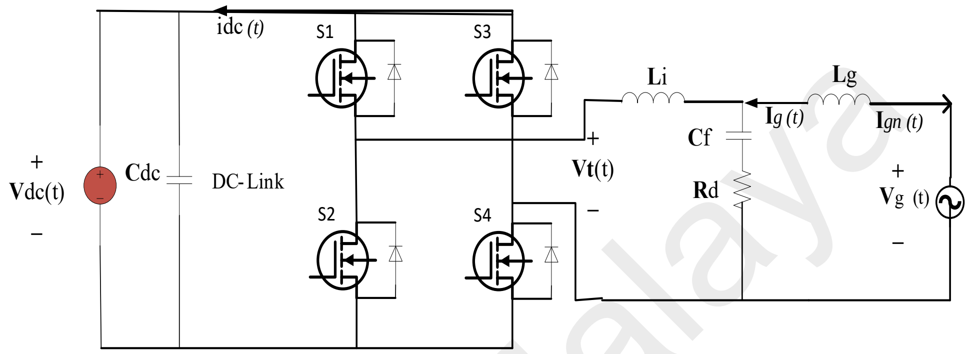

Figure 3. 8: Grid-Connected H-bridge Inverter Topology

3.6.1 Switching Circuit Configurations of the VSI

A full-bridge buck type VSI is developed with bipolar SPWM techniques. The VSI receives the DC-link voltage of the boost converter and converts it into an equivalent RMS AC voltage of the grid. A MOSFET is used instead of IGBT as a switch because it can be operated at a high switching frequency (f_{sw}>20 kHz) without switching loss, resulting in the small size of the circuit components is required to design the VSI. Moreover, a bipolar SPWM technique can shift major harmonic distortion of the output voltage of the VSI from (m_f-1) frequency level to ($2m_f - 1$) to remove the second harmonic component. Hence, an inductor-capacitor-inductor (LCL) filter requires a small size of its components. AC harmonic voltage is started appearing on the VSI waveform when a normalized modulation frequency or frequency modulation ratio (m_f >9) with modulation index (m_a) range ($0 < m_a < 1$). Harmonic frequencies are centered around the switching frequency as sidebands such as m_f, $2m_f$, and $3m_f$.

3.6.2 DC-Link Capacitor at the Input of the Inverter

Figure 3.9 shows a DC-link voltage with ripple components. The DC-link capacitor's size is calculated using Eq. (3.4), which removes the double-line frequency ripple component of the voltage. Grid voltage and current are derived in Eq. (3.34) and Eq. (3.35), respectively. Then, an instantaneous output power of the VSI is obtained by using Eq. (3.36):

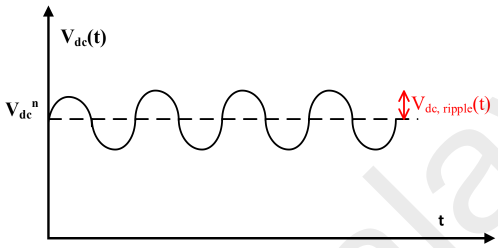

Figure 3. 9: DC-Link Voltage

$$v_g(t) = \hat{V}_g \cos(\omega_g t) \tag{3.34}$$

$$i_g(t) = \hat{I}_g \cos(\omega_g t - \phi) \tag{3.35}$$

$$P_{out}(t) = \hat{V}_g \cos(\omega_g t) * \hat{I}_g \cos(\omega_g t - \phi) = V_g^{rms} I_g^{rms}(\cos\phi + \cos(2\omega_g t - \phi))$$

$$= S(\cos\phi + \cos(2\omega_g t - \phi)) \tag{3.36}$$

Where; S is an apparent power (volt-ampere (VA)). In ideal VSI, input and output instantaneous powers must be the same amount. High-frequency ripple components of the DC current (i_{dc}) are filtered out by a DC-link capacitor. Eq. (3.37) and Eq. (3.38) represent a nominal voltage (V_{dc}^{n}) and DC current (I_{dc}) of the DC-link capacitor, respectively. The ripple component of the DC current is calculated using Eq. (3.39). The capacitance of the DC-link capacitor is obtained considering a maximum allowable ripple voltage ($V_{dc,ripple}^{max}$), using Eq. (3.40). Hence, substituting modeling parameters of the VSI, DC-link voltage (C_{cdc}) is calculated using Eq. (3.41).

$$V_{dc}^{n}\, i_{dc}(t) = S\left(\cos\phi + \cos\left(2\omega_g t - \phi\right)\right) \tag{3.37}$$

$$I_{dc} = \frac{S\cos\phi}{V_{dc}^{n}} \tag{3.38}$$

$$i_{dc,\ ripple}(t) = \frac{S\cos\left(2\omega_g t - \phi\right)}{V_{dc}^{n}} = \hat{I}_{dc,\ ripple}\cos\left(2\omega_g t - \phi\right) \tag{3.39}$$

$$C_{dc} = \frac{\hat{I}_{dc,\ ripple}}{2\ \omega_g\ V_{dc,ripple}^{max}} = \frac{S}{2\ \omega_g\ V_{dc,ripple}^{max} V_{dc}^{n}} = \frac{P_{pv}}{2 * V_{dc} * \Delta V_{dc} * \omega_g} \tag{3.40}$$

$$C_{dc} = \frac{(1.5 * 1)\ kVA}{2 * 50 * 3.1415 * 12\ V * 400\ V} = 995\ \mu\mathbf{F} \tag{3.41}$$

In this research work, a 1000 μF DC-link capacitor is selected based on Eq's calculation (3.41). Similarly, the capacitance of the input capacitor of the boost converter is chosen to be 1000 μF. In Eq. (3.40), ω_g stands for the angular frequency of the grid voltage, P_{pv} is an apparent power of the PV array, V_{dc} is an average DC-link voltage, and ΔV_{dc} is defined as a minimum ripple of the DC-link voltage. The parameters of the VSI are written in Table 3.4.

Table 3.4: Parameters of the VSI

VSI parameters /values	Symbols	Simulation	Experimental
Rated grid voltage/frequency	V_g^{Rated}	250 V (RMS) /50 Hz	60 V (RMS) /50 Hz
Rated grid current	I_g^{Rated}	8.71 A (RMS)	4.25 A (RMS)
Switching frequency	f_{sw}	10 kHz	10 kHz
Nominal DC-Link Voltage	$V_{dc}^{nominal}$	400 V	100 V
DC-link voltage % ripple	NA	10%	10%
DC-link Capacitance	C_{cdc}	945 μF	450 μF

3.6.3 LCL type LPF Filter Design

A low-pass filter (LPF) is used to obtain the output voltage and current of the VSI with a fundamental frequency (50 Hz). The VSI is operated with a high switching frequency to remove total harmonic distortion (THD) and minimize the size of the circuit components of a low pass filter (LPF). Figure 3.10 shows an LCL-LPF that is chosen because of its good performance and simple design. An inductance (L_i) at the VSI side of the LPF is calculated by considering 10% of the maximum allowable ripple current (Δi_{max}) through it shown in Eq. (3.49) ((Sgrò, Souza, Tofoli, Leão, & Sombra, 2020).

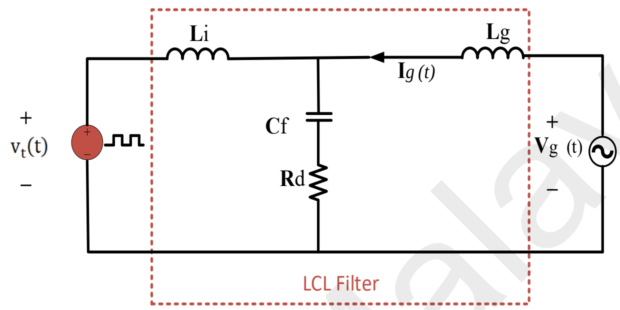

Figure 3. 10: The LCL Filter Circuit

A bipolar SPWM technique limits the flow of leakage current through the VSI inductor (L_i) without the requirement of galvanic isolation (Sarker, Datta, & Debnath, 2020). Terminal voltage ($V_t(t)$) of the VSI consists of a fundamental frequency and high order harmonic components. The LCL filter's transfer function is derived using the superposition theorem as calculated in Eq. (3.44). Eq. (3.43) is derived from Eq. (3.42) by considering the grid voltage (V_g) zero, which represents a transfer function between grid current and the terminal voltage of the VSI. Root means square (RMS) of the high order frequency component of the $V_t(t)$ is calculated using Eq. (3.45), reading a look-up table of the nominal DC-link voltage (V_{dc}^{n}). Combining Eq. (3.44) and Eq. (3.45), the RMS value of the harmonic current is calculated in Eq. (3.46). The magnitude of the filter transfer function $|H_f(jh\omega_g)|$ is calculated using the 0.37 value of the k(h) at $(2m_f - 1)$.

$$\left.\frac{I_g(s)}{V_t(s)}\right| = \frac{s\,C_f\,R_d + 1}{S^3\,C_f\,L_g\,L_i + S^2\,C_f\,R_d\left(L_i + L_g\right) + s\left(L_i + L_g\right)} \tag{3.42}$$

$$\left.\frac{I_g(s)}{V_t(s)}\right| = H_f(s) = \frac{S^2\,C_f\,L_i + s\,C_f\,R_d + 1}{S^3\,C_f\,L_g + S^2\,C_f\,R_d\left(L_i + L_g\right) + s\left(L_i + L_g\right)} \tag{3.43}$$

$$\left.\frac{I_g(s)}{V_t(s)}\right| = H_f(s) = \frac{s\,C_f\,R_d + 1}{S^3\,C_f\,L_g + S^2\,C_f\,R_d\left(L_i + L_g\right) + s\left(L_i + L_g\right)} \tag{3.44}$$

$$\left|V_t(jh\omega_g)\right| = \frac{1}{\sqrt{2}}.2.\frac{\left(\hat{V}_{A_o}\right)h}{\frac{1}{2}\;V_{dc}^{n}}.\frac{V_{dc}^{n}}{2} = \frac{1}{\sqrt{2}}.k(h).\;V_{dc}^{n} \tag{3.45}$$

$$\left|I_g(jh\omega_g)\right| = \frac{1}{\sqrt{2}}.\left|H_f(jh\omega_g)\right|.k(h).\;V_{dc}^{n} \tag{3.46}$$

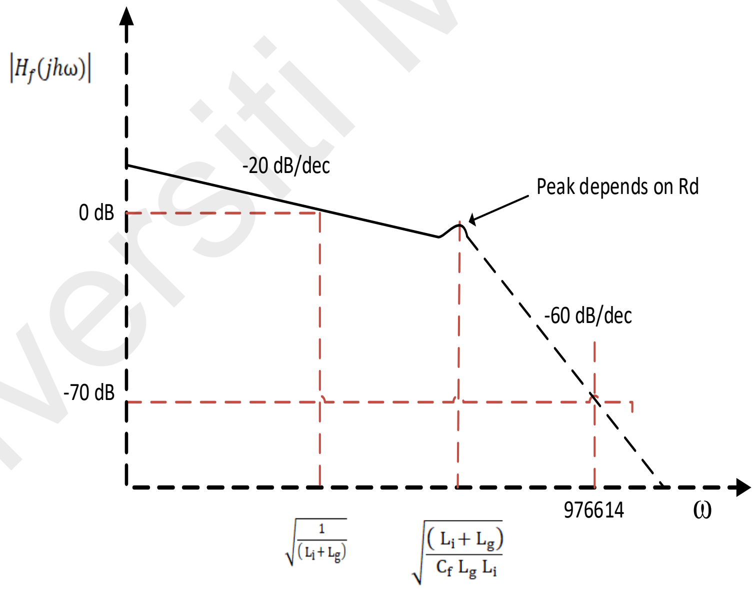

Figure 3. 11: Magnitude Plot of the Filter Transfer Function

Figure 3.11 shows a generic magnitude plot of $H_f\,(s)$ represented in Eq. (3.47), including the transfer function of the LCL filter derived in Eq. (3.44).

$$|H_f(j(2m_f - 1)377)| = |H_f(j250956)| = 0.3\%.\sqrt{2}.\frac{10}{400V * 0.37} = -70 \tag{3.47}$$

When angular frequency (ω) equals 376614, the magnitude of $H_f(j250956)$ is calculated at approximately 70 dB. The size of the LPF filter elements (L_i, L_g, C_f , and R_d) is calculated and shown in Table 3.4, using the magnitude plot of the filter transfer function. The resonance frequency (f_r) of the LPF is always should within the range of eq. (3.49) to have good system dynamics and overcome the resonance problem. Filter capacitance (C_f) is used to reduce overheating of the VSI. In this LCL filter design, an inductor (L_i) at the boost converter side is considered identical to the grid side inductor (L_g) to generate a low resonance frequency of the LPF. Eq. (3.48) shows a range of resonance frequency of the LPF filter in which f_g stands for grid fundamental frequency (50 Hz). Similarly, the values of converter side inductor (L_i), filter capacitance (C_f), and damping resistor (R_d) are calculated by using Eq. (3.49), Eq. (3.50), and Eq. (3.51), respectively. Designed parameters of the VSI specifications are written in Table 3.4.

$$10\ f_g < \left[f_r = \frac{1}{2\pi}\sqrt{\frac{(L_i + L_g)}{L_i\ L_g\ C_f}} \right] < 0.5\ f_{sw} \tag{3.48}$$

$$L_i = \frac{V_{CDC}}{6\ f_{sw}\ \Delta i_{max}} \tag{3.49}$$

$$C_f = \frac{S}{2\pi\ f_g\ V_g^2} \tag{3.50}$$

$$R_d = \frac{2\pi\ f_r\ C_f}{3} \tag{3.51}$$

Table 3.5: Specifications of the Inverter Elements

LCL-LPF parameters /values	Symbols	Values
Converter side inductor	L_i	3mH
Grid side inductor	L_g	3mH
Filter capacitance	C_f	55μ**F**
Damping Resistor	R_d	1.5Ω

3.6.4 VSI Control Design

This section of the VSI control includes current, DC-link voltage, and grid synchronization controllers. Current and Voltage controllers regulate the VSI current injected into the grid, and the DC-link voltage, respectively. A 1-ϕ VSI cannot control its active and reactive powers by simply adjusting direct current (i_d), and quadrature current (i_q) components at the d-q frame. Hence, a grid synchronizer (PLL) is used to create a reference of the grid current to the active and reactive powers' flow, as shown in Figure 3.12.

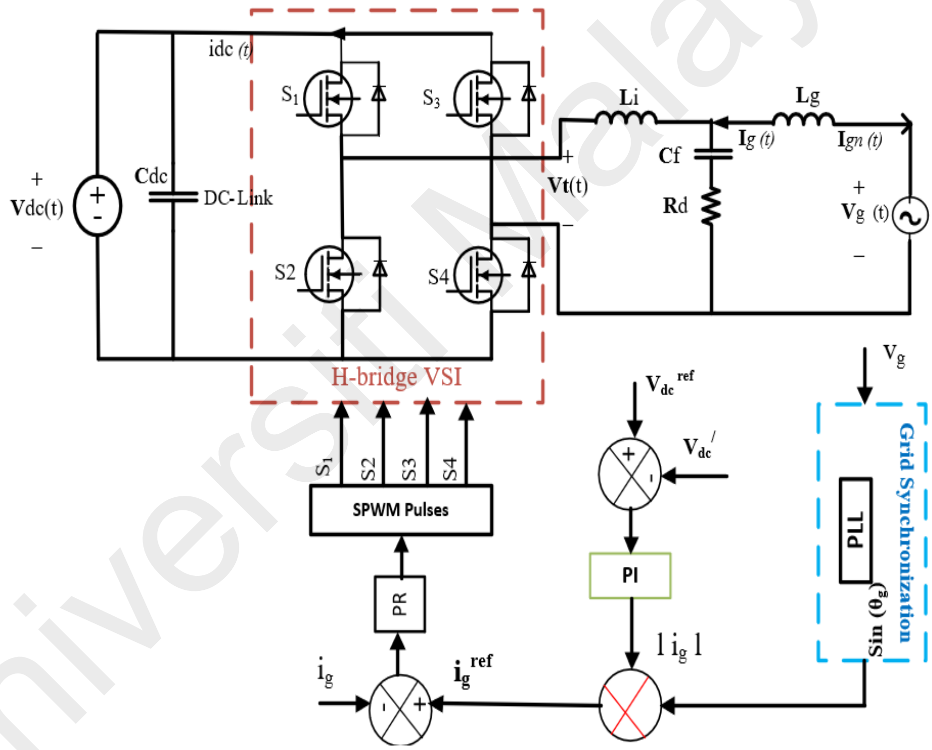

Figure 3. 12: A Complete Closed Loop Control System for the VSI

3.6.4.1 Bipolar SPWM Switching Control

THE bipolar SPWM technique is widely used to operate the switches of the VSI, generating the same amount of switching frequency for both complementary pulses (Sharif, 2018). In the SPWM technique, each pulse width varies proportionally with an amplitude of a sinusoidal reference waveform. Complementary pulses are generated by comparing a sinusoidal reference waveform with a high-frequency triangular carrier signal. Then, the amplitude of the pulses is boosted up approximately 12 to 16 V through gate drives. The modulation index is defined as an amplitude ratio between the sinusoidal and triangle signals. Modulation index can vary the amplitude level of the pulses. For example, overmodulation can increase the amplitude of the pulses and creates harmonic contents. Two pairs of the VSI switches are; (S1-S4) and (S2-S3) turned ON and OFF simultaneously, receiving complementary pulses from the bipolar SPWM technique. As a result, the VSI generates a square signal with the same amplitude of positive (+VDC) and negative (−VDC) voltage levels. The carrier wave and sinusoidal wave frequency are chosen to be 10 kHz and 50 Hz, respectively. Figure 3.13 shows a carrier and sine waves and two complementary pulses of the bipolar SPWM technique.

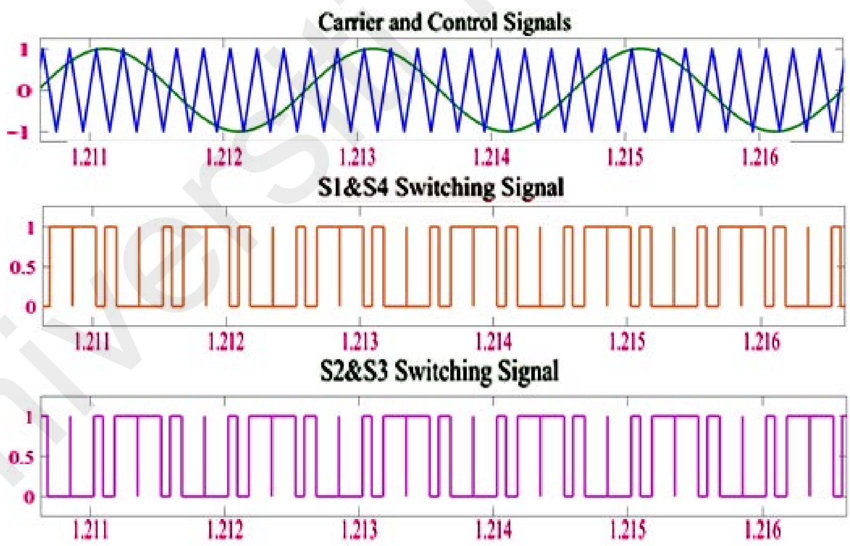

Figure 3. 13: Bipolar SPWM Control singles

3.6.4.2 Proportional Resonant Controller (PR)

The single-phase VSI uses a feedback current loop to regulate the grid current (I_g). For the VSI with a switching frequency of 10 kHz, a PI compensator is no longer sufficient to track the reference grid current with zero SSE. A higher-order compensator (PR) is needed as a substitute. The plant model of the VSI is derived in Eq. (3.49) and Eq. (3.50). When input terminal voltage (V_t) of the VSI is considered zero, the gain is calculated using Eq. (3.49).

$$G_f(s) = \frac{S^2 C_f L_i + s C_f R_d + 1}{s C_f R_d + 1} (V_g - V_t) \tag{3.49}$$

$$G_f(s) = \frac{s C_f R_d + 1}{S^3 C_f L_g L_i + S^2 C_f R_d (L_i + L_g) + s(L_i + L_g)} \tag{3.50}$$

Eq. (3.49) is simplified into Eq. (3.51) because magnitude and phase responses of the term $\left(\frac{S^2 C_f L_i + s C_f R_d + 1}{s C_f R_d + 1}\right)$ are 0dB and 0° at the fundamental frequency (50 Hz) of $V_g(j\omega)$.

$$I_g(s) = G_f(s)(V_g - V_t) \tag{3.51}$$

Figure 3.14. shows a current gain of the PR compensator ($G_i(s)$) and plant model

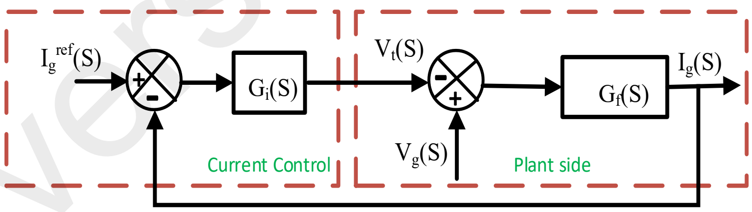

Figure 3. 14: A Current Control Block of the PR controller

The relationship between the input and the output of the current loop is written in Eq. (3.52), (3.53), and (3.54).

$$I_g(s) = H_i(s) I_g^{ref}(s) + H_v(s) V_g(s) \tag{3.52}$$

$$H_i(s) = \frac{G_f(s) G_i(s)}{G_f(s) G_i(s) - 1} \tag{3.53}$$

$$H_v(s) = \frac{G_f(s)}{1 - G_f(s)G_i(s)} \tag{3.54}$$

To track the grid reference current (I_g^{ref}) without leaving the SSE, the magnitude of $H_i\,(j\omega)$ in Eq. (3.53) equals 1 at the fundamental frequency (50 Hz) of the I_g^{ref} However, if $G_i\,(j\omega)$ has an infinite gain at the fundamental frequency, $H_i\,(j\omega)$ in Eq. (3.54) equals zero at the fundamental frequency so that the $H_v\,(j\omega)$ the term is neglected.

In an ideal PR compensator, gain $G_i\,(s)$ equals to infinite value at a cut-off frequency (ω_o) as represented in Eq. (3.55). The ideal PR compensator cannot eliminate the grid current's higher-order harmonic components because of its low gain response at other frequencies when the variation occurs in the grid frequency. Hence, the grid voltage's massive harmonic component causes a significant amount of harmonic distortion of the grid current. Therefore, a damping term, zeta (ζ), is included in the grid current's transfer function to make a non-ideal PR compensator presented in Eq. (3.56). The damping term (ζ) transforms an infinite gain of the grid current at the fundamental frequency to a finite large gain, but it needs to increase the compensator's bandwidth. The closed-loop gain of the PR compensator's current control loop is obtained by Eq. (3.57). Parameters of the PR compensator are written in Table 3.5.

$$G_i(s) = K_p^c + \frac{s\,K_i^c}{s^2 + \omega_o^2} \tag{3.55}$$

$$G_i(s) = K_p^c + \frac{s\,K_i^c}{s^2 + 2\omega_0\zeta s + \omega_o^2} \tag{3.56}$$

$$T_c(s) = G_i(s)\,G_f(s)$$

$$= \left(K_p^c + \frac{s\,K_i^c}{s^2 + 2\omega_0\zeta s + \omega_o^2}\right)\frac{s\,C_f\,R_d + 1}{S^3\,C_f\,L_g\,L_i + S^2\,C_f\,R_d\left(L_i + L_g\right) + s\left(L_i + L_g\right)} \tag{3.57}$$

Table 3.6: Parameters of PR controller

PR Parameters symbols	K_{PR}	K_R	ζ
Names	Proportional gain	Resonance gain	Damping term
Values	3	20000	0.01

3.6.5 Grid Synchronization Controller

A grid synchronization controller is used to filter out the grid voltage and current waveforms' noisy components and synchronize them in phase with the VSI voltage and current. It also emulates an orthogonal component of the grid voltage to generate reactive reference power of the VSI. Therefore, the VSI can control the flow of the reactive power better than other conventional inverters. Asynchronous reference frame phase-locked loop (SRF-PLL) controller is used to lock the grid voltage phase by detecting its zero voltage crossing (ZVC) and resetting the d-q frame to generate sine and cosine waveforms of the voltage. The SRF-PLL uses a two by two state matrix to generate parallel and orthogonal components of the grid voltage and current. The DC-link voltage is regulated by a closed-loop voltage controller presented in Eq. (3.58)

$$\mathrm{i_{dc}(t) = C_{dc}\frac{dv_{dc}(t)}{dt}} \tag{3.58}$$

DC-link current ($\mathrm{i_{dc}(t)}$) consists of both DC component ($\mathrm{I_{dc}}$), and an AC component ($\mathrm{i_{dc,ripple}(t)}$) with double-line frequency. The current DC and AC components are obtained from the equations of (3.59) and (3.60) at balanced power, respectively. The current AC and DC components are calculated in Eq. (3.61) and Eq. (3.62), respectively. The SRF-PLL takes the parallel component of the reference grid current as a grid voltage to match phase angle and frequency between the grid current $\mathrm{i_g(t)}$ and grid voltage. Therefore, Eq. (3.61) is simplified into Eq. (3.63). Then, Eq. (3.63) is simplified as Eq. (3.64) to normalize the parameters of the nominal grid voltage (V_g^n) and nominal DC voltage (V_{dc}^n).

$$v_{dc}(t) i_{dc}(t) = \hat{V}_g \cos(\omega_g t) \hat{I}_g \cos(\omega_g t - \phi) \tag{3.59}$$

$$v_{dc}(t)\, I_{dc} + v_{dc}(t) i_{dc,ripple}(t) = \frac{\hat{V}_g\, \hat{I}_g}{2} \cos(\phi) + \frac{\hat{V}_g\, \hat{I}_g}{2} \cos(2\omega_g t - \phi) \tag{3.60}$$

$$I_{dc} = \frac{\hat{V}_g\, \hat{I}_g}{2\, v_{dc}(t)} \cos(\phi) = \frac{V_g^{rms}\, \hat{I}_g}{\sqrt{2}\, v_{dc}(t)} \cos(\phi) \tag{3.61}$$

$$i_{dc,ripple}(t) = \frac{\hat{V}_g\, \hat{I}_g}{2\, v_{dc}(t)} \cos(2\omega_g t - \phi) \tag{3.62}$$

$$I_{dc} = \frac{V_g^{rms}\, \hat{I}_{g\parallel}}{\sqrt{2}\, v_{dc}(t)} \tag{3.63}$$

$$I_{dc} = \frac{V_g^{n}\, \hat{I}_{g\parallel}}{\sqrt{2}\; V_{dc}^{n}} \tag{3.64}$$

3.7 Summary

In this chapter, inverter and converter topologies are demonstrated with their working principles, circuit diagrams, and mathematical modeling. PV array was modeled under uniform and the PSCs. This chapter also discussed designing an LCL filter in conjunction with a grid-connected inverter topology (VSI). In this chapter, the size of the boost converter's circuit components, inverter, and controllers were calculated based on switching frequency, input, and output voltages. The boost converter's transfer function was mathematically manipulated to check stability and calculate accurate values of the circuit components. In the grid synchronization control, a direct-quadrature (d-q) frame transformation and the SRF-PLL circuit are implemented with their proper control techniques. This chapter also developed three MPPT algorithms in detail with their flow chart diagrams. The differences between the

MPPT methods are presented in detail. It is found that the P&O algorithm is simpler than the INC algorithm. The effects of sampling time and frequency are also discussed, and why a fast sampling time could cause large errors in the PV system. A new coordinated MPPT algorithm is designed to realize the PSCs on solar P-V curves and tests its accuracy and robustness of tracking speed, power oscillations, and convergence speed. The proposed PI-MPPT is found to be simpler to track a GMPP on the shaded P-V curves. This chapter provides a short review of the components of the proposed grid-tied PV system. The synchronous reference phase-locked loop (SRF-PLL) synchronizer is designed to synchronize characteristics waveforms between the VSI and gird. The proportional resonance (PR) controller is modeled to calculate its proportional and resonant gains regulated to remove the SSE of the VSI waveforms and generate two complementary sine pulse width modulation (SPWM) pulses to control four switches of the VSI. The designed characteristics and parameters of this chapter 3 are evaluated and validated in Chapter 4.

CHAPTER 4: SIMULATION AND EXPERIMENTAL RESULTS

4.1 Introduction

In this chapter, the MATLAB SIMULINK model is implemented to test and verify the proposed and conventional algorithms' functionality. The proposed algorithm results are presented under the standard test conditions and compared with the conventional INC and P&O algorithms' response by choosing different step size values of the reference variable. Moreover, the performance of the proposed algorithm is tested at different irradiance profiles. Measurements such as a sampling time, tracking speed, power oscillations, and step size of the proposed algorithm's duty cycle are discussed in detail in this chapter. The simulation and experimental results of the P&O, INC, and proposed MPPT methods are compared under the same testing condition and the PSCs. A comparative study between the algorithms is presented based on the modeling parameters explained in chapter 3. This chapter also presents the simulation and experimental results of the designed system, including the boost converter, a grid-tied H-bridge inverter, and the MPPT controllers. The hardware setup is implemented according to the simulation features. The switching waveforms of the converters are analyzed and compared with the theoretical model. The efficiency of the grid-tied PV system that operates at various power levels is measured, demonstrating high efficiency and the proposed topology's best performance. The tracking efficiency of the MPPT algorithms is calculated by dividing the output tracked power over input PV power.

4.2 Simulation Results

In this chapter, the simulation results from different contingency analyses are presented by investigating different parts of the designed system and verifying the proposed topology in a MATLAB simulation environment. PV module is simulated at STC and three PSCs with multiple power peaks (LMMPs and GMPP) in the first stage.

In the second stage, the proposed system, which consists of the converter, inverter, controllers, MPPTs, and utility grid, is verified using the simulation results. The INC-MPPT, P&O-MPPT, and proposed MPPT are compared to investigate their performance and robustness to interference. Results show that the proposed MPPT system is a more robust and highly efficient PV system technique than the two other MPPT techniques. In this section, a PV module is simulated using the MATLAB SIMULINK based on the PV system design in chapter 3. The solar irradiation patterns are kept similar for the three algorithms. Figure 4.1 shows the MATLAB Simulink model of the proposed system, including the PV panel, boost converter, PI controllers, MPPT algorithms, and grid load. First, simulation results are obtained using the algorithms in the STC at 1000 W/m2 and 25 °C.

The algorithms' performance is tested under a uniform and three types of the PSCs that generate four distinct characteristics of the P-V curves. The values of the circuit components of the boost converter are as follows: $C_1 = 945$ μF, $L_l = 3$ mH and $C_{cdc} = 945$ μF. The values of the components of the LCL filter circuit are as follows: $C_f = 55$ μF, $L_i = 3$ mH, and $L_g = 3$ mH. Sampling time and simulation time for the MPPT controllers are selected as 0.02 s and 1 s, respectively. The switching frequency of the boost converter is chosen to 10 kHz. The step size of the duty cycle in both the conventional algorithms and the proposed algorithm is 0.0001.

4.2.1 P-V and I-V Curves for Uniform and Shading Pattern 1, 2, and 3

In this section, four types of P-V characteristic curves are used to test the designed PV system's performance in a simulation environment generated from uniform weather conditions and shading conditions 1, 2, and 3. Figure 4.1 shows a PV panel's characteristic curves under an acute and three PSCs containing three peaks on each P-V curve. A detailed explanation of the chosen shading patterns and corresponding waveforms is given below.

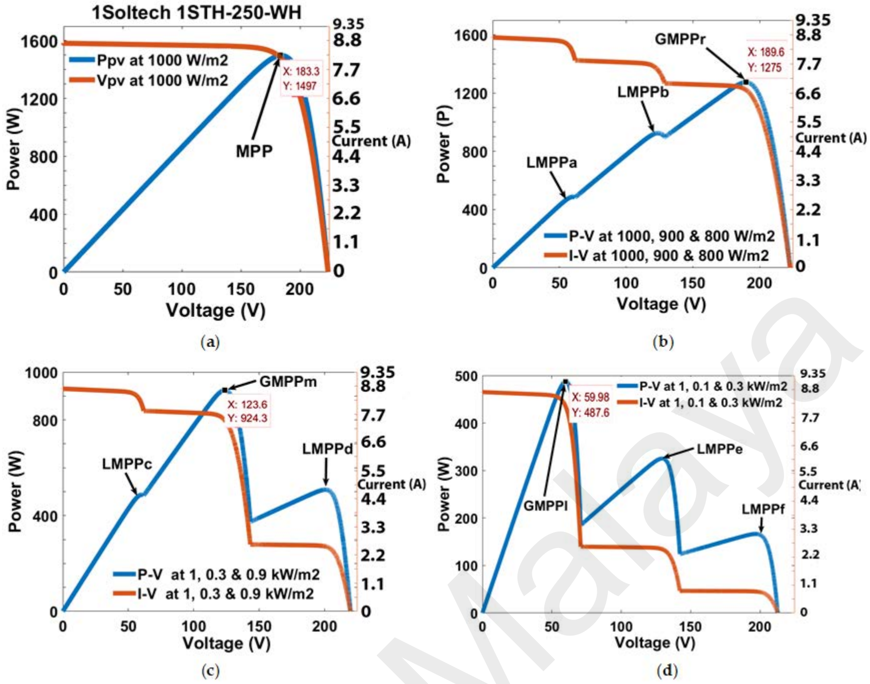

Figure 4. 1: P-V and I-V characteristic curves of the four weather conditions are showed as: (a) uniform weather; (b) shading condition 1; (c) shading condition 2; and (d) shading condition 3.

Figure 4.1 (a) shows the P-V and I-V characteristics curves generated at STC weather conditions (1000 W/m2 and 25 °C). This uniform weather condition generates a single MPP coordinate (183.9 V, 1497 W) on the non-linear P-V curve. Figure 4.1 (b) shows that a P-V curve generates multiple power peaks such as $GMPP_r$ (1.28 V, 0.144 kW), and other two LMPPs ($LMPP_a$ and $LMPP_b$), in which three PV modules; M1, M2, and M3 are exposed to 1000, 900, and 800 W/m2 irradiances. The shading condition 1 is used to check the MPPT algorithms' accuracy together with the designed PV system. Every algorithm tries to track a coordinate of the $GMPP_r$ in which the reference voltage of the algorithm should be closer to MPP voltage (189.5 V) to harness maximum power from the PV array. Figure 4.1 (c) shows that the PV modules (M1, M2, and M3) are responsible for 1, 0.3, and 0.9 kW/m2 solar irradiances, with the GMPPm value being

0.924 kW the P-V curve. The connected bypass diodes and each PV module enable bypassing the maximum current flow generated by non-shaded modules. Therefore, two more local MPPs ($LMPP_c$ and $LMPP_d$) occurred on the P-V curve, producing 487.7 W and 508.6 W powers, respectively. Figure 4.1 (d) demonstrates the P-V and I-V curves at shading condition 3. The PV modules; M_1, M_2, and M_3 are designed to receive 1, 0.2, and 0.4 kW/m2 irradiances, respectively, with an approximate value of $GMPP_l$ being 0.488 kW. Other than the $GMPP_l$, two LMPPs ($LMPP_e$ and $LMPP_f$) occurred on the P-V curve because of an unequal current flow across each PV module. The location of the $GMPP_l$ (487.6 W) is in the left-most side of the P-V curve at shading condition 3, and LMPPs (LMPPe & LMPPf) are in the right and middle of the P-V curve. Power and voltage of the LMPPe are drawn to 325.4 W and 129.4 V while $LMPP_f$ shows 166.5 W and 197 V. Conventional MPPT schemes are inefficient for locating the GMPPs smoothly because multiple local power peaks occurred on the same P-V curve, as shown in Figure 4.1 (b)–(d). A PV system's performance is highly degraded because of the wrong tracking direction of an operating point under the PSCs, mainly when conventional algorithms realize the $GMPP_r$, $GMPP_m$, and $GMPP_l$.

4.2.2 Simulation Results from INC-MPPT

This part investigates the incremental conduction (INC) MPPT algorithm's performance under four weather conditions, such as uniform and three PSCs on the P-V curves.

4.2.2.1 Uniform Weather Condition

Figure 4.2 (a) shows P-V and I-V curves of a PV array under uniform weather condition. Voltage and current values of the I-V and P-V curves are feed by the INC-

MPPT algorithm to generate PV voltage (V_{pv}), current (I_{pv}), power (P_{pv}), and duty cycle (D) as shown in Figure 4.2 (b).

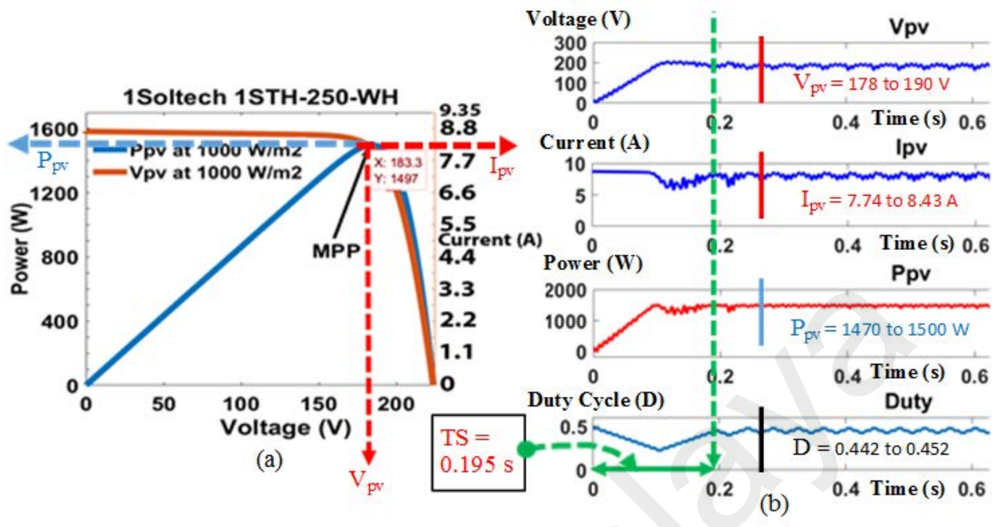

Figure 4. 2: Simulation results of Conventional INC-MPPT are; (a) P-V and I-V curves at STC, and (b) voltage, current, power, and duty cycle graphs

The operating point of the INC-MPPT is taken around 0.195 s (TS) to track the MPP location. During the SSC, the duty cycle is perturbed between 0.442 and 0.452. Consequently, voltage and current fluctuations occurred (178 to 190 V) and (7.74 to 8.43 A), respectively. Power oscillations (1470 to 1500 W) is occurred because of the duty cycle continuously being perturbed with the movement of an operating point nearest to the MPP location even after tracking the MPP earlier. The percentage efficiency (%η) of tracking the MPP by this INC-MPPT algorithm under uniform weather condition is found to be 98.2 %.

4.2.2.2 Shading Condition 1

Figure 4.3 (a) shows P-V, and I-V curves generated from shading condition 1. Figure 4.3 (b) depicts simulation results of PV voltage (V_{pv}), current (I_{pv}), power (P_{pv}), and duty cycle (D) at a partially shaded condition 1. The INC-MPPT algorithm tracks the GMPPr (183.9 V, 1275 W) within 0.205 s, regulating the duty cycle ranged from 0.38 to

0.41. The INC-MPPT algorithm at shading condition 1 generates a range of power, voltage, and current oscillations around the GMPPr, is; (1230 to 1267 W), (185 to 205 V), and (6.2 to 6.9 A), respectively.

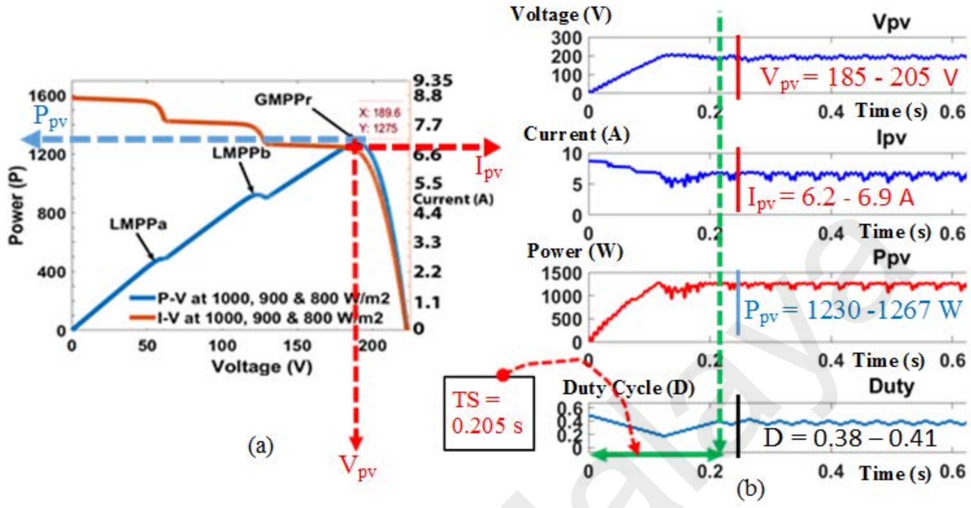

Figure 4. 3: Simulation results of the INC-MPPT are; (a) P-V and I-V curves at shading pattern 1, and (b) voltage, current, power, and duty cycle graphs

The percentage efficiency (%η) of tracking the $GMPP_r$ location is approximately 99.48 % (P_o/P_{mpp}).

4.2.2.3 Shading Condition 2

Figure 4.4 (a) demonstrates P-V and I-V characteristic curves under partial shading condition 2. Figure 4.4 (b) shows voltage (V_{pv}), current (I_{pv}), power (P_{pv}), duty cycle (D) graphs at shading condition 2, in which the maximum power point is denoted as GMPPm. In this case, the INC-MPPT algorithm's operating point goes back and forth along the P-V curve and moves between the GMPPm and $LMPP_d$ instead of maintaining its position at the GMPPm location. The algorithm's duty cycle is ranged from 0.5 to 0.52 to drive the operating point toward $GMPP_m$ location. As a result, large amounts of voltage, current, and power oscillations are measured around the $GMPP_m$. The PV voltage, current, and power oscillations are ranged from; (120 to 131 V), (6.5 to

6.77 A), and (850 to 925 W) respectively. The INC algorithm's tracking efficiency is degraded by 36.74%, which means only 63.26% is the algorithm's estimated chance to track an LMPP location instead of the $GMPP_m$ at shading condition 2. The operating point of the INC-MPPT algorithm reached at $LMPP_d$ approximately within 0.21 s.

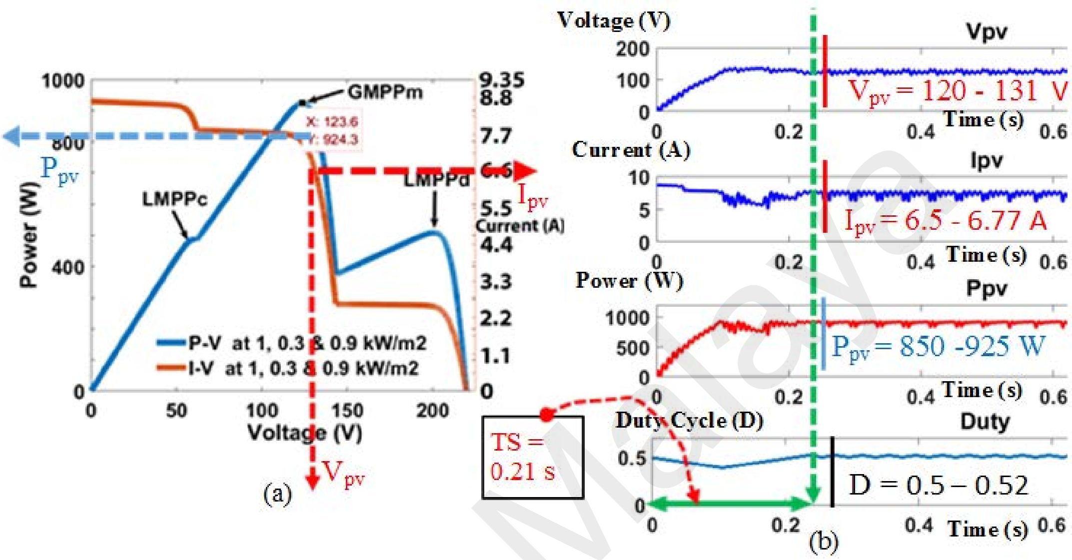

Figure 4. 4: Simulation results of the INC-MPPT are; (a) P-V and I-V curves at shading condition 2, and (b) voltage, current, power, and duty cycle graphs

4.2.2.4 Shading Condition 3

Figure 4.5 (b) shows the simulation results of the conventional INC-MPPT for shading condition 3 (left-sided GMPP location). The INC-MPPT algorithm cannot track $GMPP_l$ at shading condition 3, which causes power (P_{pv}) fluctuations from 294 to 325 W at steady-state condition; instead, an operating point is stuck at $LMPP_e$. Voltage (V_{pv}) and current (I_{pv}) fluctuations are found from; 122.5 to 132.4 V and 2.2 to 2.6 A, respectively. The duty value of the converter is regulated from 0.18 to 0.32 during these dynamic environmental conditions. The INC-MPPT took approximately 0.39 s to track the $LMPP_e$ and reach the SSC. In this stage, the INC-MPPT is unable to trace an actual path of the $GMPP_l$ because its operating point gets confused among multiple power peaks on the P-V curve. Therefore, tracking performance of this algorithm is only 75.3% at shading condition 3.

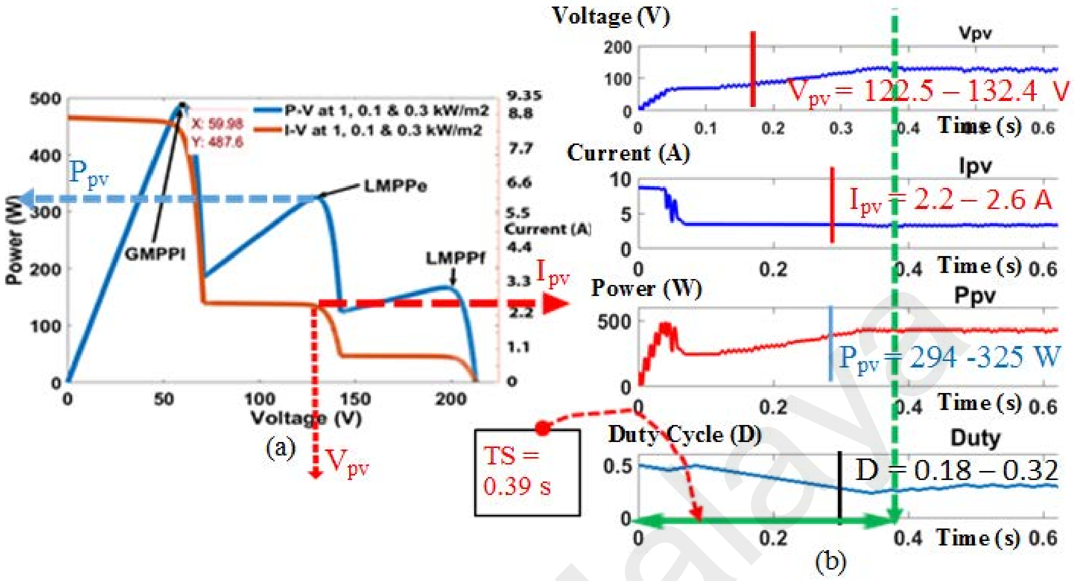

Figure 4. 5: Simulation results of the INC-MPPT are; (a) P-V and I-V curves at shading pattern 3, and (b) voltage, current, power, and duty cycle graphs

4.2.3 Simulation Results for P&O-MPPT Algorithm

Simulation work is carried out to evaluate the performance of the P&O algorithm at four different environmental conditions as follows;

4.2.3.1 Uniform Weather Condition

Figure 4.6 (a) shows P-V and I-V curves of the PV array under a uniform weather condition. Figure 4.6 (b) illustrates the simulated graphs of the voltage (V_{pv}), power (P_{pv}), current (I_{pv}), and duty cycle (D) of a conventional P&O-MPPT algorithm under uniform insolation condition. The P&O algorithm has taken around 0.21 s to track an MPP. Power, voltage, and current oscillations around the MPP are measured as; 1473 to 1500 W, 166 to 193 V, and 7.8 to 8.5 A, respectively. Massive power oscillation indicates an operating point's movement, and perturbation size of the duty cycle is unstable at the SSC. The duty cycle perturbation is ranged from 0.44 to 0.46 during the MPP tracking time.

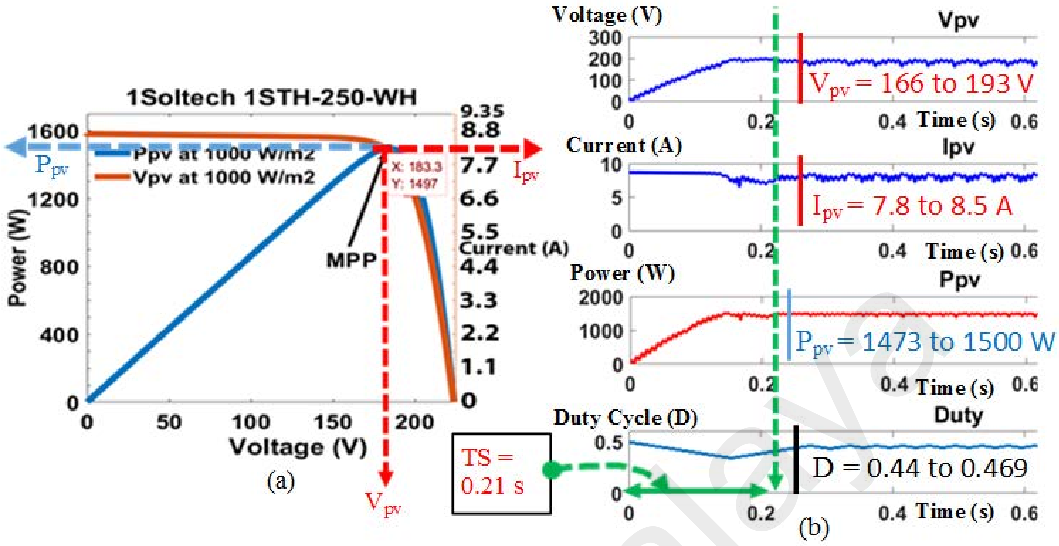

Figure 4. 6: Simulation results of the P&O-MPPT are; (a) P-V and I-V curves at STC, and (b) voltage, current, power, and duty cycle graphs

4.2.3.2 Shading Condition 1

Figure 4.7 (a) & (b) show P-V and I-V curves that are feed by the P&O-MPPT algorithm to generate a voltage (V_{pv}), current (I_{pv}), power (P_{pv}), and duty cycle (D) as shown in Figure 4.7 (b).

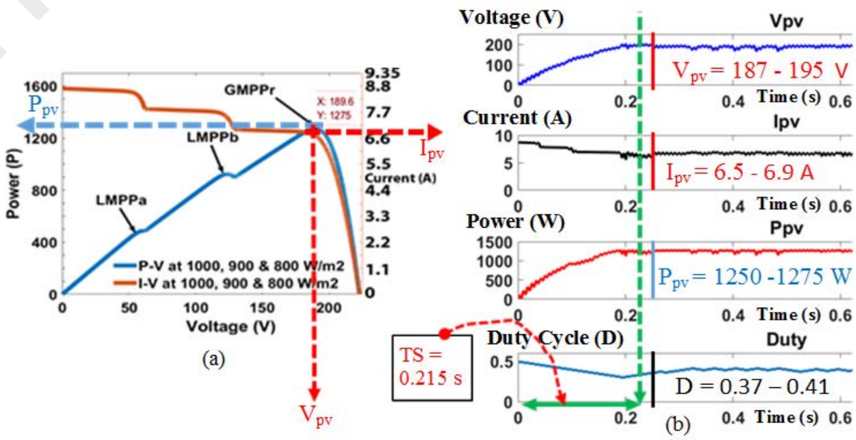

Figure 4. 7: Simulation results of the P&O-MPPT are; (a) P-V and I-V curves at shading condition 1, and (b) voltage, current, power, and duty cycle graphs

At this partially shaded condition 1, the operating point of the P&O-MPPT algorithm moves around the GMPPm location, causing a substantial amount of power oscillation (1250 to 1275 W). The P&O algorithm degrades the overall efficiency of MPP tracking performance (99.66%). Voltage, current, and duty cycle perturbation values are measured from 187 to 195 V, 6.5 to 6.9 A, and 0.37 to 0.41. The tracking speed of the algorithm is measured around 0.215 s.

4.2.3.3 Shading Condition 2

Figure 4.8 shows the simulation result of the P&O-MPPT technique under shading condition 2. This algorithm's operating point moves between the $GMPP_m$ and $LMPP_d$, which takes around 0.22 s to reach the $LMPP_d$. An amount of power (P_{pv}) oscillation (264 W) is measured on the P-V curve. Similarly, voltage (V_{pv}) and current (I_{pv}) fluctuations are measured to be 24.2 V and 2.38 A, respectively. In the steady-state condition, the duty cycle range is found from 0.49 to 0.52. As a result, the efficiency of tracking the $LMPP_d$ is found to be around 63.46 %.

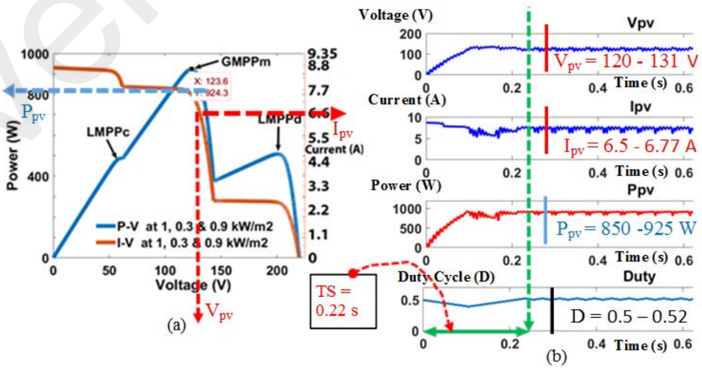

Figure 4. 8: Simulation results of the P&O-MPPT are; (a) P-V and I-V curves at shading condition 2, and (b) voltage, current, power, and duty cycle graphs

4.2.3.4 Shading Condition 3

Figure 4.9 shows the simulation results of the P&O-MPPT algorithm at shading condition 3. In this case, the P&O-MPPT's operating point solely tracks $LMPP_e$ instead of the GMPP$_l$ on the shaded P-V curve shown in Figure 4.9 (a). Figure 4.9 (b) represents voltage (Vpv), current (I_{pv}), power (P_{pv}), and duty cycle (D) graphs that are generated from the values of the P-V and I-V curves through the P&O-MPPT algorithm. The operating point of the P&O-MPPT needs a minimum of 0.315 s to reach even the LMPP$_e$. After wrongly tracking the LMPP$_e$, the PV module's power (P_{pv}) fluctuates between 294 and 326 W at the SSC. The duty cycle of the converter at the SSC varies from 0.44 and 0.46. The tracking efficiency of the P&O-MPPT is approximately 76.8% as the operating point is stuck at LMPP$_e$, resulting in massive power loss.

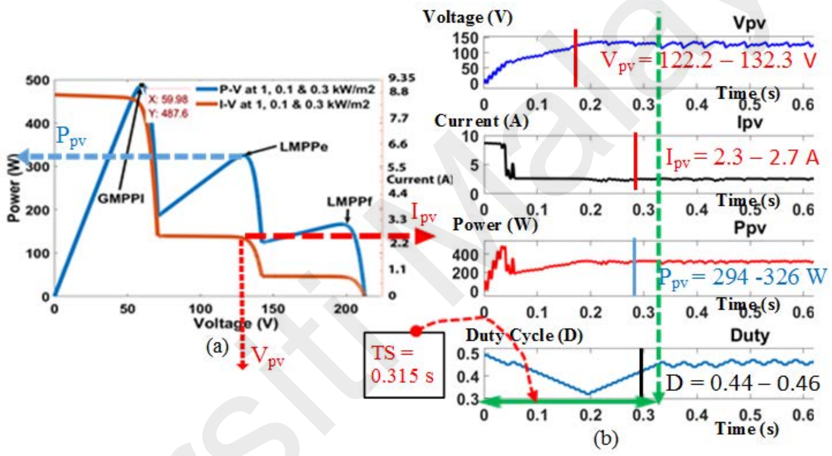

Figure 4. 9: Simulation results of the P&O-MPPT are; (a) P-V and I-V curves at shading condition 2, and (b) voltage, current, power, and duty cycle graphs

4.2.4 Simulation Results for proposed PI-MPPT Algorithm

This section includes different contingency analysis of the proposed MPPT algorithm to investigate its reliability and robustness against disturbances and partially shaded conditions. Four types of results are outlined as follows;

4.2.4.1 Uniform Weather condition

Figure 4.10 (a) shows P-V and I-V curves that are passed through the proposed MPPT algorithm to track MPP voltage (V_{mpp}), current (I_{mpp}), and power (P_{mpp} = 1497 W). Figure 4.10 (b) shows the proposed algorithm tracks an MPP location with a tracking efficiency of 99.99 % (1496.85/1497 * 100). The duty cycle (D) of the boost converter remains constant by 0.4745 around the MPP location after several iterations at the SSC on the P-V curve. The proposed algorithm achieves a tracking speed of 0.19 s to reach the MPP. After tracking the MPP, no power (P_{pv}), voltage (V_{pv}), and current (I_{pv}) oscillations remain at the SSC shown in Figure 4.10 (b).

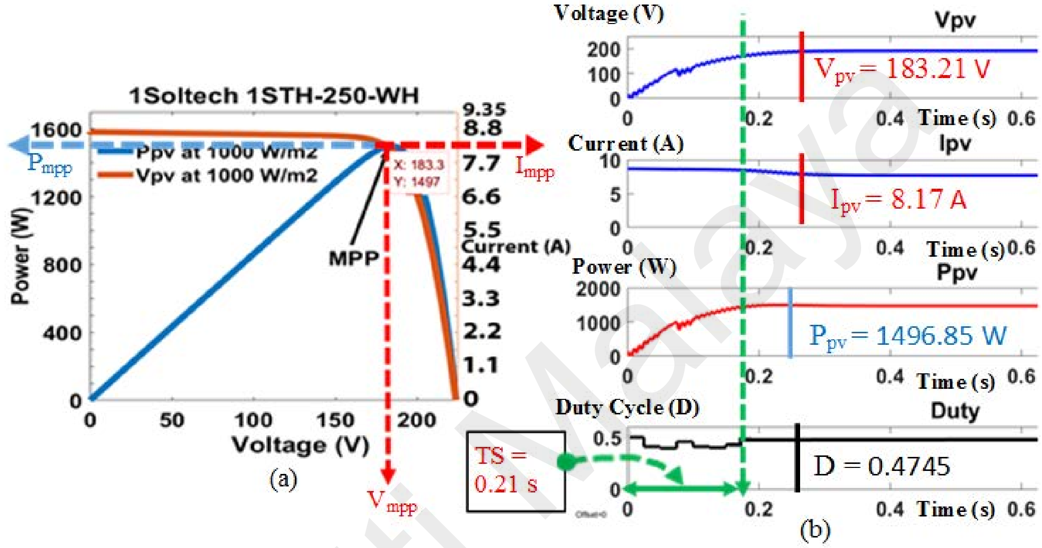

Figure 4. 10: Simulation results of the Proposed MPPT are; (a) P-V and I-V curves at STC, and (b) voltage, current, power, and duty cycle graphs

4.2.4.2 Shading Condition 1

Figure 4.11 shows the simulation results of shading condition 1 and PV characteristics graphs. The $GMPP_r$ is located on the right of the P-V curve. With the operating point movement toward $GMPP_r$, the duty cycle (D) perturbation is followed by a sequence (0.5, 0.45, 0.43, and 0.4745), and constant D (0.458) occurs when the $GMPP_r$ is tracked as shown in the black colored line graph of Figure 4.11 (b). Proposed algorithm tracks the $GMPP_r$ at PV power (P_{pv} = 1274.1 W), voltage (V_{pv} = 189.59 V) and current (I_{pv} = 6.72 A), which are resemble to the power (P_{GMPPr} = 1275 W), voltage (V_{GMPPr} = 189.6 V) and current (I_{GMPPr} = 6.724 A) as shown Figure 4.11 (b), and (a), respectively. As a result, the proposed algorithm achieves the tracking efficiency (%η) and tracking speed (TS) of 99.93 % (P_{pv} /P_{GMPPr} * 100) and 0.13 s, respectively.

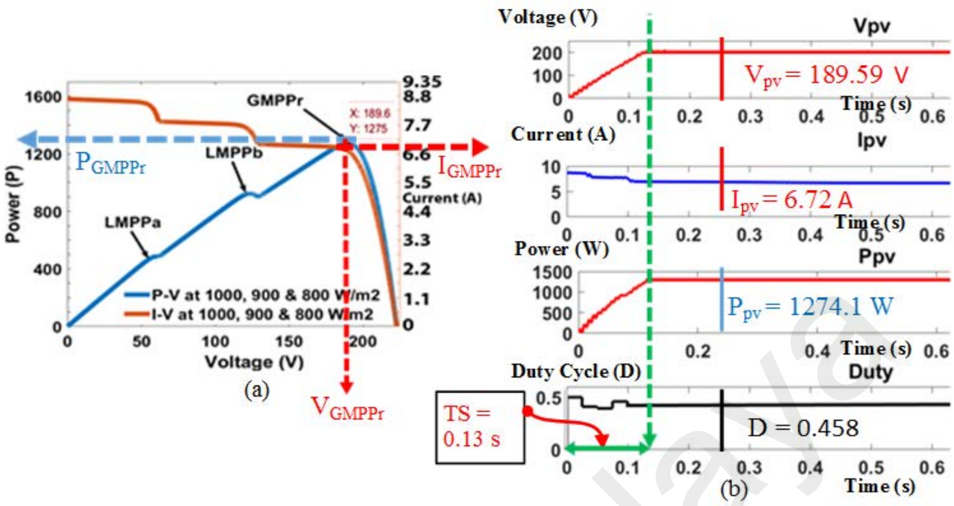

Figure 4. 11: Simulation results of the Proposed MPPT are; (a) P-V and I-V curves at shading condition 1, and (b) voltage, current, power, and duty cycle graphs

4.2.4.3 Shading Condition 2

Figure 4.12 (a) and (b) show P-V and I-V curves and line graphs of PV power (P_{pv}), voltage (V_{pv}), current (I_{pv}), and duty cycle (D) under the shading condition 2.

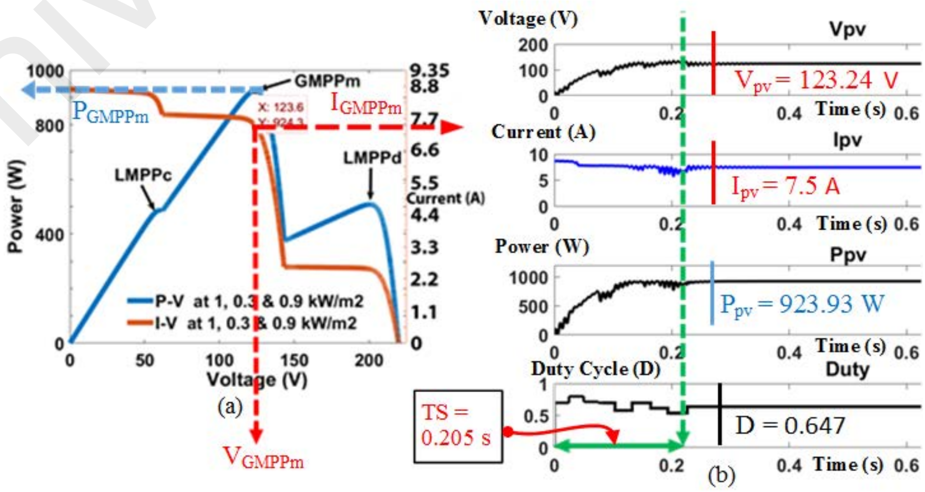

Figure 4. 12: Simulation results of the Proposed-MPPT are; (a) P-V and I-V curves at shading condition 2, and (b) voltage, current, power, and duty cycle graphs

The proposed algorithm tracks the GMPPm at PV power (P_{pv} = 923.93 W), voltage (V_{pv} = 123.24 V) and current (I_{pv} = 7.5 A), which are equivalent to the the power (P_{GMPPm} = 924.3 W), voltage (V_{GMPPm} = 123.6 V), and current (I_{GMPPm} = 6.724 A) as shown Figure 4.12 (b), and (a), respectively. As a result, the proposed algorithm achieves the tracking efficiency (%η) and tracking speed (TS) that are 99.93 % (P_{pv} /P_{GMPPm} * 100) and 0.205 s, respectively.

4.2.4.4 Shading Condition 3

Figure 4.13 (a) and (b) show P-V and I-V curves and line graphs of PV power (Ppv), voltage (Vpv), current (Ipv), and duty cycle (D) under the shading condition 3.

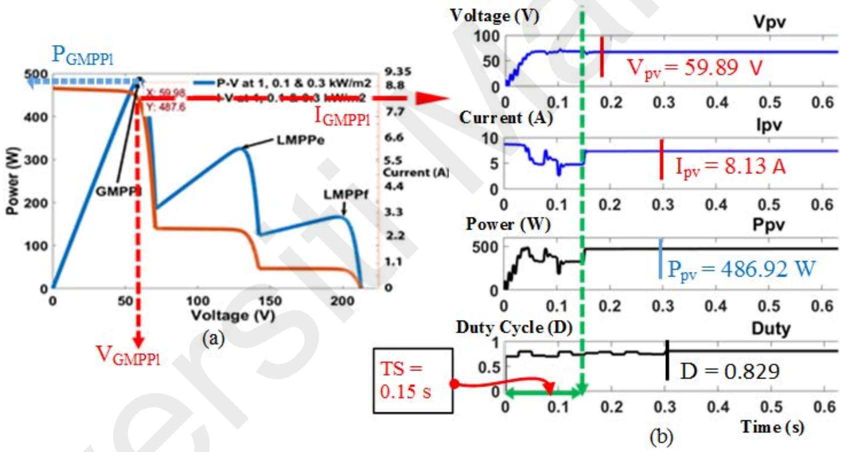

Figure 4. 13: Simulation results of the Proposed-MPPT are; (a) P-V and I-V curves at shading condition 3, and (b) voltage, current, power, and duty cycle graphs.

The proposed algorithm tracks the GMPPl at PV power (P_{pv} = 486.92 W), voltage (V_{pv} = 59.89 V) and current (I_{pv} = 8.13 A), which are equivalent to the the power (P_{GMPPl} = 487.6 W), voltage (V_{GMPPl} = 59.98 V), and current (I_{GMPPl} = 8.129 A) as shown Figure 4.13 (b), and (a), respectively. As a result, the proposed algorithm achieves the tracking efficiency (%η) and tracking speed (TS) of 99.86 % (P_{pv} /P_{GMPPl} * 100) and 0.15 s, respectively.

4.2.5 Comparative Study

This section includes a comparative study between the three MPPT algorithms' obtained results under acute weather and the PSCs. In the INC, P&O, and proposed MPPTs, there is no much difference in tracking an MPP location under a uniform weate condition. Even at shading condition 1, the three algorithms can track a GMPP with a little difference of power oscillations and tracking accuracy. But, conventional INC and P&O are not prone to use under shading conditions 2 and 3 because of having massive power oscillation at the location of a GMPP or LMPP. Hence, this comparative study helps to identify the proposed MPPT as a reliable technique in this research work.

4.2.5.1 Uniform Weather condition

Figure 4.14 (a) shows P-V and I-V characteristics curves under a uniform weather conditon. Figure 4.14 (b) shows the simulation of power graphs for conventional INC, P&O, and proposed algorithms under uniform solar insolation on a PV array. In this weather condition, the PV array's MPP is located at 1497 W power on the P-V curve. Power oscillations considered in both INC and P&O algorithms are much higher than the proposed MPPT scheme (zero oscillation). Power fluctuation in conventional algorithms during the SCC is around 30 W (1500-1470) and 27 W (1500-1473), whereas no considerable power loss is found in the proposed MPPT. The MPP tracking capability percentage (%η) is 98.2 %, 98.3%, and 99.99 % in the INC, P&O, and proposed algorithms. Hence, the proposed algorithm is superior to the other two MPPT methods in terms of tracking performance.

Similarly, no oscillation occurred in the current and voltage graphs while running the proposed algorithm in the uniform weather condition, as demonstrated in Figure 4.14 (c) & (d). The Proposed PI-MPPT achieved 0.005 and 0.02 seconds faster-tracking speed than the conventional INC and P&O-MPPT techniques. Hence, similar characteristics of the three MPPT algorithms are observed in terms of tracking speed. Figure 4.14 (e) shows how the step change of the duty cycle happens during the simulation time (from 0 to 0.5 s). A decreasing and increasing trend of the duty cycle occurs until around 0.2 s of the simulation time in the INC, P&O, and the proposed techniques. However, the proposed MPPT algorithm stops the interations of the duty cycle after passing transient time (0.19 s) and tracks GMPP, whereas other algorithms continue the perturbation to the next level.

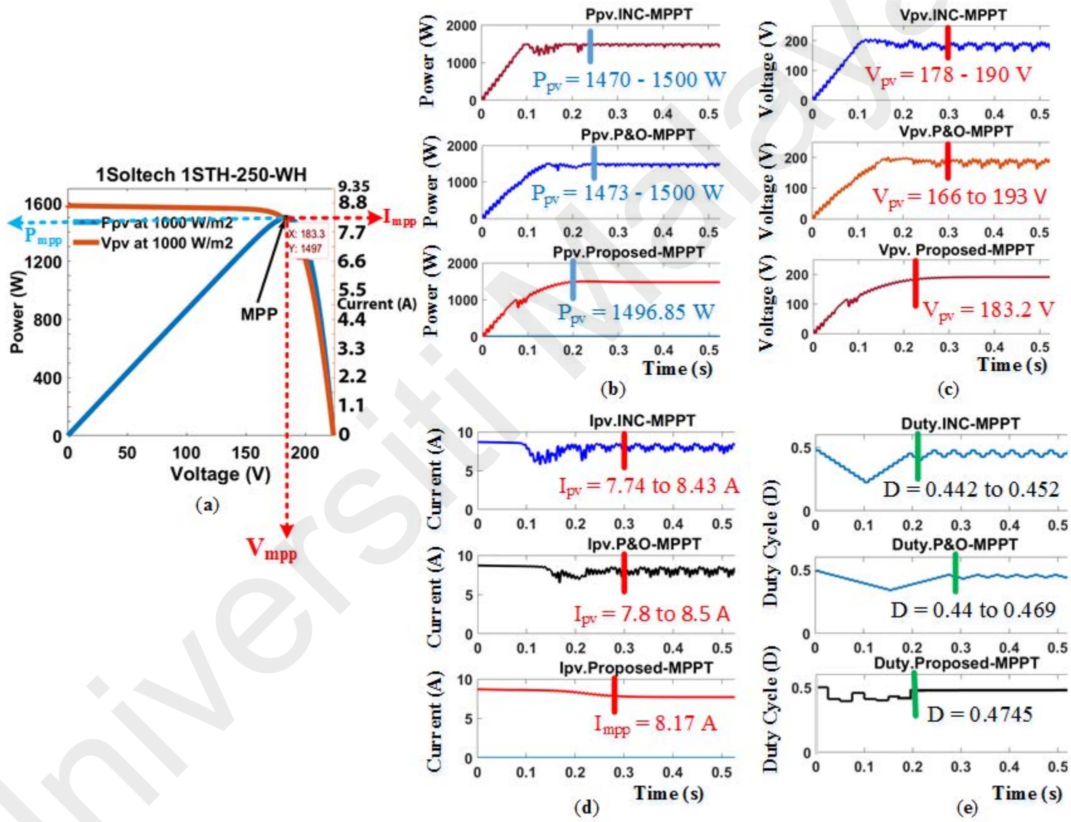

Figure 4. 14: Comparative simulation results of INC, P&O, and Proposed algorithms at STC are listed as (a) STC waveforms; (b) power; (c) voltage (d); current; and (e) duty cycle waveforms.

4.2.5.2 Shading Condition 1

Figure 4.15 shows the comparative analyses of powers, voltages, currents, and duty cycles between the MPPT methods. These waveforms are drawn from the shading condition 1, in which the $GMPP_r$ location is on the right side of the P-V curve. The proposed technique tracks the $GMPP_r$ because its searching process enables high rapid convergence of the operating point toward GMPP. The duty cycle (0.458) also converges to the best location of the GMPP in the proposed algorithm. In contrast, the conventional MPPT schemes cannot remove the fluctuation of the duty cycle values even after tracing the GMPPr locus's path. Power fluctuations at the SSC in both INC and P&O MPPT algorithms are 37 and 25 W, respectively, compared with the zero power loss in the proposed MPPT technique, as shown in Figure 4.15 (b).

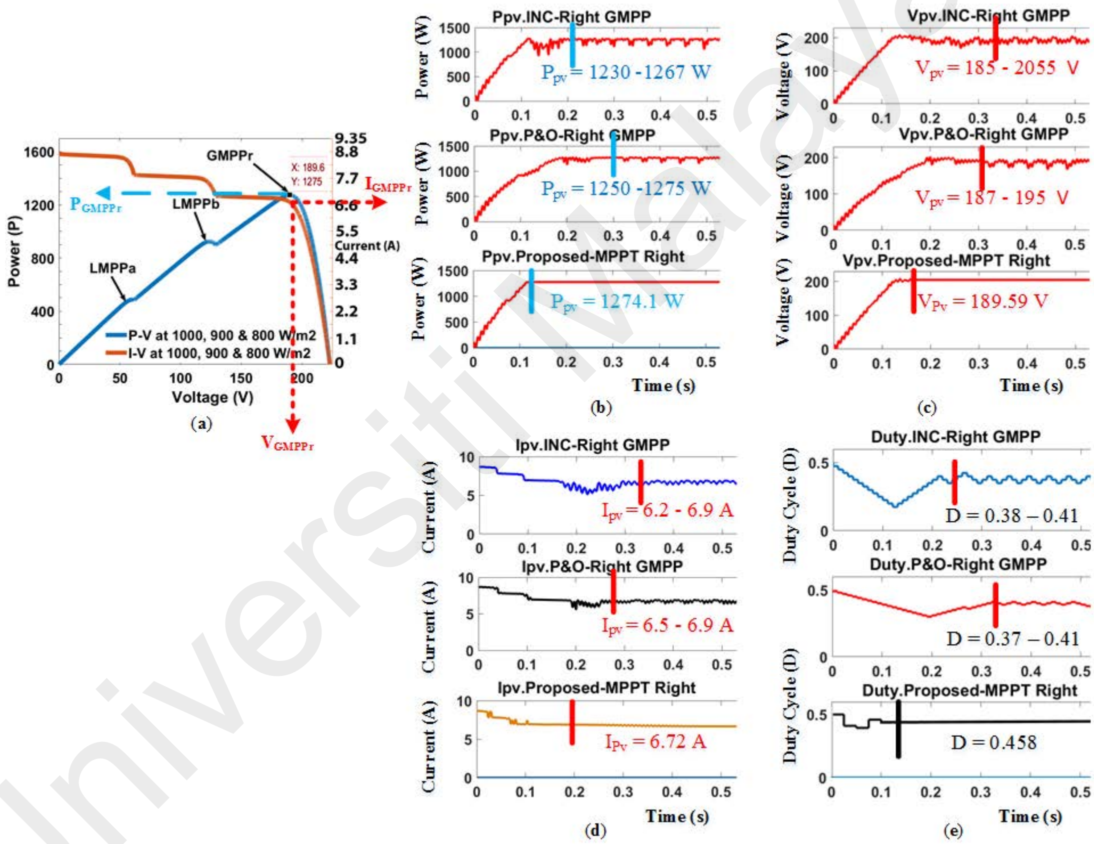

Figure 4. 15: Comparative Simulation results of INC, P&O, and proposed MPPTs at shading condition 1 are listed as (a) P-V and I-V curves; (b) power; (c) voltage; (d) current; and (e) duty cycle.

The proposed technique needs less than 0.075 and 0.085 seconds from INC and P&O MPPT algorithms to track the GMPP. Nevertheless, the proposed MPPT system's accuracy improved because no noticeable perturbation was observed in the duty cycle at the GMPP location. The proposed method achieved 0.45% and 0.27% tracking efficiencies higher than those of the INC and P&O MPPT techniques, respectively.

4.2.5.3 Shading Condition 2

Figure 4.16 (b) demonstrates a PV array's power graphs at shading pattern 2 (middle GMPP case). Power oscillations approximately 100 and 84 W more are measured in the conventional INC and P&O MPPTs than in the proposed MPPT technique.

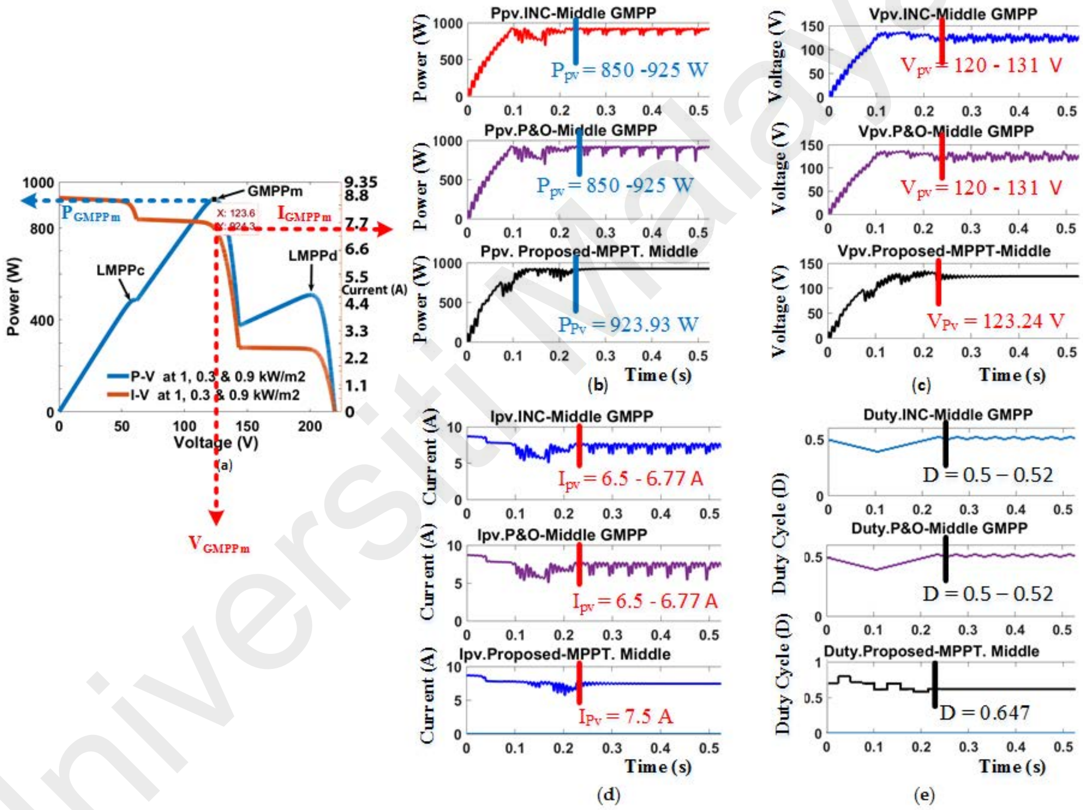

Figure 4. 16: Comparative Simulation results of INC, P&O, and proposed MPPTs at shading condition 2 are listed as (a) P-V and I-V curves; (b) power; (c) voltage; (d) current; and (e) duty cycle.

The conventional MPPT algorithms are stuck at one of the local MPPs instead of tacking a GMPP location on the P-V curve, resulting in massive power loss. Therefore, the proposed algorithm's tracking accuracy is higher than that of the traditional algorithms by 36.7% and 36.5%, respectively. Similarly, a substantial number of oscillations are drawn in the conventional techniques on their voltage and current graphs; (20.5 V and 1.5 A) associated with INC, and (15.6 V and 1.54 A) with P&O, as shown in Figures 4.16 (b) and (c). Moreover, the proposed technique's tracking speed (0.205 s) is faster than those of the conventional ones (0.21 and 0.22 s), as the operating point converges the duty cycle rapidly toward the GMPP. The proposed algorithm requires only a few duty cycle perturbations to reach the GMPP, resulting in substantial improvements in tracking speed and convergence time. Figure 12 (e) shows the graphs of the duty cycle perturbation for different algorithms. The GMPP location's duty cycle is calculated as 0.647, which is satisfied by the proposed technique for shading condition 2. However, a fluctuation of 0.02 in the duty cycle step size is found in the conventional MPPT algorithms. In contrast, the constant duty cycle is operated in the proposed scheme at steady-state conditions (SSC).

4.2.5.4 Shading Condition 3

Figure 4.17 (b)-(e) shows a comparative study of PV graphs of the INC, P&O, and coordinated PI-MPPT algorithms. Oscillations in power, voltage, and current are measured to the SSC. In the proposed MPPT technique, no power oscillation is found at the SSC, whereas the conventional algorithms show extensive power losses even after tracking an $LMPP_e$ location. Power oscillations in the conventional INC and P&O MPPTs are exposed at 31 and 22 W, respectively. An operating point of the proposed MPPT method remains on the $GMPP_l$ location at 0.829 duty cycle of the boost converter after perturbing 0.64, 0.78, and 0.829 consecutively. Consequently, the proposed algorithm's tracking performance is much higher than that of the conventional techniques by 24.56% and 23.06%, respectively. Hence, the proposed PI-MPPT achieved 99.86% power efficiency. The tracking speed (TS) in INC, P&O, and proposed algorithms are calculated by 0.39, 0.315, and 0.15 s, respectively. Hence, the proposed algorithm can track GMPP almost two times higher than the traditional MPPT schemes at the shading condition 3.

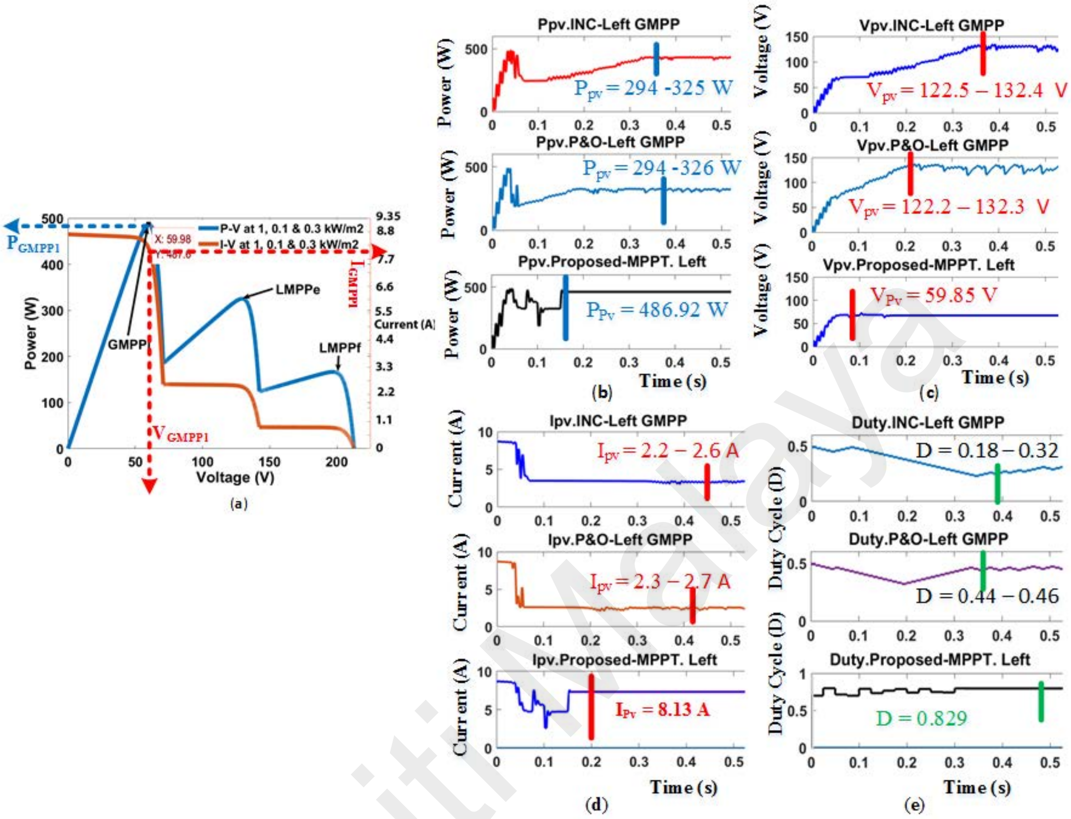

Figure 4. 17: Simulation results of INC, P&O, and proposed MPPTs at shading condition 3. are listed as (a) P-V and I-V curves; (b) power; (c) voltage; (d) current; and (e) duty cycle characteristics.

4.2.5.5 Performance of H-Bridge VSI

The H-bridge VSI is controlled by a PLL, PR, SPWM pulses, and PI controller to produce a constant grid voltage and frequency (250 V and 50 Hz, respectively). Figure 4.18 (a) shows the steady-state response of the grid voltage (V_g = 249.5 V) and current (I_g = 10.48 A) waveforms of the VSI when the proposed MPPT algorithm is operating at the MPP (1497) location on the P-V curve under uniform weather condition. Note that the waveforms are in phase, and no ripple components appeared to them. Figure 4.18 (b) illustrates the current and voltage waveforms of the VSI that injects active power to the utility grid at unity power factor under shading condition 1. The peak value of the current injected into the grid decreases, maintaining the same phase and unity power factor. Thus, ripple-less grid voltage and current are measured to be 251 V and 7.2 A, respectively. Figure 4.18 (c) depicts the grid voltage and current waveforms at shading condition 2, synchronized with the grid phase and frequency. The PR controller eliminates a control system on the grid-side tracks the sinusoidal grid voltage and current signals with a fundamental frequency of 50 Hz and the SSE. Figure 4.18 (d) illustrates the grid's voltage and current waveforms with an accurate demonstration of their phase and frequency synchronization with the VSI. The voltage and current are 250.2 V and 3.1 A, respectively, when the VSI is operated under shading condition 3.

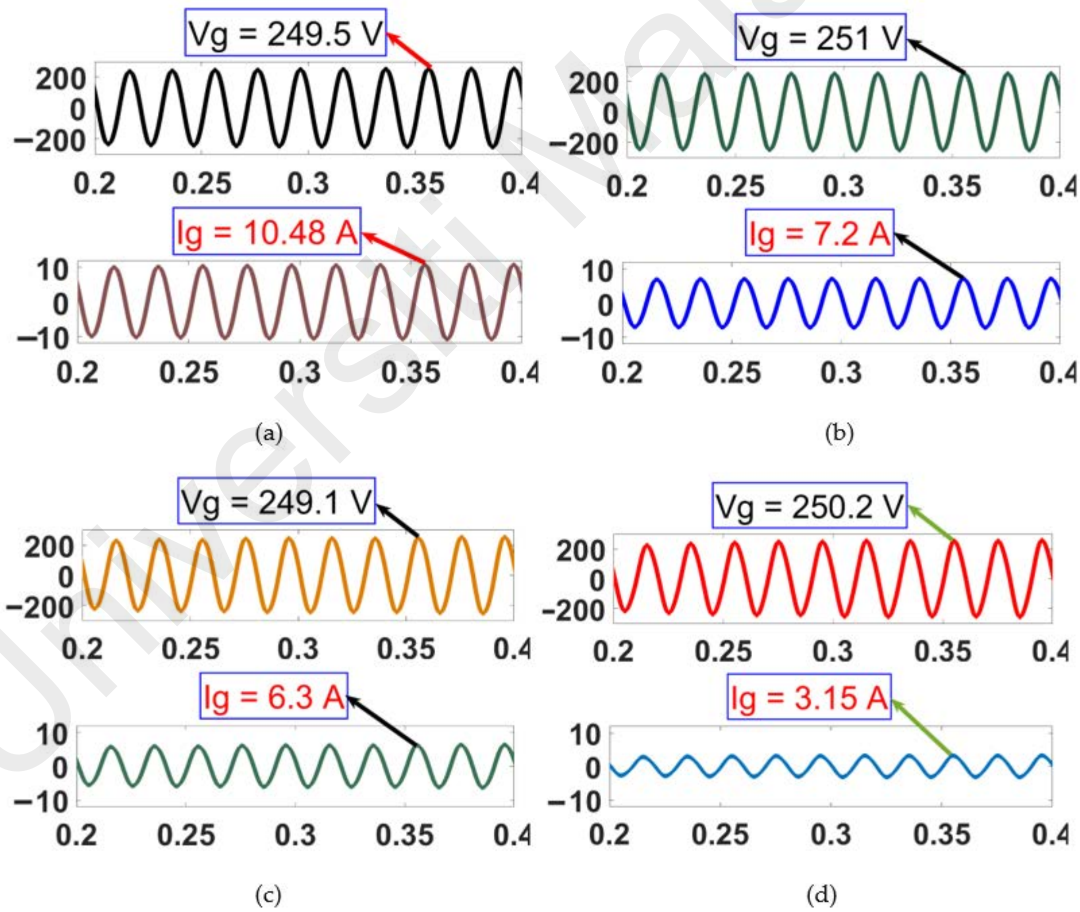

Figure 4. 18: Simulation results of the proposed VSI: (a) uniform weather; (b) shading pattern 1; (c) shading pattern 2; and (d) shading pattern 3.

4.3 Experimental Validation

Experimental work was conducted o validate the model design analysis for four solar insolation profiles and shading patterns. The proposed topology is run with experimental works to investigate the conventional and proposed MPPT algorithms' performance. To analyze the tracking speed, convergence time, and power oscillations against the shading conditions 1, 2, and 3, a series-connected PV module (Model Atlantis Energy Systems SS125LM) was used to build the PV array in both the solar array simulator (SAS) and table modes of Agilent solar simulator. A low-power (213.33 W at STC) PV module was chosen because of a limitation in the simulator's power configuration. A dSPACE board, MATLAB software, and the solar simulator are interfaced with the proposed topology to generate PWM and sine PWM (SPWM) signals in controlling converter and inverter switches at 10 kHz frequency. The dSPACE controller was also used to sense current and voltage from the boost converter through the analog-to-digital (ADC) converter ports, triggering the waveforms.

4.3.1 Experimental Setup

Figure 4.19 shows a scaled-down prototype of an experimental setup comprising a digital oscilloscope (LeCroy), DC power supply units, DC-DC boost converter, DSP dSPACE board, gate drives, sensors, filter circuits, solar simulator interface, and load. The hardware schematic and design parameters were analyzed through the experimental setup under uniform and shaded conditions. These results were then compared with PI-P&O and PI-INC algorithms. The conventional and proposed MPPT schemes were evaluated for shading pattern 1 (five modules per string in each series-connected panel at 1, 0.8, and 0.6 kW/m2), pattern 2 (five modules per string in each series-connected panel at 1, 0.5, and 0.2 kW/m2), and pattern 3 (five modules per string in each series-connected panel at 1, 0.1 and 0.3 kW/m2). A modular SAS (E4360A, Agilent

Technologies) was used to obtain different levels of solar irradiance curves (uniform and partial shading patterns). Initially, uniform and partially shaded PV curves were transformed into comma-delimited value (CSV) files in a MATLAB Simulink environment. These CSV files comprised P-V and I-V curve values, which generated MPPs and GMPPs at the uniform, right, middle, and left sides of the waveforms. The files were uploaded and implemented in the solar simulator interfaced with a laptop to display the graphical user interface (GUI) on the screen.

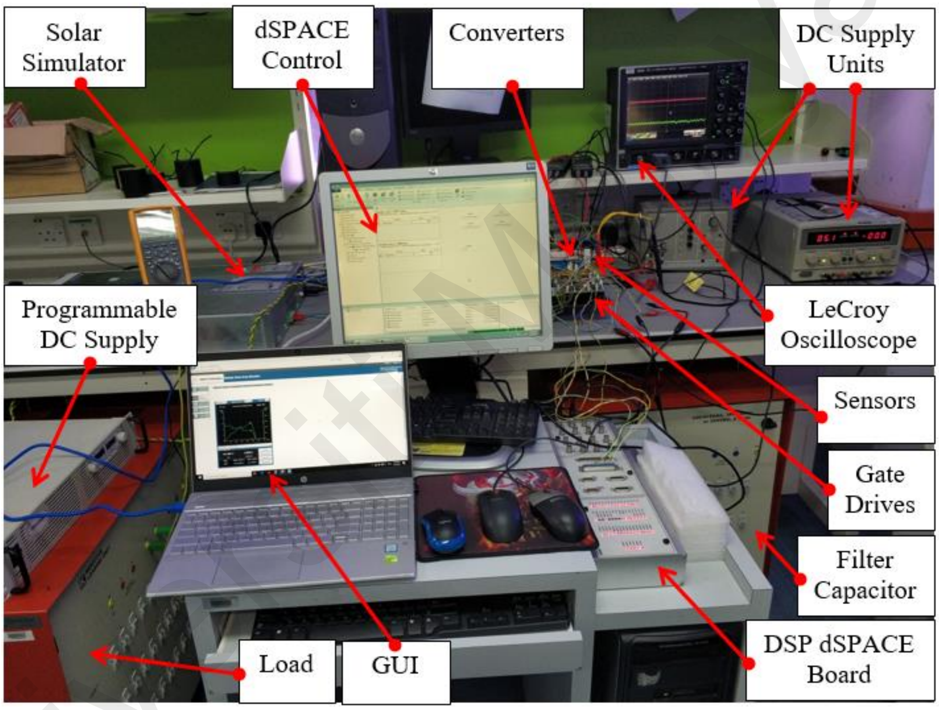

Figure 4. 19: Experimental Setup

Keysight Connection Expert 2018 software and Web User Interface (WUI) were used to selecting and running the partial shading patterns and designed modules to operate the simulator. The solar simulator supplies different power schemes produced from the partially shaded PV array to the boost converter's input side. Sensors (LV-25P and LA-25NP) were used as the transducers in this experimental analysis to sense the current and voltage from the PV output curves. The dSPACE hardware board reads the voltage and current sensors' values to implement MPPT algorithms with a proper selection of gain parameters. The input of the boost converter is connected to the output of the current and voltage sensors. Then, the boost converter's output is connected with the H-bridge inverter's input to generate AC signals fed by the load. The same sampling time (0.02) is used in both simulation and experimental analyses to measure PV current and voltage with MATLAB and Lecry oscilloscope, respectively.

4.3.2 PWM and SPWMs Generation in dSPACE Platform

dSPACE DS1104 board is used to control the boost converter and the VSI by interfacing the MATLAB Simulink model in a real-time hardware design. In the MATLAB Simulation model, dSPACE input-output (I/O) blocks such as DS1104ADC and DS1104DAC are introduced. An automatic generation of C-code is transformed from the simulation model because of using real-time-workshop (RTW). Graphical user interface (GUI) with dSPACE Control Desk is used in real-time to display and monitor parameters such as voltage and current of the converters.

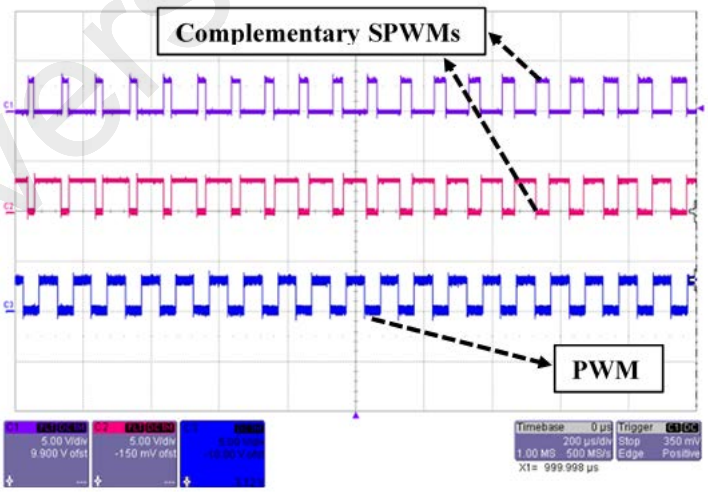

Figure 4. 20: PWM and SPWM Pulses in dSPACE Platform

The control desk is interfaced with the MATLAB Simulink model and real-time interface (RTI) library (to generate control signals and build a Simulink model). After reading and scaling down the analog values of the voltage and current measured from the sensors, the DS1104 board feeds them in a workable level and sends them to the analog to digital converter (ADC) channels with the proper sampling process. These analog signals are fed by the PWM and SPWM generators to produce switching pulses for the inverter and converter, as shown in Figure 4.20. The switches' duty cycle is modulated with the inverter control signal (reference output voltage) to operate the switches (MOSFETs) of the FB-VSI. Gate drive circuits are used between the dSPACE board and the converters to receive the ADC channels' generated signals. PWM blocks (DS1104SL_DSP_PWM and DS1104SL_DSP_PWM1) have four PWM channels. A constant block is used to the input port of the PWM block to generate duty cycle pulses. Then, a constant reference value of the duty cycle is defined into the constant block. The switching frequency is set to 10 kHz into the PWM block with dead-band values. The PWM pulses' output voltage is from 4 to 5 V obtained from the slave I/O connector pins (5, 7, and 9). Gate drivers are used to boosting the PWM and SPWM voltage levels between 13 and 16 V to smoothly control the switches of the VSI.

4.3.3 Boost converter and VSI Tests

Figure 4.21 shows the results of the boost converter and the VSI at a constant duty cycle operation (0.714).

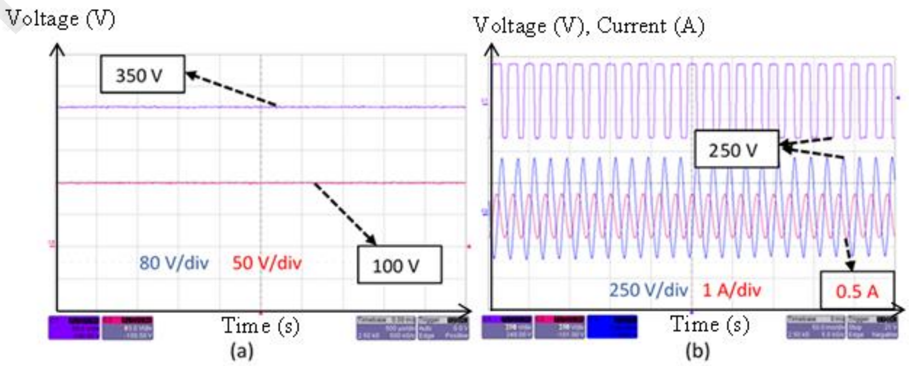

Figure 4. 21: boost converter and the VSI results: (a) input and output voltages of boost converter; (b) output square and sinusoidal voltage waveforms, and current waveforms VSI.

Figure 4.21 (a) shows the boost converter boots up from 100 V (input DC voltage) to 350 V (output DC voltage). Input and output DC currents of the boost converter are to be 4.51 and 1.3 A, respectively. The VSI control system is designed to generate the output voltage of 250 V sinusoidal waveform for 350-400 V input DC-link voltage as shown in Figure 4.21 (b). In the VSI, the output square wave is found to be 3-levels (+V, 0, and −V) with no ripple components because of operating its switches by accurate complementary SPWM pulses.

4.3.4 P-V and I-V Curves for Uniform and Shading Patterns 1, 2, and 3

Figure 4.22 shows a PV panel's characteristic curves under uniform weather and the PSCs containing multiple peaks on each P-V curve.

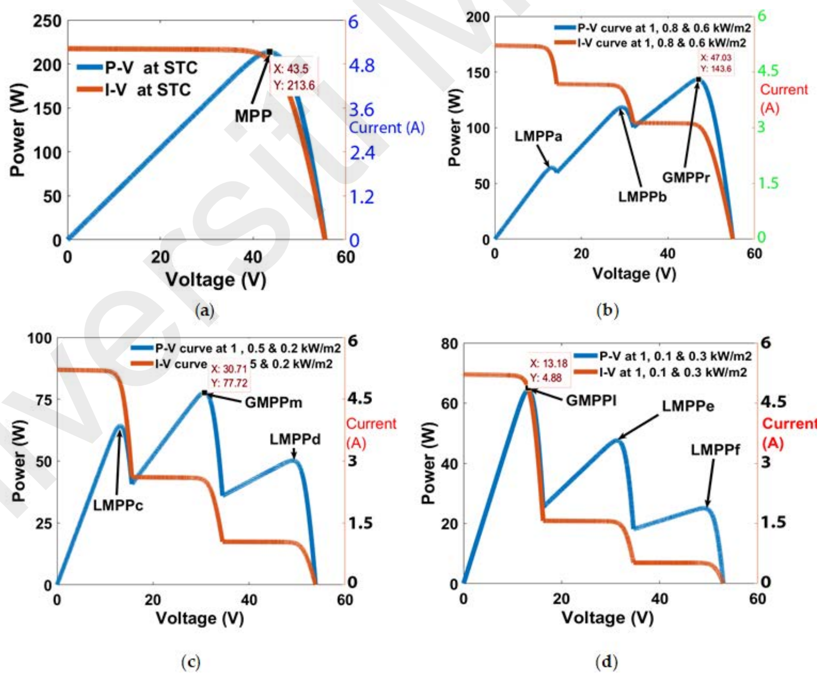

Figure 4. 22: Characteristic curves of the four irradiance profiles for the experimental test are shown as (a) uni-form weather; (b) shading pattern 1; (c) shading pattern 2; and (d) shading pattern 3.

PV array power for experimental analysis is approximately 7 times lesser than the simulated PV array because the solar simulator supports below 350 W. Figure 4.22 (a) shows the P-V and I-V curves are generated from the STC weather (1000 W/m2 and 25 °C) condition. Hence, the P-V curve generates a single MPP (43.5 V, 213.6 W). Figure 4.22 (b) demonstrates a GMPPr (0.144 kW) and two corresponding LMPPs (LMPPa and LMPPb) that occurred on the P-V curve at shading condition 1. Figure 4.24 (c) depicts P-V and I-V curves for shading condition 2, consisting of a $GMPP_m$ (0.078 kW) and other local MPPs ($LMPP_c$ and $LMPP_d$). Figure 4.22 (d) shows values of $GMPP_l$ being 0.064 kW and two LMPPs ($LMPP_e$ and $LMPP_f$) that occurred on the P-V curve at shading condition 3. These uniform and partially shading P-V and I-V curves generated from a PV model (Atlantis Energy system (SS125LM)) are implemented in the Agilent solar simulator to validate the performance of the MPPT algorithms in the experimental environment. The parameters of the PV model are presented in Table 4.1.

Table 4.1: Parameters of PV Modules for Experimental Analysis

Parameters of Atlantis Energy System SS125LM Module at STC			
Parameters	**MPP/GMPP**	**LMPP1**	**LMPP2**
Maximum Power (P_{mpp})	213.585 W	NA	NA
Voltage at MPP (V_{mpp})	43.5 V	NA	NA
Current at MPP (I_{mpp})	4.91 A	NA	NA
Open Circuit Voltage (V_{oc})	55.5 V	NA	NA
Short circuit current (I_{sc})	5.22 A	-	-
Parameters of Atlantis Energy System SS125LM at Shading Pattern 1			
Maximum Power (P_{mpp})	143.6 W	118.7 W	64.52 W
Voltage at MPP (V_{mpp})	47.03 V	29.45 V	13.18 V
Current at MPP (I_{mpp})	3.05 A	4.03 A	4.895 A
Open Circuit Voltage (V_{oc})	54.964 V	54.964 V	54.964 V
Short circuit current (I_{sc})	5.22 A	-	--
Parameters of Atlantis Energy System SS125LM at Shading Pattern 2			
Maximum Power (P_{mpp})	77.72 W	64.32 W	50.25 W
Voltage at MPP (V_{mpp})	30.71 V	13.18 V	49.12 V
Current at MPP (I_{mpp})	2.53 A	4.88 A	1.023 A
Open Circuit Voltage (V_{oc})	53.85 V	53.85 V	53.85 V
Short circuit current (I_{sc})	5.22 A	-	-
Parameters of Atlantis Energy System SS125LM at Shading Pattern 3			
Maximum Power (P_{mpp})	61.31 W	47.63 W	25.08 W
Voltage at MPP (V_{mpp})	13.18 V	31.31 V	48.98 V
Current at MPP (I_{mpp})	4.88 A	1.52 A	0.512 A
Short circuit current (I_{sc})	52.99 V	52.99 V	52.99 V
Short circuit current (I_{sc})	5.22 A	-	-

4.3.5 Experimental Results for Uniform Weather Condition

Figure 4.23 (a)-(c) shows the tracking outcomes of the conventional P&O, INC, and proposed MPPT schemes under no partially shaded condition

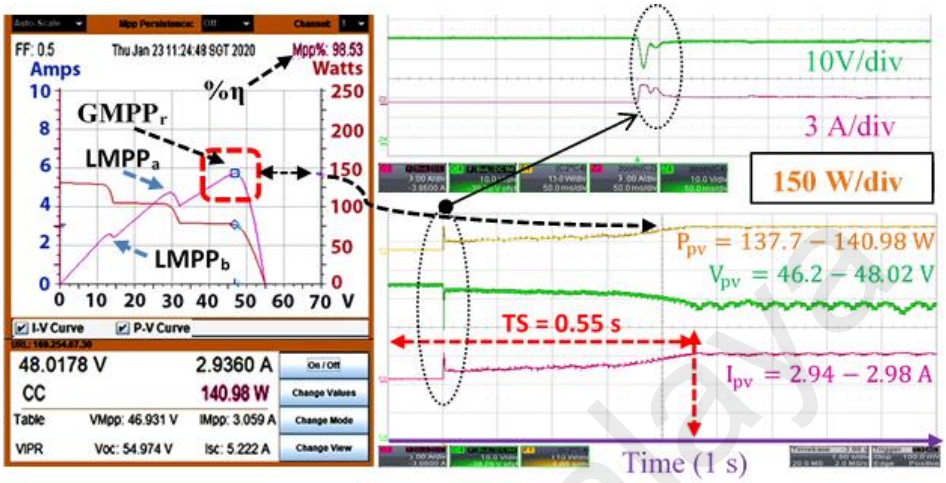

(a)

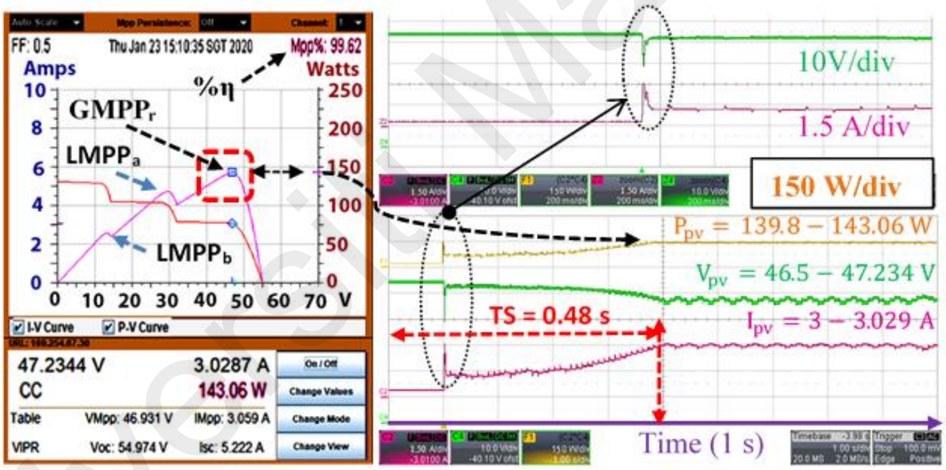

(b)

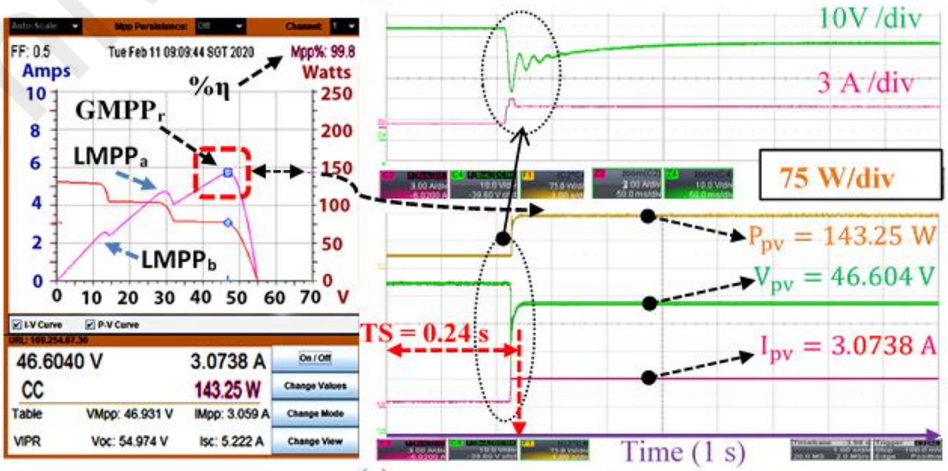

(c)

Figure 4. 23: Experimental results under STC: (a) INC-MPPT; (b) P&O-MPPT; and (c) proposed MPPT.

. Figure 4.23 (a) represents the power, voltage, and current waveforms of the conventional INC algorithm that tracks MPP within 0.575 s. However, it contains numerous power oscillations (210.5–212.66 W) under STC. The INC-MPPT continuously perturbs the duty cycle (ranged from 0.273 to 0.278) to shift the SSC's operating point location. Hence, INC and P&O MPPTs' tracking efficiency (%η) is approximately found to be 99.59 % and 99.88%, respectively, as shown in Figures 4.23 (a) and (b). The P&O-MPPT takes around 0.57 s to reach the MPP location under the uniform weather condition while experiencing power fluctuations (211–213.27 W).

Figure 4.23 (c) shows the line graphs of PV characteristic curves of the proposed algorithm. This algorithm's operating point starts propagating from a higher voltage location to a lower one to find the MPP location on the P-V curve. The proposed MPPT algorithm tracks the MPP location within 0.29 s after completing some duty cycle iterations. The proposed MPPT terminates the searching process after finding the MPP at the right place on the P-V curve. Therefore, power (P_{pv}), voltage (V_{pv}), and current (I_{pv}) oscillations are negligible because of maintaining a constant duty cycle (0.273) of the boost converter around the MPP location. The proposed MPPT algorithm is 0.4 % and 0.11 % more efficient than the conventional INC and P&O-MPPTs algorithms that are unstable around the GMPP location because of an inconsistent perturbation of the boost converter's duty cycle. In contrast, the proposed algorithm makes the duty cycle constant around the MPP location with rapid tracking and convergence speeds.

4.3.6 Experimental Results for Shading Condition 1

Figure 4.24 shows the experimental results for shading condition 1 (1, 0.8, and 0.6 kW/m^2), in which the $GMPP_r$ is located at the right side of the P-V curve. The powers of $GMPP_r$, $LMPP_a$, and $LMPP_b$ are 143.6, 118.7, and 64.52 W, respectively. Figure 4.24

(a) depicts the power (P_{pv}), voltage (V_{pv}), and current (I_{pv}) graphs obtained by applying the INC-MPPT algorithm.

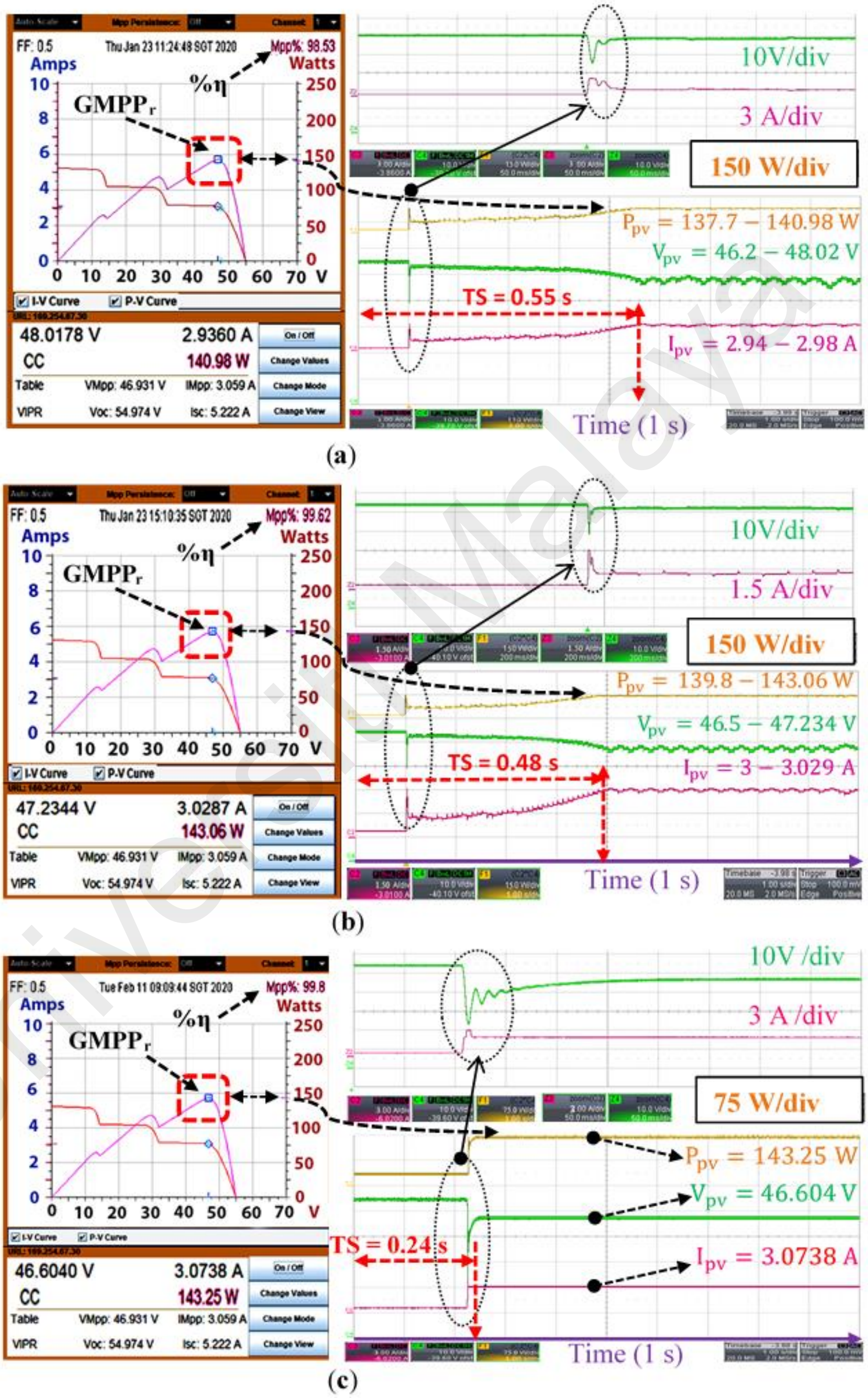

Figure 4. 24: Experimental comparison of three MPPT techniques at the right GMPP of the PSC: (a) conventional INC; (b) conventional P&O; and (c) coordinated PI-MPPT algorithms.

Here, the conventional INC-MPPT can track $GMPP_r$ location after some perturbations of the duty cycle and power fluctuations (from 137.676 to 140.98 W) around the $GMPP_r$ location. Consequently, INC-MPPT achieved 99.59% of power efficiency from the shading condition 1. The INC scheme requires at least 0.55 s to converge the operating point toward the $GMPP_r$ location with duty cycle changes from 0.181 to 0.22. Conversely, the conventional P&O algorithm can track the $GMPP_r$ location within 0.48 s with duty cycle changes between 0.2 and 0.218, as demonstrated in Figure 4.24 (b). The P&O MPPT experiences a lesser amount of power oscillation around the $GMPP_r$ (139.8–143.06 W) than the INC.

Hence, the P&O algorithm achieves a similar tracking efficiency (99.62%) as the INC algorithm. Figure 4.24 (c) shows the PV characteristic graphs and tracking results of the proposed MPPT technique. An operating point is rapidly driven toward the $GMPP_r$ location, requiring only 0.24 s tracking speed; hence, the proposed algorithm is satisfied and validated with the simulation results. The proposed MPPT method stops searching for the $GMPP_r$ location and maintains a 0.223 constant duty cycle at the SSC. The conventional INC and P&O MPPTs cannot remove power oscillations around the $GMPP_r$ at the SSC, whereas the proposed algorithm shows zero power fluctuations. Nevertheless, the power efficiency of the proposed MPPT is achieved by 99.92%.

4.3.7 Experimental Results from Shading Condition 2

Figure 4.25 (a)-(c) shows the conventional and proposed MPPT schemes' results under partially shading condition 2. The conventional INC and P&O techniques failed to track the $GMPP_m$ location because they cancel the searching process after reaching across an LMPP on the P-V curve, as shown in Figure 4.25 (a) & (b). The conventional MPPT techniques track an $LMPP_d$ (49.12 W) on the right corner of the P-V curve, resulting in power oscillations found 48 and 50 W in the INC and P&O, respectively.

Therefore, the conventional INC and P&O MPPT methods show a low tracking efficiency (62.22%) to track $LMPP_d$, and they require 0.29 s and 0.25 s, respectively, to track the LMPP instead of the $GMPP_m$ on the P-V curve.

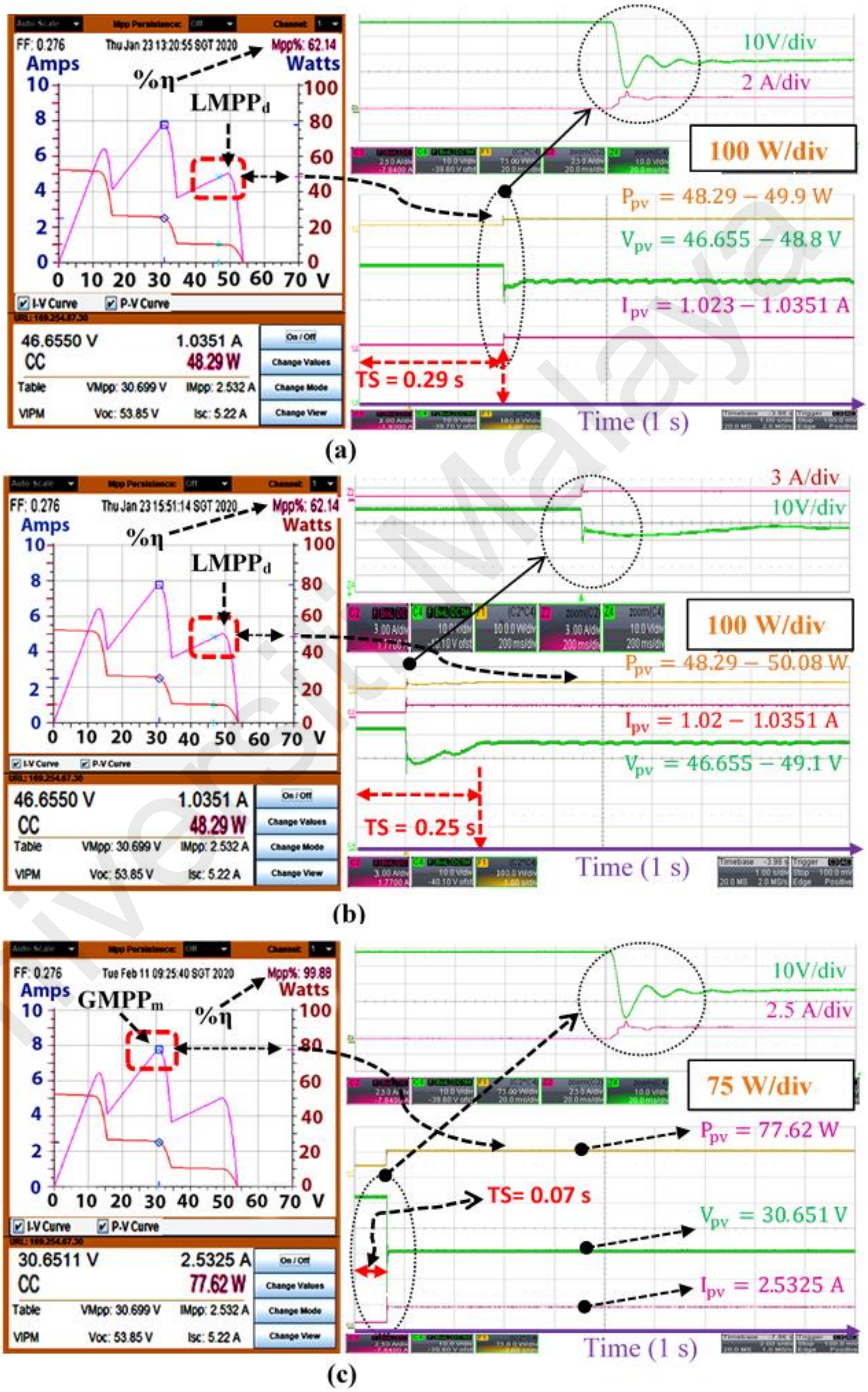

Figure 4. 25: Experimental comparison of the MPPT techniques at Shading Condition 2: (a) INC-MPPT; (b) P&O-MPPT; and (c) Proposed algorithm.

Moreover, the traditional MPPT algorithms consistently perturb the duty cycle from 0.152 to 0.187, though one of the $LMPP_d$ is tracked at the SSC. Thus, both conventional algorithms degrade tracking efficiency and prevent their operating point from moving closer to the $GMPP_m$ area at this shading condition 2. Figure 4.25 (c) shows experimental results of the proposed algorithm at shading condition 2 are satisfied with the simulation results obtained from a similar P-V curve. An operating point of the proposed MPPT first locates nearer to an $LMPP_d$ (50.25 V, 49.12 W) and then returns to track the $GMPP_m$ (30.71 V, 77.72 W). The proposed algorithm stopped searching for other LMPP locations and stuck at a duty cycle of 0.489 at the SSC after tracking the $GMPP_m$ within 0.07 s with no power oscillations. The INC, P&O, and proposed MPPT algorithms achieve a tracking efficiency of 99.95 %, 62.22 %, and 62.22 %, respectively. Hence, the proposed algorithm can operate smoothly at the shading condition 2 and enables its operating point to always be in the $GMPP_m$ region.

4.3.8 Experimental Results for Shading Condition 3

Figure 4.26 (a)-(c) illustrates the conventional and proposed MPPT schemes' experimental results at shading condition 3. In this shading condition, the $GMPP_l$, $LMPP_e$, and $LMPP_f$ comprise 64.34, 47.63, 25.08 W power in descending order, and voltages are; 13.18, 31.31, and 48.98 V, respectively. Figure 4.26 (a) shows that the conventional INC algorithm failed to reach the $GMPP_l$ location at shading condition 3. The INC algorithm starts searching for the $LMPP_e$ location along the P-V curve, resulting in excessive power oscillations (46.52–48.53 W) and continuous perturbations of the duty cycle (0.451–0.471). Thus, the INC algorithm achieved the tracking efficiency of 73.67% and propagated around the $LMPP_e$ coordinate (31.31 V, 47.63 W) with a tracking speed of 0.46 s. Similarly, Figure 4.26 (b) shows the conventional P&O algorithm failed to track $GMPP_l$, and its operating point moves around the same $LMPP_e$

location with massive power oscillation (47.29–48.3 W) and continuous perturbation of the duty cycle (0.474–0.477) as shown in Figure 4.26 (b).

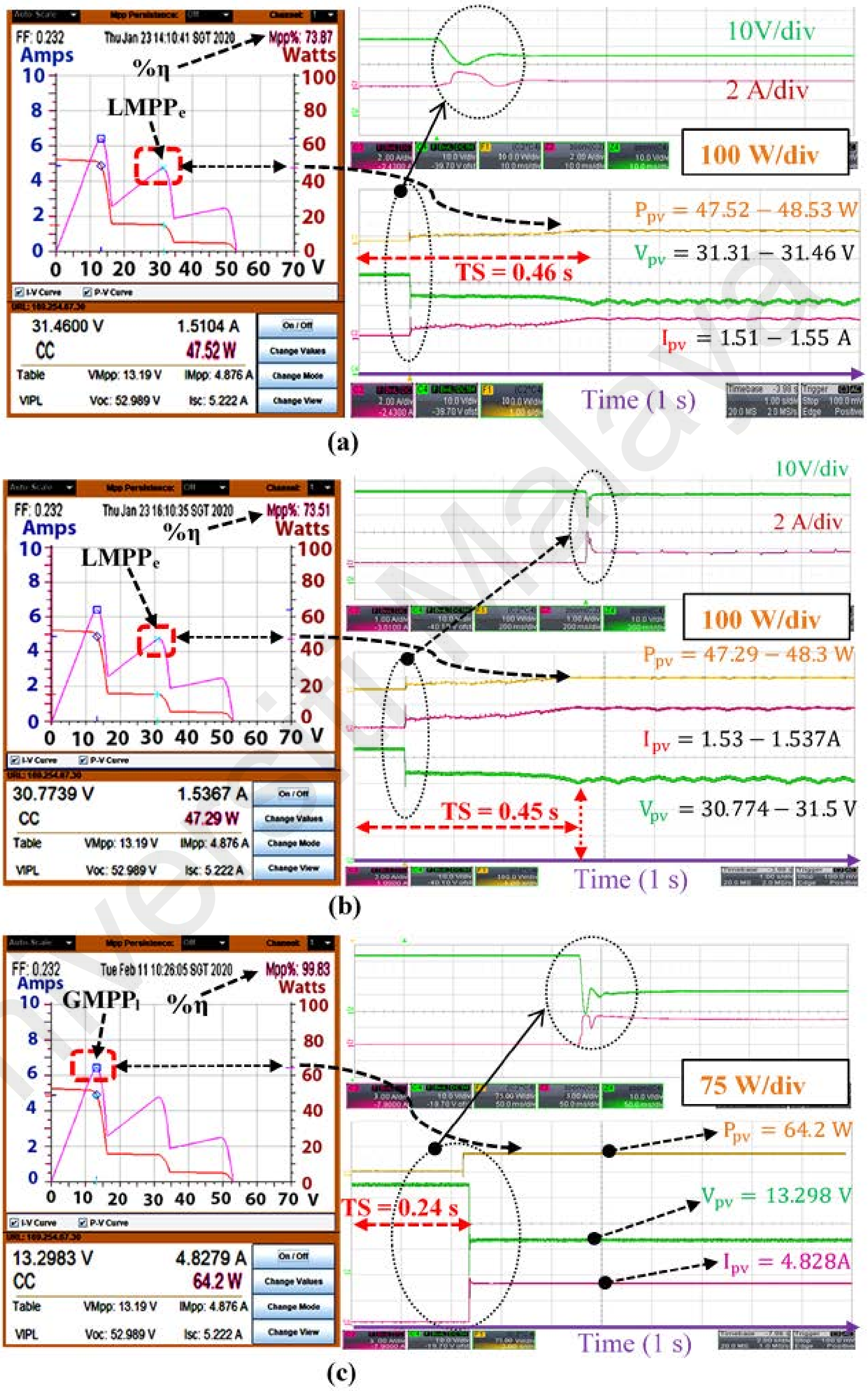

Figure 4. 26: Comparative analysis of the algorithms at the left GMPP of the PSC: (a) INC-MPPT; (b) P&O-MPPT; and (c) Proposed algorithm.

Thus, the P&O algorithm is unreliable for tracking the $GMPP_l$ under the shading condition 3 because of its low tracking efficiency (73.51%) and slow tracking speed (0.45 s). However, Figure 4.26 (c) shows the Proposed algorithm tracked the $GMPP_l$ accurately within a short time under the shading condition 3. Dragging the operating point to the SSC and reaching the $GMPP_l$ out, the proposed algorithm requires only a tracking speed (TS) of 0.24 s. A disadvantage of tracking the $GMPP_l$ using the proposed technique is that MPPT should be operated at a constant duty cycle of 0.778 at the SSC, which increases the I_{pv}. The proposed MPPT algorithm's operating point starts searching for an MPP location from the P-V curve's right side and stops at the left-sided $GMPP_l$ (13.18 V, 64.2 W) with a power efficiency of 99.83%). Thus, the proposed technique is found to be around two times more efficient than conventional techniques.

4.3.9 Experimental Results for Voltage Source Inverter (VSI)

Figure 4.27 shows the voltage, and the VSI feeds current waveforms of the unity-powered utility grid after DC power at uniform weather condition, and shading conditions 1, 2, and 3.

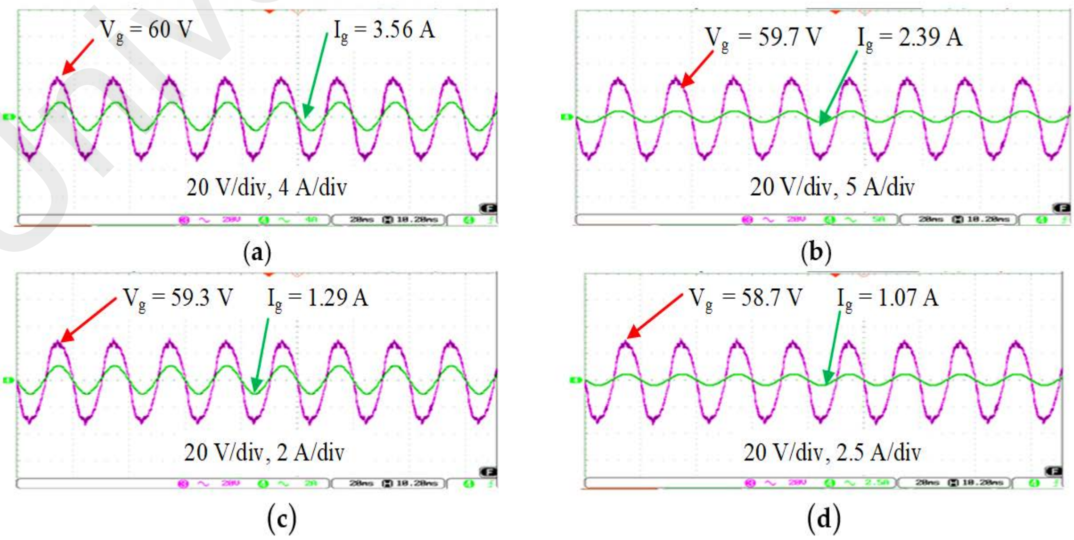

Figure 4. 27: Experimental results of the proposed VSI: (a) uniform weather; (b) shading pattern 1; (c) shading pattern 2; and (d) shading pattern 3.

These waveforms are directly matched with the scaled-down power grid because they do not show much ripple component and total harmonic distortion (THD). The waveforms of the sinusoidal grid current and voltage are taken at the SSC by neglecting the PV system's transient period. Figure 4.27 (a) shows the grid current (I_g) is in phase with grid voltage (V_g), maintaining unity power factor and supplying power to the grid with 3.56 A under a uniform weather condition. Figure 4.27 (b) shows the output power of the VSI reduces at shading pattern 1 because the current decreases by 1.17 A, and maintaining the grid voltage of 59.7 V. Similarly, Figure 4.27 (c)–(d) shows the grid currents and voltages are 59.3 V and 58.7 V; and 1.29 A, and 1.07 A, respectively, under the shading patterns 2 and 3. Experimental and simulation results of the VSI are validated because the same phase and frequency of the grid current and voltage are obtained from both comparative studies.

4.4 Comparative Study of the MPPTs Results

This section highlights the simulation and experimental results with different contingency analyses of the proposed and conventional MPPT techniques (Tables 4 and 5). The conventional MPPTs cause enormous power loss and perturb the wrong size of the duty cycle at shading conditions 2 and 3 in tracking an MPP and $GMPP_r$ under uniform weather and shading condition 1. The performance of the conventional MPPTs is found to be similar between the simulation and experimental studies. Under uniform and shading conditions 1, 2, and 3, tracking efficiencies are 83.89%, 84.38%, and 99.96% for the INC, P&O, and proposed MPPT schemes, respectively. Hence, the proposed MPPT technique exhibits much higher efficiency than the conventional algorithms. Consequently, the proposed technique is more robust and efficient than traditional MPPT algorithms under uniform and shading conditions.

4.4.1 Comparative Study of the Simulation Results

As illustrated in Table 4.2, the proposed PI-MPPT algorithm is evaluated under a uniform weather condition and shading conditions 1, 2, and 3.

Table 4.2: Comparative study of simulated parameters among MPPTs

Simulated Parameters		MPPT Algorithms		
		INC	**P&O**	**Proposed**
Uniform weather (1497 W)	Power Oscillation (W)	1470-1500	1473-1500	No
	Duty Cycle (D)	0.442-0.452	0.44-0.46	0.4745
	%η of MPP	98.2 %	98.3 %	99.99 %
	Tracking Speed (TS)	0.195 s	0.21 s	0.19 s
Shading condition 1 (1275 W)	Power Oscillation (W)	1230-1267	1250-1275	No
	Duty Cycle (D)	0.38-0.41	0.37-0.41	0.458
	%η of GMPPr	99.48 %	99.66 %	99.93 %
	Tracking Speed (TS)	0.205 s	0.215 s	0.13 s
Shading condition 2 (924.4 W)	Power Oscillation (W)	830-925	850-925	No
	Duty Cycle (D)	0.5-0.52	0.49-0.52	0.647
	%η of $LMPP_d$ / $GMPP_m$	63.26 %	63.46 %	99.96 %
	TS for $LMPP_d$ / $GMPP_m$	0.21 s	0.22 s	0.205 s
Shading condition 3 (487.6 W)	Power Oscillation (W)	294-325	294-326	No
	Duty Cycle (D)	0.18-0.32	0.44-0.46	0.829
	%η of $LMPP_e$ / $GMPP_l$	75.3 %	76.8 %	99.86 %
	TS for $LMPP_e$ / $GMPP_l$	0.39 s	0.315 s	0.15 s

The proposed algorithm can track the MPP, $GMPP_r$, $GMPP_m$, and $GMPP_L$ locations within 0.19, 0.13, 0.205, and 0.13 s at uniform weather and shading conditions 1, 2, and 3, respectively. Tracking speeds (TSs) of the INC, P&O, and proposed PI-MPPT algorithms are 0.39, 0.315, and 0.13 s, respectively, at shading condition 3. Hence, the proposed algorithm can track the $GMPP_L$ approximately two times faster than the traditional MPPT schemes at the shading condition 3.

4.4.2 Comparative Study of Experimental Results

Experimental results with different contingency analyses of the proposed and conventional MPPT techniques are highlighted in this section, as shown in Table 4.3.

Table 4.3: Experimental comparison of the proposed and conventional algorithms

Simulated MPP Values/ Experimental Parameters		MPPT Algorithms' Performance		
		INC	**P&O**	**Proposed**
Uniform weather (213.6 W)	Power Oscillation (W)	210.5-212.66	211-213.29	No
	Duty Cycle (D)	0.273-0.278	0.247-0.253	0.273
	%η of MPP	99.59	99.88	99.99
	Tracking Speed (TS)	0.575	0.57	0.29
Shading condition 1 (143.6 W)	Power Oscillation (W)	137.7-140.98	139.8-143.06	No
	Duty Cycle (D)	0.181-0.22	0.2-0.218	0.223
	%η of GMPPr	99.59	99.62	99.92
	Tracking Speed (TS)	0.55	0.48	0.24
Shading condition 2 (77.72 W)	Power Oscillation (W)	48.29-50.08	48.29-50.08	No
	Duty Cycle (D)	0.152-0.158	0.168-0.187	0.489
	%η of $LMPP_d$ / $GMPP_m$	62.22	62.22	99.95
	TS for $LMPP_d$ / $GMPP_m$	0.29	0.25	0.07
Shading condition 3 (64.31 W)	Power Oscillation (W)	47.52-48.53	47.29-48.3	No
	Duty Cycle (D)	0.451-0.471	0.474-0.477	0.778
	%η of $LMPP_e$ / $GMPP_l$	73.51	73.67	99.83
	TS for $LMPP_e$ / $GMPP_l$	0.46	0.45	0.24

All algorithms can track MPP efficiently (above 99% efficiency) under uniform weather conditions. Tracking speed (TS) is higher in the proposed MPPT than the conventional ones under the uniform weather condition. However, the conventional INC and P&O MPPT algorithms cause enormous power loss and perturb the wrong step size of a duty cycle under shading conditions 2 and 3.

4.4.3 Comparative Study between Literature and Experimental Results

A comparative study is performed in this section between literature and experimental outcomes to investigate the parameters' performance, such as complexity, power efficiency, tracking speed, dependency, and reliability, when the INC, P&O and Proposed MPPT algorithms are exposed to shading conditions 1, 2, and 3.

Table 4.4: Detail comparison study of the proposed scheme with other algorithms in both Literature and Experimental outcomes

Weathers/Parameters/Algorithms			INC	P&O	PI-MPPT
Normal Weather	%MPP	Literature[14]	97	98	99.92
		Experimental	99.59	99.88	
	Tracking Speed (s)	Literature[15]	0.25	0.27	0.29
		Experimental	0.575	0.57	
PSC to Right GMPP	%GMPP	Literature[16]	99	98	99.8
		Experimental	99.53	99.62	
	Tracking Speed (s)	Literature[17]	0.2	0.2	0.24
		Experimental	0.55	0.48	
PSC to Middle GMPP	%GMPP	Literature[18]	65	60	99.88
		Experimental	62.14	62.14	
	Tracking Speed (s)	Literature[19]	0.25	0.20	0.07
		Experimental	0.29	0.25	
PSC to Left GMPP	%GMPP	Literature[20]	75	70	99.83
		Experimental	73.67	73.51	
	Tracking Speed (s)	Literature[21]	0.4	0.5	0.24
		Experimental	0.46	0.45	
Potential GMPP tracking ability at pattern 2&3			No	No	Yes
Complexity			Simple	Simple	Medium
Cost			High	Medium	Low
Tracking Speed			Low	Low	High
Steady-State Oscillation			High	High	No
Reliability			Low	Low	High

[14] Kabalci, E., Gokkus, G., & Gorgun, A. (2015, June). Design and implementation of a PI-MPPT based Buck-Boost converter. In *2015 7th International Conference on Electronics, Computers and Artificial Intelligence (ECAI)* (pp. SG-23). IEEE.

[15] Khaled, A. M. E. U. R., Aboubakeur, H. A. D. J. A. I. S. S. A., Mohamed, B. O. U. T. O. U. B. A. T., & Nabil, A. B. O. U. C. H. A. B. A. N. A. (2018, November). A Fast MPPT Control Technique Using PID Controller in a Photovoltaic System. In *2018 International Conference on Applied Smart Systems (ICASS)* (pp. 1-5). IEEE.

[16] . Implementation of INC-PIMPPT and its comparison with INC MPPT by direct duty cycle control for solar photovoltaics employing zeta converter.

[17] Bouchakour, A., Borni, A., & Brahami, M. (2019). Comparative study of P&O-PI and fuzzy-PI MPPT controllers and their optimisation using GA and PSO for photovoltaic water pumping systems. *International Journal of Ambient Energy*, 1-12.

[18] Liu, Y., Liu, X., Shi, D., Zhang, Y., Wu, Q., Zhu, Z., & Lin, X. (2019, June). An MPPT Approach Using Improved Hill Climbing and Double Closed Loop Control. In *2019 IEEE 46th Photovoltaic Specialists Conference (PVSC)* (pp. 2935-2941). IEEE.

[19] Huynh, D. C., & Dunnigan, M. W. (2016). Development and comparison of an improved incremental conductance algorithm for tracking the MPP of a solar PV panel. IEEE Transactions on Sustainable Energy, 7(4), 1421-1429.

[20] Soon, T. K., & Mekhilef, S. (2014). A fast-converging MPPT technique for photovoltaic system under fast-varying solar irradiation and load resistance. Industrial Informatics, IEEE Transactions on, 11(1), 176-186.

[21] Manickam, C., Raman, G. R., Raman, G. P., Ganesan, S. I., & Nagamani, C. (2016). A Hybrid Algorithm for Tracking of GMPP Based on P&O and PSO With Reduced Power Oscillation in String Inverters. IEEE Transactions on Industrial Electronics, 63(10), 6097-6106.

Table 4.4 compares the proposed coordinated PI-MPPT algorithm with conventional INC and P&O MPPT techniques, considering the predicted values of the PV parameters in the literature review, and experimental results at four weather conditions. A little difference of the proposed MPPT technique's PV parameters is found between the literature values and experimental results. This variation is evident because of some system and component losses in the experimental analysis. The conventional algorithms are comparatively simple than the proposed MPPT, but they show very low efficiency and consistency in looking for the LMPP. For example, tracking an MPP location is not equal in both INC and P&O MPPT algorithms. The conventional MPPT algorithms fail to track GMPP location, especially when exposed to shading patterns 2 and 3. The proposed algorithm enables the operating point to successfully search for the $GMPP_r$, $GMPP_m$, and $GMPP_l$ locations skipping a portion of the P-V curve, increasing accuracy and robustness in the tracking process. In contrast, the traditional MPPT techniques are mutually not compatible in this circumstance. The tracking time of all algorithms is longer under the shading conditions 2 than other shading and uniform solar insolation conditions.

4.5 Summary

In this chapter 4, the shortcomings of P&O and incremental conductance MPPTs are discussed. The proposed coordinated PI-MPPT algorithm is an effective algorithm than conventional MPPT schemes under acute and stochastic weather conditions. The proposed coordinated PI-MPPT demonstrated better performance concerning tracking speed, power oscillations, and tracking efficiency. Though the proposed MPPT scheme's demonstrated results are worthy enough, one cannot conclude that this algorithm works better than that of hybrid and improved MPPT techniques developed in different research works. Nevertheless, the proposed technique is more reliable, robust, and less dependent on initial MPP locations, has an accurate and reliable tracking of the

GMPP location. The VSI is experimentally tested to investigate the energy transformation from DC-link to a single-phase AC grid system with maintaining unity power factor and without injecting harmonic components of the current and voltage waveforms into the utility grid. The PR controller maximized the real-power output of the FB-VSI. The SRF-PLL matched the output voltage and the current between the VSI and grid with the same phase and frequency. Moreover, the VSI injected sinusoidal current to the grid is regulated precisely and stiffly using PR and PI controllers. The experimental result presented in this chapter is validated with the grid-connected PV system.

CHAPTER 5: CONCLUSION AND FUTURE WORK

5.1 Conclusion

This research has reviewed renewable energy sources such as solar power plants, DC-DC converters, DC-AC single-phase VSI topologies, and filter circuit designs. This study also included a detailed comparison between offline, online, hill climbing, and combined MPPT algorithms in the review section. PI controllers were performed in simulation work, and the dSPACE controller interfaced with the hardware system to control PWM and SPWM signals. For the grid synchronization with the converters, PR and SRE-PLL controllers generated zero steady-state error and fewer harmonic distortions on the VSI waveforms, respectively. In this dissertation, the PV module was simulated under different solar irradiation conditions to evaluate the performance of the tracking MPP and GMPPs from the P-V curves. Therefore, the output power of the PV module has a significant effect on radiation levels. The converter's function is to regulate the PV voltage and current and keep them at a desired constant level. The two-staged converter topologies have been used to connect the PV module to the utility grid. The main principle of connecting the inverter with the grid is to deliver highly efficient power and reliable operation of the proposed system. In Chapter 3, the DC-DC boost converter and H-bridge VSI were designed by selecting the frequency of 10 kHz that reduces the boost converter's cost because the size of the components is reduced if the switching frequency is increased.

Chapter 4 shows that the DC-DC converters were built using MATLAB Simulink and validated with a series of experimental studies. The feedback controller is built-in MATLAB Simulink software and hardware setup with current and voltage sensors. The complexity of implanting MPPT algorithms is minimized using a powerful but expensive digital controller (dSPACE). This study evaluates a proposed coordinated PI-

MPPT algorithm compared to the other two conventional MPPT techniques to track GMPP on a PV module subjected to an acute and three partial shading conditions. The proposed method is faster, more robust, sustainable, and reliable than the conventional offline and online MPPT schemes reviewed in the literature when exposed to the series-connected PV modules subjected to bypass diodes and multiple MPPs on P-V curve. Experimental and simulation results demonstrated that the proposed PI-MPPT algorithm tracked the GMPPr (shading condition 1), $GMPP_m$ (shading condition 2), and GMPPl (shading condition 3) as compared to the traditional MPPT techniques. The literature work's PV parameters are verified and matched in both simulation and experimental studies with good accuracy, reliability, and faster tracking response. The proposed algorithm's computational burden is lowered by using a simple algorithm, dSPACE controller, and suitable hardware components. The proposed algorithm is tested numerous times both in simulation and experimental analyses and found that it has high precision and less dependency on different weather conditions. Table 4.1 & Table 4.3 highlight a detailed comparative study of the algorithms' verification when they are exposed to three shading patterns and an acute weather condition.

5.2 Future Work

For this dissertation, some work can be done to improve the implemented grid-connected PV system's efficiency. Therefore, some of the future works are highlighted below:

- To achieve maximum efficiency of the MPPT, further comparative study of the proposed algorithm's performance can be extensively investigated with modified and hybrid MPPT techniques.
- The proposed technique can be evaluated under different shading patterns subjected to more than three multiple peaks and load variations.

- The extension of simulation on a three-phase inverter and three-phase grid-connected photovoltaic power plants with a higher number of voltage levels could be done.
- The presented hardware could be implemented as a prototype on a printed circuit board (PCB) with the proposed algorithm loaded into the dSPACE controller. The overall unit can be developed as an end-user-product with different specifications.

REFERENCES

Abdelsalam, A. K., Massoud, A. M., Ahmed, S., & Enjeti, P. N. (2011). High-performance adaptive perturb and observe MPPT technique for photovoltaic-based microgrids. *IEEE transactions on power electronics, 26*(4), 1010-1021.

Abdourraziq, S., & El Bachtiri, R. (2014). *A perturb and observe method using fuzzy logic control for PV pumping system.* Paper presented at the 2014 International Conference on Multimedia Computing and Systems (ICMCS).

Ahmad, S., Rashid, M. T., Ferdowsy, C. S., Islam, S., & Mahmood, A. H. (2015, 19-20 Dec. 2015). *A technical comparison among different PV-MPPT algorithms to observe the effect of fast changing solar irradiation.* Paper presented at the 2015 IEEE International WIE Conference on Electrical and Computer Engineering (WIECON-ECE).

Albatran, S., Allabadi, A. S., Al Khalaileh, A. R., & Fu, Y. (2020). Improving the Performance of a Two-Level Voltage Source Inverter in the Overmodulation Region Using Adaptive Optimal Third Harmonic Injection Pulsewidth Modulation Schemes. *IEEE transactions on power electronics, 36*(1), 1092-1103.

Anto, E. K., Asumadu, J. A., & Okyere, P. Y. (2016). *PID control for improving P&O-MPPT performance of a grid-connected solar PV system with Ziegler-Nichols tuning method.* Paper presented at the 2016 IEEE 11th Conference on Industrial Electronics and Applications (ICIEA).

Aroul, K., Umashankar, S., Prabhu, K., & Sanjeevikumar, P. (2018). Reviewing the Performance of an Improved Seven-Level Multilevel Inverter for Various Pulse Width Modulation Techniques. In *In Advances in Electronics, Communication and Computing* (pp. 479-490): Springer, Singapore.

Ashique, R. H., Salam, Z., & Ahmed, J. (2015, October). *An adaptive P&O MPPT using a sectionalized piece-wise linear PV curve.* Paper presented at the 2015 IEEE Conference on Energy Conversion (CENCON). IEEE.

Asok, S. K., Baburaj, F., Jayaprakash, P., & Mukundan, N. (2018, March). *Proportional Resonant Based Current Control Of Three-Phase Single Stage Grid Connected PV System.* Paper presented at the 2018 International Conference on Control, Power, Communication and Computing Technologies (ICCPCCT). IEEE.

Awasthi, A., Shukla, A. K., SR, M. M., Dondariya, C., Shukla, K., Porwal, D., & Richhariya, G. (2020). Review on sun tracking technology in solar PV system. *Energy Reports, 6*, 392-405.

Baburajan, S., Peyghami, S., Kumar, D., Blaabjerg, F., & Davari, P. (2020). *Effect of Unipolar and Bipolar SPWM on the Lifetime of DC-link Capacitors in Single-Phase Voltage Source Inverters.* Paper presented at the 2020 22nd European Conference on Power Electronics and Applications (EPE'20 ECCE Europe).

Belhachat, F., & Larbes, C. (2018). A review of global maximum power point tracking techniques of photovoltaic system under partial shading conditions. *Renewable and Sustainable Energy Reviews, 92*, 513-553.

Bendib, B., Belmili, H., & Krim, F. (2015). A survey of the most used MPPT methods: Conventional and advanced algorithms applied for photovoltaic systems. *Renewable and Sustainable Energy Reviews, 45*, 637-648.

Bhattacharyya, S., Samanta, S., & Mishra, S. (2020). Steady Output and Fast Tracking MPPT (SOFT-MPPT) for P&O and InC Algorithms. *IEEE Transactions on Sustainable Energy, 12*(1), 293-302.

Bi, Z., Ma, J., Wang, K., Man, K. L., Smith, J. S., & Yue, Y. (2020). Identification of partial shading conditions for photovoltaic strings. *IEEE Access, 8*, 75491-75502.

Bollipo, R. B., Mikkili, S., & Bonthagorla, P. K. (2020). Critical review on PV MPPT techniques: classical, intelligent and optimisation. *IET Renewable Power Generation, 14*(9), 1433-1452.

Bonthagorla, P. K., & Mikkili, S. (2020). Optimal PV array configuration for extracting maximum power under partial shading conditions by mitigating mismatching power loss. *CSEE Journal of Power and Energy Systems*.

Bouchakour, A., Borni, A., & Brahami, M. (2019). Comparative study of P&O-PI and fuzzy-PI MPPT controllers and their optimisation using GA and PSO for photovoltaic water pumping systems. *International Journal of Ambient Energy*, 1-12.

Bouzerdoum, M., & Mellit, A. (2017, October). *Performance prediction of a grid-connected photovoltaic plant.* Paper presented at the 2017 5th International Conference on Electrical Engineering-Boumerdes (ICEE-B).

Carannante, G., Fraddanno, C., Pagano, M., & Piegari, L. (2009). Experimental performance of MPPT algorithm for photovoltaic sources subject to inhomogeneous insolation. *IEEE Transactions on Industrial Electronics, 56*(11), 4374-4380.

Cha, H., Vu, T. K., & Kim, J. E. (2009). *Design and control of Proportional-Resonant controller based Photovoltaic power conditioning system.* Paper presented at the Energy Conversion Congress and Exposition, 2009. ECCE 2009. IEEE.

Charaabi, A., Barambones, O., Zaidi, A., & Zanzouri, N. (2020). *A Novel Two Stage Controller for a DC-DC Boost Converter to Harvest Maximum Energy from the PV Power Generation.* Paper presented at the Actuators.

Darcy Gnana Jegha, A., Subathra, M., Manoj Kumar, N., Subramaniam, U., & Padmanaban, S. (2020). A High Gain DC-DC Converter with Grey Wolf Optimizer Based MPPT Algorithm for PV Fed BLDC Motor Drive. *Applied Sciences, 10*(8), 2797.

Deshpande, A., Patil, S., & Deopare, H. (2016, April). *Comparative simulation of conventional maximum power point tracking methods.* Paper presented at the 2016 International Conference on Computing, Communication and Automation (ICCCA). IEEE.

Despotovic, M., & Nedic, V. (2015). Comparison of optimum tilt angles of solar collectors determined at yearly, seasonal and monthly levels. *Energy Conversion and Management, 97*, 121-131.

Ebhota, W. S., & Jen, T.-C. (2020). Fossil fuels environmental challenges and the role of solar photovoltaic technology advances in fast tracking hybrid renewable energy system. *International Journal of Precision Engineering and Manufacturing-Green Technology, 7*(1), 97-117.

El Khateb, A. H., Rahim, N. A., Selvaraj, J., & Williams, B. W. (2014). DC-to-DC converter with low input current ripple for maximum photovoltaic power extraction. *IEEE Transactions on Industrial Electronics, 62*(4), 2246-2256.

Elgendy, M. A., Zahawi, B., & Atkinson, D. J. (2014, 8-10 April 2014). *Evaluation of incremental conductance MPPT algorithm at low perturbation rates.* Paper presented at the 7th IET International Conference on Power Electronics, Machines and Drives (PEMD 2014).

Eltarouty, A., Aboudan, M., Biricik, S., Ahmed, H., & Benbouzid, M. (2020). *Unbalance and Disturbance Rejection Based Phase Locked Loop for Grid*

Synchronization. Paper presented at the IECON 2020 The 46th Annual Conference of the IEEE Industrial Electronics Society.

Eltawil, M. A., Zhao, Z. J. R., & Reviews, S. E. (2010). Grid-connected photovoltaic power systems: Technical and potential problems—A review. *Renewable and Sustainable Energy Reviews, 14*(1), 112-129.

Esfahani, S. K., Karrech, A., Cameron, R., Elchalakani, M., Tenorio, R., & Jerez, F. (2020). Optimizing the solar energy capture of residential roof design in the southern hemisphere through Evolutionary Algorithm. *Energy and Built Environment*.

Ezinwanne, O., Zhongwen, F., & Zhijun, L. (2017). Energy Performance and Cost Comparison of MPPT Techniques for Photovoltaics and other Applications. *Energy Procedia, 107*(156), 297-303.

Faldu, K. S., & Kulkarni, P. (2020). *Maximization of the output power from photovoltaic array under partial shading conditions.* Paper presented at the 2020 IEEE International Students' Conference on Electrical, Electronics and Computer Science (SCEECS).

Fantino, R. A., Busada, C. A., & Solsona, J. A. (2020). Grid Impedance Estimation by Measuring Only the Current Injected to the Grid by a VSI With $ LCL $ Filter. *IEEE Transactions on Industrial Electronics, 68*(3), 1841-1850.

Farhat, M., Barambones, O., & Sbita, L. (2015). Efficiency optimization of a DSP-based standalone PV system using a stable single input fuzzy logic controller. *Renewable and Sustainable Energy Reviews, 49*, 907-920.

Fatima, T., Shahzad, U., & Cui, L. (2020). Renewable and nonrenewable energy consumption, trade and CO2 emissions in high emitter countries: does the income level matter? *Journal of Environmental Planning and Management*, 1-25.

Harrag, A., & Messalti, S. (2015). Variable step size modified P&O MPPT algorithm using GA-based hybrid offline/online PID controller. *Renewable and Sustainable Energy Reviews, 49*, 1247-1260.

Hashemi, B., Cretu, A.-M., & Taheri, S. (2020). Snow Loss Prediction for Photovoltaic Farms Using Computational Intelligence Techniques. *IEEE Journal of Photovoltaics, 10*(4), 1044-1052.

Heidari, N., Gwamuri, J., Townsend, T., & Pearce, J. M. (2015). Impact of Snow and ground interference on photovoltaic electric system performance. *IEEE Journal of Photovoltaics, 5*(6), 1680-1685.

Heinisch, V., Odenberger, M., Göransson, L., & Johnsson, F. (2019). Prosumers in the Electricity System—Household vs. System Optimization of the Operation of Residential Photovoltaic Battery Systems. *Frontiers in Energy Research, 6*, 145.

Hossain, M. J., Tiwari, B., & Bhattacharya, I. (2016). *An adaptive step size incremental conductance method for faster maximum power point tracking.* Paper presented at the 2016 IEEE 43rd Photovoltaic Specialists Conference (PVSC).IEEE.

Hsieh, G.-C., Hsieh, H.-I., Tsai, C.-Y., & Wang, C.-H. (2012). Photovoltaic power-increment-aided incremental-conductance MPPT with two-phased tracking. *IEEE transactions on power electronics, 28*(6), 2895-2911.

Hu, D., Yin, A., & Ghaderi, D. (2020). A transformer-less single-switch boost converter with high-voltage gain and mitigated-voltage stress applicable for photovoltaic utilizations. *International Transactions on Electrical Energy Systems, 30*(10), e12569.

Hua, C. C., Fang, Y. H., & Chen, W. T. (2016). Hybrid maximum power point tracking method with variable step size for photovoltaic systems. *IET Renewable Power Generation, 10*(2), 127-132.

Huang, C., Wang, L., Yeung, R. S. C., Zhang, Z., Chung, H. S. H., & Bensoussan, A. (2017). A prediction model-guided Jaya algorithm for the PV system maximum power point tracking. *IEEE Transactions on Sustainable Energy, 9*(1), 45-55.

Husain, M. A., Tariq, A., Hameed, S., Arif, M. S. B., & Jain, A. (2017). Comparative assessment of maximum power point tracking procedures for photovoltaic systems. *Green Energy & Environment, 2*(1), 5-17.

Hussein, K. H., Muta, I., Hoshino, T., & Osakada, M. (1995). Maximum photovoltaic power tracking: an algorithm for rapidly changing atmospheric conditions. *IEE Proceedings - Generation, Transmission and Distribution, 142*(1), 59-64.

Huynh, D. C., & Dunnigan, M. W. (2016). Development and comparison of an improved incremental conductance algorithm for tracking the MPP of a solar PV panel. *IEEE Transactions on Sustainable Energy, 7*(4), 1421-1429.

Huynh, P., & Cho, B. H. (1996). Design and analysis of a microprocessor-controlled peak-power-tracking system [for solar cell arrays]. *IEEE Transactions on Aerospace and Electronic Systems, 32*(1), 182-190.

Ibrahim, A., Aboelsaud, R., & Obukhov, S. (2019). *Comprehensive Analysis of PSO and P&O for the Global Maximum Power Point Tracking of the PV under Partial Shading.* Paper presented at the 2019 International Youth Conference on Radio Electronics, Electrical and Power Engineering (REEPE).

Ibrahim, A. O., & Basir, O. (2013). *A novel sensorless support vector regression based multi-stage algorithm to track the maximum power point for photovoltaic systems.* Paper presented at the 2013 IEEE Power & Energy Society General Meeting.IEEE.

IsaTezde, E., MuhsinDemir, M., Gurel, F., IbrahimOkumus, H., & Kahveci, H. (2018). *Two-Stage Power Converter Design and Control for Renewable Energy Systems.* Paper presented at the 2018 IEEE 18th International Power Electronics and Motion Control Conference (PEMC).

Islam, H., Mekhilef, S., Shah, N., Soon, T., Seyedmahmousian, M., Horan, B., & Stojcevski, A. (2018). Performance evaluation of maximum power point tracking approaches and photovoltaic systems. *Energies, 11*(2), 365.

Islam, S., Zeb, K., Din, W., Khan, I., Ishfaq, M., Busarello, T., & Kim, H. J. E. (2018). Design of a Proportional Resonant Controller with Resonant Harmonic Compensator and Fault Ride Trough Strategies for a Grid-Connected Photovoltaic System. *Electronics, 7*(12), 451.

Jana, S., Kumar, N., Mishra, R., Sen, D., & Saha, T. K. (2020). Development and implementation of modified MPPT algorithm for boost converter-based PV system under input and load deviation. *International Transactions on Electrical Energy Systems, 30*(2), e12190.

Jasuan, A., Nawawi, Z., & Samaulah, H. (2018. October). *Comparative Analysis of Applications Off-Grid PV System and On-Grid PV System for Households in Indonesia.* Paper presented at the 2018 International Conference on Electrical Engineering and Computer Science (ICECOS). IEEE.

Jedari, M., Gharehpetian, G., Fathi, S. H., & Vahids, S. (2016). *An adaptive InCon MPPT algorithm considering irradiance slope tracking for PV application.* Paper presented at the 2016 4th International Symposium on Environmental Friendly Energies and Applications (EFEA).

Ji, Y. H., Jung, D. Y., Kim, J. G., Kim, J. H., Lee, T. W., & Won, C. Y. (2010). A real maximum power point tracking method for mismatching compensation in PV array under partially shaded conditions. *IEEE transactions on power electronics, 26*(4), 1001-1009.

Jiandong, D., Ma, X., & Tuo, S. (2018, September). *A Variable Step Size P&O MPPT Algorithm for Three-Phase Grid-Connected PV Systems.* Paper presented at the 2018 China International Conference on Electricity Distribution (CICED). IEEE.

Jiang, L. L., Nayanasiri, D., Maskell, D. L., & Vilathgamuwa, D. (2015). A hybrid maximum power point tracking for partially shaded photovoltaic systems in the tropics. *Renewable Energy, 76*, 53-65.

Jiang, Y., Qahouq, J. A. A., & Haskew, T. A. (2012). Adaptive step size with adaptive-perturbation-frequency digital MPPT controller for a single-sensor photovoltaic solar system. *IEEE transactions on power electronics, 28*(7), 3195-3205.

Jiang, Z., Chen, Y., Zhang, B., Qiu, D., & Xie, F. (2020). Multiscale Modeling and Analysis of Boost Converter Based on Device Mechanism Model and Continuous Switching Function. *IEEE Journal of Emerging and Selected Topics in Power Electronics*.

Joisher, M., Singh, D., Taheri, S., Espinoza-Trejo, D. R., Pouresmaeil, E., & Taheri, H. (2020). A hybrid evolutionary-based MPPT for photovoltaic systems under partial shading conditions. *IEEE Access, 8*, 38481-38492.

Joshi, S., & Sharma, P. (2018). *Green growth and development: evaluating sustainability impacts of solar energy transitions in India.* Discipline of Economics, IIT Indore.

Kabalcı, E. (2020). Review on novel single-phase grid-connected solar inverters: Circuits and control methods. *Solar Energy, 198*, 247-274.

Kabalci, E., Gokkus, G., & Gorgun, A. (2015). *Design and implementation of a PI-MPPT based Buck-Boost converter.* Paper presented at the 2015 7th International Conference on Electronics, Computers and Artificial Intelligence (ECAI).

Kafui, A. D., Seres, I., & Farkas, I. (2019). Efficiency comparison of different photovoltaic modules. *Acta Technologica Agriculturae, 22*(1), 5-11.

Kalair, A., Abas, N., Saleem, M. S., Kalair, A. R., & Khan, N. (2020). Role of energy storage systems in energy transition from fossil fuels to renewables. *Energy Storage*, e135.

Kalavalli, C., Meenalochini, P., Selvaprasanth, P., & Haq, S. S. A. (2020). Dual loop control for single phase PWM inverter for distributed generation. *Materials Today: Proceedings*.

Kamarzaman, N. A., & Tan, C. W. (2014). A comprehensive review of maximum power point tracking algorithms for photovoltaic systems. *Renewable and Sustainable Energy Reviews, 37*, 585-598.

Karami, N., Moubayed, N., & Outbib, R. (2017). General review and classification of different MPPT Techniques. *Renewable and Sustainable Energy Reviews, 68*, 1-18.

Kermadi, M., & Berkouk, E. M. (2015). *A hybrid PSO-PI based maximum power point tracking algorithm using adaptive sampling time strategy.* Paper presented at the 2015 4th International Conference on Electrical Engineering (ICEE).

Khaled, A., Aboubakeur, H., Mohamed, B., & Nabil, A. (2018). *A Fast MPPT Control Technique Using PID Controller in a Photovoltaic System.* Paper presented at the 2018 International Conference on Applied Smart Systems (ICASS).

Khezri, R., Mahmoudi, A., & Haque, M. H. (2020). Optimal capacity of solar PV and battery storage for Australian grid-connected households. *IEEE Transactions on Industry Applications, 56*(5), 5319-5329.

Killi, M., & Samanta, S. (2015). Modified perturb and observe MPPT algorithm for drift avoidance in photovoltaic systems. *IEEE Transactions on Industrial Electronics, 62*(9), 5549-5559.

Kok Soon Tey, S. M., Mehdi Seyedmahmoudian, Ben Horan, Amanullah Than Oo, and Alex Stojcevski. (2018). Improved Differential Evolution-based MPPT Algorithm using SEPIC for PV Systems under Partial Shading Conditions and Load Variation. *IEEE Transactions on Industrial Informatics, 14*(10), 4322-4333.

Kollimalla, S. K., & Mishra, M. K. (2014). Variable perturbation size adaptive P&O MPPT algorithm for sudden changes in irradiance. *IEEE Transactions on Sustainable Energy, 5*(3), 718-728.

Kumar, N., Hussain, I., Singh, B., & Panigrahi, B. K. (2017). Framework of maximum power extraction from solar PV panel using self predictive perturb and observe algorithm. *IEEE Transactions on Sustainable Energy, 9*(2), 895-903.

Kuo, Y. C., Liang, T. u., & Chen, J. F. (2001). Novel maximum-power-point-tracking controller for photovoltaic energy conversion system. *IEEE Transactions on Industrial Electronics, 48*(3), 594-601.

Lee, J.-G., Ko, J.-S., Jeong, D.-E., Jeong, H.-G., Kim, D.-K., & Chung, D.-H. (2012). *High performance MPPT control of photovoltaic using VSSIC method.* Paper presented at the 2012 IEEE Vehicle Power and Propulsion Conference.

Lee, J. E., Bae, S., Oh, W., Park, H., Kim, S. M., Lee, D., . . . Yang, J. (2016). Investigation of damage caused by partial shading of CuInxGa (1-x) Se2 photovoltaic modules with bypass diodes. *Progress in Photovoltaics: Research and Applications, 24*(8), 1035-1043.

Lee, J. G., Ko, J. S., Jeong, D. E., Jeong, H. G., Kim, D. K., & Chung, D. H. (2012, October). *High performance MPPT control of photovoltaic using VSSIC method.* Paper presented at the 2012 IEEE Vehicle Power and Propulsion Conference. IEEE.

Leng, M., Zhou, G., Tian, Q., Xu, G., & Blaabjerg, F. (2020). Small Signal Modeling and Design Analysis for Boost Converter With Valley V 2 Control. *IEEE transactions on power electronics, 35*(12), 13475-13487.

Li, X., Mauzerall, D. L., & Bergin, M. H. (2020). Global reduction of solar power generation efficiency due to aerosols and panel soiling. *Nature Sustainability, 3*(9), 720-727.

Liu, F., Duan, S., Liu, F., Liu, B., & Kang, Y. (2008). A Variable Step Size INC MPPT Method for PV Systems. *IEEE Transactions on Industrial Electronics, 55*(7), 2622-2628.

Liu, Y., Liu, X., Shi, D., Zhang, Y., Wu, Q., Zhu, Z., & Lin, X. (2019). *An MPPT Approach Using Improved Hill Climbing and Double Closed Loop Control.* Paper presented at the 2019 IEEE 46th Photovoltaic Specialists Conference (PVSC).

Lyden, S., Haque, M. E., Gargoom, A., & Negnevitsky, M. (2013). *Review of maximum power point tracking approaches suitable for PV systems under partial shading conditions.* Paper presented at the 2013 Australasian Universities Power Engineering Conference (AUPEC).

Maghami, M. R., Hizam, H., Gomes, C., Radzi, M. A., Rezadad, M. I., & Hajighorbani, S. (2016). Power loss due to soiling on solar panel: A review. *Renewable and Sustainable Energy Reviews, 59*, 1307-1316.

Maghami, M. R., Hizam, H., Gomes, C., Radzi, M. A., Rezadad, M. I., Hajighorbani, S. J. R., & Reviews, S. E. (2016). Power loss due to soiling on solar panel: A review. *59*, 1307-1316.

Mahmoud, Y., Abdelwahed, M., & El Saadany, E. F. (2016). An Enhanced MPPT Method Combining Model-Based and Heuristic Techniques. *IEEE Transactions on Sustainable Energy, 7*(2), 576-585.

Manickam, C., Raman, G. R., Raman, G. P., Ganesan, S. I., & Nagamani, C. (2016). A Hybrid Algorithm for Tracking of GMPP Based on P&O and PSO With Reduced Power Oscillation in String Inverters. *IEEE Transactions on Industrial Electronics, 63*(10), 6097-6106.

Meghdadi, S., & Iqbal, T. (2015). A low cost method of snow detection on solar panels and sending alerts. *Clean Energy Technol, 3*(5), 393-397.

Meghdadi, S., & Iqbal, T. (2015). A low cost method of snow detection on solar panels and sending alerts. *J. Clean Energy Technol., 3*(5), 393-397.

Mirza, A. F., Mansoor, M., Ling, Q., Yin, B., & Javed, M. Y. (2020). A Salp-Swarm Optimization based MPPT technique for harvesting maximum energy from PV systems under partial shading conditions. *Energy Conversion and Management, 209*, 112625.

Mirzaee, A., Arab Ansari, S., & Shokrollahi Moghani, J. (2020). Single switch quadratic boost converter with continuous input current for high voltage applications. *International Journal of Circuit Theory and Applications, 48*(4), 587-602.

Mohammed, H., Kumar, M., & Gupta, R. (2020). Bypass diode effect on temperature distribution in crystalline silicon photovoltaic module under partial shading. *Solar Energy, 208*, 182-194.

Mohammed, S. S., & Devaraj, D. (2015). *Simulation of Incremental Conductance MPPT based two phase interleaved boost converter using MATLAB/Simulink.* Paper presented at the 2015 IEEE International Conference on Electrical, Computer and communication Technologies (ICECCT).

Mohanty, S., Subudhi, B., & Ray, P. K. (2016). A Grey Wolf Assisted Perturb &Observe MPPT Algorithm for a Photovoltaic Power System. *IEEE Transactions on Energy Conversion, 32*(1), 340-347.

Motahhir, S., El Hammoumi, A., & El Ghzizal, A. (2018). Photovoltaic system with quantitative comparative between an improved MPPT and existing INC and P&O methods under fast varying of solar irradiation. *Energy Reports, 4*, 341-350.

Nazir, F. U., Kumar, N., Pal, B. C., Singh, B., & Panigrahi, B. K. (2020). Enhanced sogi controller for weak grid integrated solar pv system. *IEEE Transactions on Energy Conversion, 35*(3), 1208-1217.

Oruganti, H., Dash, S., Nallaperumal, C., & Ramasamy, S. J. E. (2018). A proportional resonant controller for suppressing resonance in grid tied multilevel inverter. *Energies, 11*(5), 1024.

Ovaska, S. (2010). Maximum power point tracking algorithms for photovoltaic applications. *Diss. Aalto University*.

Palanisamy, R., & Vijayakumar, K. (2020). Transformerless three-phase Z-source four-wire voltage source inverter-fed grid-connected PV system. *International Journal of Ambient Energy*, 1-9.

Panigrahi, R., Mishra, S. K., & Srivastava, S. (2018, September). *Grid Integration of Small-Scale Photovoltaic Systems-A Review.* Paper presented at the 2018 IEEE Industry Applications Society Annual Meeting (IAS). IEEE.

Patel, A., & Tiwari, H. (2017). *Implementation of INC-PIMPPT and its comparison with INC MPPT by direct duty cycle control for solar photovoltaics employing zeta converter.* Paper presented at the 2017 International Conference on Information, Communication, Instrumentation and Control (ICICIC).

Peña, J. C. U., Sampaio, L. P., de Brito, M. A. G., & Canesin, C. A. (2020). RLC passive damped LCL single-phase voltage source inverter with capability to operate in grid-connected and islanded modes: design and control strategy. *Electrical Engineering, 102*(4), 2509-2519.

Prabaharan, N., Arun, V., Palanisamy, K., & Sanjeevikumar, P. (2018). A New Pulse Width Modulation Technique with Hybrid Carrier Arrangement for Multilevel Inverter Topology. In *Advances in Electronics, Communication and Computing* (pp. 37-44). Singapore Springer.

Pugliese, S., Kwon, Y., & Liserre, M. (2020). *Positive-Negative Sequence SRF-PLL Model for Accurate Stability Analysis in Grid-Tied Converters.* Paper presented at the 2020 IEEE Energy Conversion Congress and Exposition (ECCE).

Radianto, D., Dousouky, G. M., & Shoyama, M. (2015, October). *MPPT based on incremental conductance-fuzzy logic algorithm for photovoltaic system under variable climate conditions.* Paper presented at the 2015 IEEE International Telecommunications Energy Conference (INTELEC). IEEE.

Radjai, T., Gaubert, J. P., Rahmani, L., & Mekhilef, S. (2015). Experimental verification of P&O MPPT algorithm with direct control based on Fuzzy logic control using CUK converter. *International Transactions on Electrical Energy Systems, 25*(12), 3492-3508.

Radjai, T., Rahmani, L., Mekhilef, S., & Gaubert, J. P. (2014). Implementation of a modified incremental conductance MPPT algorithm with direct control based on a fuzzy duty cycle change estimator using dSPACE. *Solar Energy, 110*, 325-337.

Rakhshan, M., Vafamand, N., Khooban, M. H., & Blaabjerg, F. (2018). Maximum power point tracking control of photovoltaic systems: A polynomial fuzzy model-based approach. *IEEE Journal of Emerging and Selected Topics in Power Electronics, 6*(1), 292-299.

Ram, J. P., Manghani, H., Pillai, D. S., Babu, T. S., Miyatake, M., & Rajasekar, N. (2018). Analysis on solar PV emulators: A review. *Renewable and Sustainable Energy Reviews, 81*, 149-160.

Rettner, C., Schiedermeier, M., Apelsmeier, A., & März, M. (2020). *Fast DC-link capacitor design for Voltage Source Inverters based on weighted total harmonic distortion.* Paper presented at the 2020 IEEE Applied Power Electronics Conference and Exposition (APEC).

Rex, S. R., & Praba, D. M. S. R. (2020). Design of PWM with four transistor comparator for DC–DC boost converters. *Microprocessors and Microsystems, 72*, 102844.

Rouibah, N., Barazane, L., Rabhi, A., Hajji, B., Bouhedir, R., Hamied, A., & Mellit, A. (2020). *Experimental Assessment of Perturb & Observe, Incremental Conductance and Hill Climbing MPPTs for Photovoltaic Systems.* Paper presented at the International Conference on Electronic Engineering and Renewable Energy.

Sadaf, S., Bhaskar, M. S., Meraj, M., Iqbal, A., & Al-Emadi, N. (2020). A novel modified switched inductor boost converter with reduced switch voltage stress. *IEEE Transactions on Industrial Electronics, 68*(2), 1275-1289.

Sahoo, J., Samanta, S., & Bhattacharyya, S. (2020). Adaptive PID controller with P&O MPPT algorithm for photovoltaic system. *IETE Journal of Research, 66*(4), 442-453.

Saidan, M., Albaali, A. G., Alasis, E., & Kaldellis, J. K. (2016). Experimental study on the effect of dust deposition on solar photovoltaic panels in desert environment. *Renewable Energy, 92*, 499-505.

Saidi, A., & Benachaiba, C. (2016, 15-17 Nov. 2016). *Comparison of IC and P&O algorithms in MPPT for grid connected PV module.* Paper presented at the 2016 8th International Conference on Modelling, Identification and Control (ICMIC).

Saravanan, S., & Babu, N. R. (2015, March). *Performance analysis of boost & Cuk converter in MPPT based PV system.* Paper presented at the 2015 International Conference on Circuits, Power and Computing Technologies [ICCPCT-2015]. IEEE.

Sarikhani, A., Allahverdinejad, B., & Hamzeh, M. (2020). A Non-Isolated Buck-Boost DC-DC Converter with Continuous Input Current for Photovoltaic Applications. *IEEE Journal of Emerging and Selected Topics in Power Electronics*.

Sarker, R., Datta, A., & Debnath, S. (2020). FPGA-Based High-Definition SPWM Generation With Harmonic Mitigation Property for Voltage Source Inverter Applications. *IEEE Transactions on Industrial Informatics, 17*(2), 1352-1362.

Sebtahmadi, S. S., Azad, H. B., Kaboli, S. H. A., Islam, M. D., & Mekhilef, S. (2018). A PSO-DQ current control scheme for performance enhancement of Z-source matrix converter to drive IM Fed by abnormal voltage. *IEEE transactions on power electronics, 33*(2), 1666-1681.

Seyedmahmoudian, M., Horan, B., Soon, T. K., Rahmani, R., Oo, A. M. T., Mekhilef, S., & Stojcevski, A. (2016). State of the art artificial intelligence-based MPPT techniques for mitigating partial shading effects on PV systems–a review. *Renewable and Sustainable Energy Reviews, 64*, 435-455.

Sgrò, D., Souza, S. A., Tofoli, F. L., Leão, R. P. S., & Sombra, A. K. R. (2020). An integrated design approach of LCL filters based on nonlinear inductors for grid-connected inverter applications. *Electric Power Systems Research, 186*, 106389.

Shams, I., Saad, M., & SOON, T. K. (2020). Improved Team Game Optimization Algorithm Based Solar MPPT with Fast Convergence Speed and Fast Response to Load Variations. *IEEE Transactions on Industrial Electronics*.

Sharif, S. (2018). Half-Sine Wave Modulation Technique a New Method for Generating Variable Frequency Sinusoidal Current. *IEEE transactions on power electronics, 34*(7), 6575-6582.

Sharma, N., & Puri, V. (2020). Solar Energy Fundamental Methodologies and its Economics: A Review. *IETE Journal of Research*, 1-26.

Shebani, M. M., Iqbal, T., & Quaicoe, J. E. (2016, 12-14 Oct. 2016). *Comparing bisection numerical algorithm with fractional short circuit current and open circuit voltage methods for MPPT photovoltaic systems.* Paper presented at the 2016 IEEE Electrical Power and Energy Conference (EPEC).

Sher, H. A., Murtaza, A. F., Noman, A., Addoweesh, K. E., Al-Haddad, K., & Chiaberge, M. (2015). A new sensorless hybrid MPPT algorithm based on fractional short-circuit current measurement and P&O MPPT. *IEEE Transactions on Sustainable Energy, 6*(4), 1426-1434.

Singh, N., & Khan, I. (2020). *Scheme and Simulation of SVPWM and SPWM based on two level VSI for Grid connected PV System.* Paper presented at the 2020 International Conference on Advances in Computing, Communication & Materials (ICACCM).

Singh, P., Palwalia, D., Gupta, A., & Kumar, P. (2015). Comparison of photovoltaic array maximum power point tracking techniques. *Int. Adv. Res. J. Sci. Eng. Technol, 2*(1), 401-404.

Smadi, I. A., & Rana, A.-Q. (2020). Explicit one-step model and adaptive maximum power point tracking algorithm for a photovoltaic module. *Computers & Electrical Engineering, 85*, 106659.

Soon, T. K., & Mekhilef, S. (2014). A fast-converging MPPT technique for photovoltaic system under fast-varying solar irradiation and load resistance. *Industrial Informatics, IEEE Transactions on, 11*(1), 176-186.

Stojić, D., Georgijević, N., Rivera, M., & Milić, S. (2017). Novel orthogonal signal generator for single phase PLL applications. *IET Power Electronics, 11*(3), 427-433.

Suman, N., Yadav, D., & Jangid, T. (2018). *Modelling and Analysis of Photovoltaic System with Improved Inverter Technique.* Paper presented at the 2018 9th International Conference on Computing, Communication and Networking Technologies (ICCCNT). IEEE.

Sundareswaran, K., Vigneshkumar, V., Sankar, P., Simon, S. P., Nayak, P. S. R., & Palani, S. (2015). Development of an improved P&O algorithm assisted through a colony of foraging ants for MPPT in PV system. *IEEE Transactions on Industrial Informatics, 12*(1), 187-200.

Teo, J., Tan, R. H., Mok, V., Ramachandaramurthy, V. K., & Tan, C. (2020). Impact of bypass diode forward voltage on maximum power of a photovoltaic system under partial shading conditions. *Energy, 191*, 116491.

Teo, K. T. K., Lim, P. Y., Chua, B. L., Goh, H. H., & Tan, M. K. (2014, December). *Maximum Power Point Tracking of Partially Shaded Photovoltaic Arrays Using Particle Swarm Optimization.* Paper presented at the 2014 4th International Conference on Artificial Intelligence with Applications in Engineering and Technology. IEEE.

Tey, K. S., & Mekhilef, S. (2014). Modified incremental conductance MPPT algorithm to mitigate inaccurate responses under fast-changing solar irradiation level. *Solar Energy, 101*, 333-342.

Uno, M., & Kukita, A. (2014). Two-Switch Voltage Equalizer Using an LLC Resonant Inverter and Voltage Multiplier for Partially Shaded Series-Connected Photovoltaic Modules. *IEEE Transactions on Industry Applications, 51*(2), 1587-1601.

Villalva, M. G., Gazoli, J. R., & Ruppert Filho, E. (2009). *Modeling and circuit-based simulation of photovoltaic arrays.* Paper presented at the 2009 Brazilian Power Electronics Conference. IEEE.

Voswinckel, S., Mikolajick, T., & Wesselak, V. (2020). Influence of the active leakage current pathway on the potential induced degradation of CIGS thin film solar modules. *Solar Energy, 197*, 455-461.

Wang, Y., Li, Y., & Ruan, X. (2016). High-Accuracy and Fast-Speed MPPT Methods for PV String Under Partially Shaded Conditions. *IEEE Transactions on Industrial Electronics, 63*(1), 235-245.

Winston, D. P., Kumaravel, S., Kumar, B. P., & Devakirubakaran, S. (2020). Performance improvement of solar PV array topologies during various partial shading conditions. *Solar Energy, 196*, 228-242.

Xia, T., Zhang, X., Tan, G., & Liu, Y. (2020). Synchronous reference frame single-phase phase-locked loop (PLL) algorithm based on half-cycle DFT. *IET Power Electronics, 13*(9), 1893-1900.

Yan, C., Qu, M., Chen, Y., & Feng, M. (2020). Snow removal method for self-heating of photovoltaic panels and its feasibility study. *Solar Energy, 206*, 374-380.

Youssef, A., El-Telbany, M., & Zekry, A. (2018). Design and simulation of fuzzy controller for three phase grid connected PV systems. *International Journal of Engineering & Technology, 7*(4), 5554-5557.

Yuan, X., Allmeling, J., Merk, W., & Stemmler, H. (2000, October). *Stationary frame generalized integrators for current control of active power filters with zero steady state error for current harmonics of concern under unbalanced and distorted operation conditions.* Paper presented at the Conference Record of the 2000 IEEE Industry Applications Conference. Thirty-Fifth IAS Annual Meeting and World Conference on Industrial Applications of Electrical Energy (Cat. No. 00CH37129). IEEE.

Yuditya, B. H., Hasanah, R. N., Ardhenta, L., & Taufik, T. (2020). *Performance Comparison of Single-Phase Multilevel Inverter with SPWM Unipolar and Bipolar Switching Techniques.* Paper presented at the 2020 FORTEI-International Conference on Electrical Engineering (FORTEI-ICEE).

Yunmei, C., & Xiangwei, L. (2019). *Study of bypass diodes configuration on PV modules with partial shaded.* Paper presented at the 2019 Chinese Control And Decision Conference (CCDC).

Zakzouk, N. E., Abdelsalam, A. K., Helal, A. A., & Williams, B. W. (2020). High performance single-phase single-stage grid-tied PV current source inverter using cascaded harmonic compensators. *Energies, 13*(2), 380.

Zhang, H., Lu, Y., Han, W., Zhu, J., Zhang, Y., & Huang, W. (2020). Solar energy conversion and utilization: Towards the emerging photo-electrochemical devices based on perovskite photovoltaics. *Chemical Engineering Journal, 393*, 124766.

Zhang, R., Wu, A., Zhang, S., Wang, Z., & Cang, S. (2018). Dynamical analysis and circuit implementation of a DC/DC single-stage boost converter with memristance load. *Nonlinear Dynamics, 93*(3), 1741-1755.

LIST OF PUBLICATIONS AND PAPERS PRESENTED

➢ Journal Paper (published)

- Improved Proportional-Integral Coordinated MPPT Controller with Fast Tracking Speed for Grid-Tied PV Systems under Partially Shaded Conditions. Sustainability, 13 (2), 830. Status: Published on 15th January 2021.

sustainability MDPI

Article

Improved Proportional-Integral Coordinated MPPT Controller with Fast Tracking Speed for Grid-Tied PV Systems under Partially Shaded Conditions

Haidar Islam [1,*], Saad Mekhilef [1,*], Noraisyah Mohamed Shah [2], Tey Kok Soon [3], Addy Wahyudie [4,*] and Mahrous Ahmed [5]

1 Power Electronics and Renewable Energy Research Laboratory (PEARL), Department of Electrical, Faculty of Engineering, University of Malaya, Kuala Lumpur 50603, Malaysia
2 Department of Electrical, Faculty of Engineering, University of Malaya, Kuala Lumpur 50603, Malaysia; noraisyah@um.edu.my
3 Department of Computer System & Technology, Faculty of Computer Science & Information Technology, University of Malaya, Kuala Lumpur 50603, Malaysia; koksoon@um.edu.my
4 Department of Electrical Engineering, United Arab Emirates University, P.O. Box 15551, Al Ain, UAE
5 Department of Electrical Engineering, College of Engineering, Taif University, Taif 219744, Saudi Arabia; m.elsamman@tu.edu.sa
* Correspondence: haidar.meee@siswa.um.edu.my (H.I.); saad@um.edu.my (S.M.); addy.w@uaeu.ac.ae (A.W.)

Abstract: When a photovoltaic (PV) system is exposed to physical objects and cloud coverage and connected to bypass diodes, a partial shading condition (PSC) occurs, which causes a global maximum power point (GMPP) and numerous local maximum power points (LMPPs) on the power-voltage (P-V) curve. Unlike conventional MPPT techniques that search for multiple LMPPs on the P-V curve, it is possible to track GMPP straightaway by designing a simple but robust MPPT technique that results in faster tracking speed and low power oscillations. Hence, in this study, an improved proportional-integral (PI) coordinated Maximum Power Point Tracking (MPPT) algorithm is designed to enhance the conversion efficiency of a PV system under PSC with fast-tracking speed and reduced power oscillations. Here, PI controllers are used to mitigating the steady-state errors of output voltage and current of PV system that later on passed through an incremental conductance (INC) algorithm to regulate the duty cycle of a dc–dc boost converter in order to ensure fast MPPT process. The PV system is integrated with the grid through an H-bridge inverter, which is controlled by a synchronous reference frame (SRF) controller. Tracking speed and steady-state oscillations of the proposed MPPT are evaluated in the MATLAB/Simulink environment and validated via a laboratory experimental setup using Agilent solar simulator and dSPACE (DS1104) controller. Results show that the proposed MPPT technique reduces the power fluctuations of PV array significantly and the tracking speed of the proposed method is 13% and 11% faster than the conventional INC and perturb and observe (P&O) methods respectively under PSCs.

Keywords: MPPT; PWM; partial shading condition; PV; grid-connected; incremental conductance and PI

check for updates

Citation: Islam, H.; Mekhilef, S.; Shah, N.M.; Soon, T.K.; Wahyudie, A.; Ahmed, M. Improved Proportional-Integral Coordinated MPPT Controller with Fast Tracking Speed for Grid-Tied PV Systems under Partially Shaded Conditions. *Sustainability* **2021**, *13*, 830. https://doi.org/10.3390/su13020830

Received: 24 December 2020
Accepted: 12 January 2021
Published: 15 January 2021

Publisher's Note: MDPI stays neutral with regard to jurisdictional claims in published maps and institutional affiliations.

1. Introduction

The demand for renewable energy as an alternative source of conventional power generation is increasing because of a decrease in its production expenses, zero carbon emissions, and economical tariffs [1]. Renewable energy production is predicted to increase by 6.7% by 2030 [2]. The report of the Joint Research Center revealed that the global installation of PV plants was 315 GW in 2016, with a cumulative increase of 40% annual production over the last 15 years. Therefore, 133.7 billion USD was invested in 2016 alone to produce PV energy, comprising 55% of gross renewable energy cost [3]. Nevertheless, solar energy is harnessed from a PV module that is viable, sustainable, eco-friendly, efficient,

- Performance evaluation of maximum power point tracking approaches and photovoltaic systems. Energies, 11(2), 365. Status: Published on 4th February 2018.

energies

MDPI

Review

Performance Evaluation of Maximum Power Point Tracking Approaches and Photovoltaic Systems

Haidar Islam [1,*], Saad Mekhilef [1,*], Noraisyah Binti Mohamed Shah [2], Tey Kok Soon [3], Mehdi Seyedmahmousian [4], Ben Horan [4] and Alex Stojcevski [4]

[1] Power Electronics and Renewable Energy Research Laboratory (PEARL), Department of Electrical Engineering, University of Malaya, Kuala Lumpur 50603, Malaysia

[2] Department of Electrical, Engineering, University of Malaya, Kuala Lumpur 50603, Malaysia; noraisyah@um.edu.my

[3] Department of Computer System & Technology, Faculty of Computer Science & Information Technology, University of Malaya, Kuala Lumpur 50603, Malaysia; koksoon@um.edu.my

[4] School of Engineering, Deakin University, Waurn Ponds, Victoria 3216, Australia; mehdis@deakin.edu.au (M.S.); ben.horan@deakin.edu.au (B.H.); astojcevski@swin.edu.au (A.S.)

* Correspondence: haidareee@gmail.com (H.I.); saad@um.edu.my (S.M.); Tel.: +60-37-967-7667 (H.I.); Tel.: +60-37-967-6851 (S.M.)

Received: 5 January 2018; Accepted: 29 January 2018; Published: 4 February 2018

Abstract: This paper elaborates a comprehensive overview of a photovoltaic (PV) system model, and compares the attributes of various conventional and improved incremental conductance algorithms, perturbation and observation techniques, and other maximum power point tracking (MPPT) algorithms in normal and partial shading conditions. Performance evaluation techniques are discussed on the basis of the dynamic parameters of the PV system. Following a discussion of the MPPT algorithms in each category, a table is drawn to summarize their key specifications. In the performance evaluation section, the appropriate PV module technologies, atmospheric effects on PV panels, design complexity, and number of sensors and internal parameters of the PV system are outlined. In the last phase, a comparative table presents performance-evaluating parameters of MPPT design criterion. This paper is organized in such a way that future researchers and engineers can select an appropriate MPPT scheme without complication.

Keywords: maximum power point tracking; photovoltaic systems; incremental conductance; perturbation and observation; partial shading conditions; performance evaluation

1. Introduction

Energy is a necessity in our lives, contributing to the development of economies, and social growth [1,2]. Fossil fuels such as coal, gas, and oil contribute nearly 87% of the total global energy production, whereas nuclear power plants generate approximately 6% of the energy. Renewable-energy, such as solar, geothermal, wind, hydro, and biofuels, produce the remaining 7% of the total energy demand [3,4]. In the last couple of decades, many studies on solar energy have been conducted because of its abundance, renewability and clean nature [5,6]. Photovoltaic technology (PV) is an important technology that can convert solar irradiance directly to electrical energy through a PV panel [5,7]. However, solar PV panels have drawbacks, such as very low energy conversion efficiency (less than 22.5%), the high manufacturing cost of energy, and high dependence on environmental factors [5,7–9]. The power of a PV array is unstable, and the current and voltage characteristics curve of a PV cell is

➢ Conference (published)

- Comparative Study of Different Transformer-less Inverter Topologies for Grid-tied Photovoltaic System. In 2019 5th International Conference on Advances in Electrical Engineering (ICAEE).

Comparative Study of Different Transformer-less Inverter Topologies for Grid-tied Photovoltaic System

Arghya Saha
Renewable Energy and Technology Institute of Energy
University of Dhaka
Dhaka-1000, Bangladesh
E-mail: arghyasaha2013@gmail.com

Shameem Ahmad, Saad Mekhilef, Umme Kulsum Jhuma, Haidar Islam, Zahirul Amin Chowdhury
Power Electronics and Renewable Energy Research Laboratory (PEARL), Department of Electrical Engineering, University of Malaya
Kuala Lumpur, Malaysia
E-mail:shameem.ahmad@hotmail.com, saad@um.edu.my,umme.jr@gmail.com haidareee@gmail.com, zac.eee@hotmail.com

Monirul Islam
School of Information Technology and Electrical Engineering
University of Queensland, St Lucia
Brisbane, Australia
E-mail: monir04eee@yahoo.com

***Abstract*— Lately, interest is developing significantly on transformerless photovoltaic (PV) inverter for its small size, low cost and high efficiency compared to the inverter which has transformer. Different topologies of transformerless inverters are stated in the literature based on the leakage current characteristics. In this paper five different topologies of transformerless inverters (H5, H6, HERIC, Modified H6, OH5) have been selected for analysis. For controlling the grid current and voltage of the DC link a common controller for all the topologies has been designed based on PI controller and SPWM technique. These two techniques have been used to generate the switching pulses for the inverter switches. The simulation of all the five topologies are conducted in MATLAB/SIMULINK environment and analysis has been done. Finally, based on that a comparative study has been obtained based on the component ratings, leakage current, maximum efficiency and components number to determine a better topology for real world operation.**

Keywords—Transformerless photovoltaic inverter, H5 Topology, H6 Topology, HERIC Topology, PI controller, SPWM technique.

I. INTRODUCTION

The conventional power plants are coal fired power plant, gas power plant, hydro power plant and nuclear power plant. In these types of power plants, electricity needs to transmit over a long distance from the generation. These are centralized systems [1-2]. In [3], it is mentioned that the safety and solidity of these power system networks are in danger because of a number of blackouts. Moreover, Extreme weather ruptures power grid . On the other hand, solar and wind power, biogas, biomass are known as decentralized energy sources. These sources are more flexible and modular. The transmission line losses can be reduced by using these distributed energy sources. The use of fossil fuels is also reducing our total energy and is also polluting our environment [4]. Hence, these energy sources especially solar and wind power based energy sources have gain more

Usually, Photovoltaic inverters is divided into two groups on the basis of the galvanic isolation. First one is isolated inverter and the other is non-isolated inverter. A transformer which is operated in high or low frequency can be used in isolated inverter. As the size of the low frequency transformer is big it also increases the total system area. In [6,7] it is stated that non-isolated (transformerless) inverter has higher efficiency and it is small in size than isolated inverter. Yet, because of no transformer, there is leakage current in non-isolated inverter (galvanic isolation) . However, parasitic capacitance can be a problem. This problem can be solved by using transformers but it will reduce the efficiency. The connection between PV array and grid is direct if non-isolated inverter is used and it is made without galvanic isolation. During the operation of the switching components (at starting), with the help of common node capacitive current is injected in the inverter. This induced leakage current affects the normal characteristics of it and eventually array is disconnected when residual current is tripped. This induced leakage current can be the reason of tripping residual current and then the whole system has to be reactivated manually. So, the leakage current should be eliminated or it must be kept in a low value. Hence, a number of researches has been done to eliminate this problem and it is proved that this can be solved by the modification of the PV system.

In this paper, simulation has been done on some latest topologies of PV inverters and performance has been analyzed. The main perspective is to deliver some developments in grid connected PV inverter. At first, literature review of different PV inverter system is presented and demands for the grid and PV module has been examined. Later, leakage current problem of non-isolated inverter is discussed. Next, the performance of the different topologies were compared by doing simulation in MATLAB/ SIMULINK. Lastly, by discussing the approaches, the best one among the topologies of grid-tied PV system has been

➢ Conference (Presented)

- State of the art of modified PV-MPPT Techniques. In IEEE Conference on Saudi Arabia Smart Grid (SASG 2018).

State of the Art of Modified PV-MPPT Techniques

MD Haidar Islam[1], Saad Mekhilef[1, 2], Noraisyah Mohamed Shah[1], Tey Kok Soon[3], Muhyaddin Rawa[2, 4], Hussain Bassi[5]

[1]***Abstract*-- Solar energy has greater impact on our lives and contribution to the development of social growth. In the last couple of decades, researchers conducted many studies on solar energy due to its abundance, renewability and clean nature. Photovoltaic (PV) technology is a dominant technology that can convert solar irradiance directly to electrical energy through a PV system. However, solar PV panels have drawbacks, such as very low energy conversion efficiency, the high manufacturing cost of energy, and high dependence on environmental factors. Maximum Power Point Tracking (MPPT) algorithm is required to maximize overall energy production from PV sources during random atmospheric conditions. MPPT charge controllers are imperative techniques used to maximize photovoltaic output power. The conventional MPPT strategies are easier to implement due to having a unique operating point at uniform condition. However, it is challenging to operate large and partly shaded PV systems with high PV penetration level. Improved methods are found to be particularly suitable in detecting global maxima by reducing rising complexities at Partial Shading Conditions. This paper reviews some newly developed modified MPPT techniques for investigating the performance of an overall PV system are evaluated in terms of their robustness, effectiveness to Partial Shading Conditions (PSCs), less implementation complexity and fast computing in dynamics and steady-state conditions. These include modified Gray Wolf Optimization (GWO), Solar Tracker INC-MPPT, Search Skip Judge (SSJ) MPPT, Flower Pollination Algorithm (FPA), Gaussian Arctangent Function (GAF) and Double Integral Sliding Mode Control (DISMC) algorithms.**

***Index Terms*-- Maximum Power Point Tracking (MPPT), Incremental Conductance (INC), Perturbation and Observation (P&O), Partial Shading Conditions (PSCs).**

I. Introduction

THE increasing demand in energy consumption and the unpredictable price of fuel requires the need to address the impacts of economic progress and environmental pollution [1]. Many conventional, online and offline MPPT schemes such as Incremental Conductance (INC), Perturbation and Observation (P&O), Fractional Open Circuit Voltage (FOCV), Fractional Short Circuit Current (FSCC) are designed to track the Maximum Power Point (MPP) for uniform environmental conditions where the PV curve generates only one MPP [2], [3]. However, the power of a PV array is unstable and the I-V characteristic of the PV cell is non-linear, and it varies with irradiation, temperature and loads, resulting in the emergence of the global maximum power point (GMPP) and the local maximum power points (LMPPs) [4]. The GMPP and LMPPs appear on the PV curves whenever various PV modules are subjected to unequal solar insolation levels, which implies to PSCs [5].

The modified MPPT techniques are developed to track GMPP quickly instead of searching more LMPPs by skipping unnecessary voltage intervals under PSCs [6]. These techniques enable a high convergence speed, robustness to interferences and panel deteriorations, as well as providing optimum efficiency on high-powered PV system [7]. To enhance the performance of an overall PV system, numerous improved MPPT techniques are outlined in this paper with their key system parameters, effect of PSCs, implementation complexity, flexibility, reliability and cost effectiveness.

II. PV Array Modeling

PV cells are made with p-n junction diode to produce electrical energy from photons. It can absorb the solar illumination and can convert the photons to electrons in a convergence period. A small light load or DC motor is able to directly obtain electric supply from the panel terminals. However, some applications need a dc/dc converter to control load current, load voltage, power flow from a grid-connected system and to track the MPP [8]. The PV panel equivalent circuit and PV curves in different solar insolation levels show in Fig. 1 and Fig. 2 respectively.

$$I = I_{pv}N_{par} - I_o N_{par}\left[\exp\left(\frac{V + R_s\left(\frac{N_{ser}}{N_{par}}\right)I}{V_t \alpha N_{ser}}\right) - 1\right] - \frac{V + R_s\left(\frac{N_{ser}}{N_{par}}\right)I}{R_p\left(\frac{N_{ser}}{N_{par}}\right)} \quad (1)$$

[1]Power Electronics and Renewable Energy Research Laboratory (PEARL), Faculty of Engineering, University of Malaya, 50603 Kuala Lumpur, Malaysia (haidareee@gmail.com; saad@um.edu.my; noraisyah@um.edu.my).
[2]Center of Research Excellence in Renewable Energy and Power Systems, King Abdulaziz University, Jeddah 21589, Saudi Arabia (mrawa@kau.edu.sa; saad@um.edu.my).
[3]Department of Computer System & Technology, Faculty of Computer Science & Information Technology, University of Malaya, 50603 Kuala Lumpur, Malaysia (koksoon@um.edu.my).
[4]Department of Electrical and Computer Engineering, King Abdulaziz University, Jeddah 21589, Saudi Arabia (mrawa@kau.edu.sa).